80GRC020F0166 3.3-2 Rev.D
February 28, 2025

AC AND DC FAULT MANAGEMENT FOR MEGAWATT ELECTRIFIED AIRCRAFT ELECTRICAL POWERTRAINS

TASK 3: LIFETIME AND RELIABILITY OF ELECTRICAL INSULATORS

FINAL REPORT

Prepared for
NASA Glenn Research Center
21000 Brookpark Road
Cleveland, OH 44135
Attention: Andrew Woodworth

Prepared by
Raytheon Technologies Corporation
Pratt & Whitney
400 Main Street
East Harford, CT 06118 USA

Prepared in Response to:
Contract No. NNC15BA06B
Task Order No. 80GRC020F0166
CDRL No.: 3.3-2

GO BEYOND

This document does not contain any export regulated technical data.

TABLE OF CONTENTS

Section *Page*

Section *Page*

LIST OF FIGURES

Figure *Page*

Figure *Page*

Figure *Page*

Figure *Page*

LIST OF TABLES

Table *Page*

ACRONYMS

A

AC	Alternating Current
AMR	Adaptive Mesh Refinement

B

BEM	boundary Element Method

C

CSF	Continuous Surface Field

D

DC	Direct Current
DUT	Device Under Test

H

HFCT	High Frequency Current Transformer

I

IBM	Immersed Boundary Method
IEC	International Electrotechnical Commission

P

PD	Partial Discharge
PDIV	Partial Discharge Inception Voltage
PFA	Perfluoro Alkoxy

R

RTRC	RTX Technology Research Center
RTX	Raytheon Technology Corporation

T

TGA	Thermogravimetric

1. EXECUTIVE SUMMARY

This research project was a collaborative investigation between researchers at the RTX Technology Research Center (RTRC) and the University of Texas at Austin and made a significant contribution to enabling electric aircraft. The transport of electric power between the points of generation and use requires power cables. These cables must be smaller, lighter and provide a more predictable life than power cables used in stationary applications. Consequently, this investigation provided heretofore unavailable information supporting the safety and reliability of smaller lighter power cables for electrified aircraft. In addition, the research identified key additional engineering data needed to support quantitative reliability assessments. Important advances included:

- Demonstrated that at least one manufacturer can make a novel, smaller, lighter power cable that is free from serious defects.
- Developed and published an appropriate analytical construct to describe the life of this novel cable. This is a necessary step for use in aviation where the understanding of remaining life is critical.
- Demonstrated thermal-mechanical aging that suggested 1000+ flights before the thermal-mechanical processes produced defects large enough that the defect growth was accelerated electrically.
- Showed that electrical aging took place at two rates. The first possibly lasting weeks to months and the second possibly days to weeks. If robust, this provides a good diagnostic for cable replacement.
- Demonstrated that the traditional electrical testing of cable materials using manufactured voids can be misleading due to the size of the voids. Emerging laser drilling technology permitted demonstration that the physics of failure in realistically small voids is different from that in the unrealistically large voids used in earlier research, which is very important for high-quality, high-performance, small aircraft cables.

Although this project represents a significant contribution to the specifics of cable aging in the aircraft environment, important additional research remains to be completed, including:

- Non-uniform thermal cycling by applying the heat from the center conductor to maximize thermal stress next to the core area where the electric gradient is the strongest. This builds on the uniform thermal cycling that has been completed.
- The augmentation of the thermal-mechanical failure rate by electrical processes. Better understanding of these time constants strongly affects the ability to predict life.
- Termination design: Terminations provide not only electrical reflection potential, but a location for a series arc fault and an area where ozone can diffuse into the center conductor and negatively affect cable insulation.
- The abrasion and ozone resistance of the cable jacket.
- Pressure cycling as an accelerant of thermal, mechanical, and/or electrical aging.
- Possible methods for online PD detection and offline PD localization

2. INTRODUCTION

2.1. Background

The electric power cables used in transportation lead a different life than the power cables used in the electric grid for decades. Life prediction for grid power cables is continuously improving by combining statistical operating data and physics of failure information. By comparison, life prediction is as, or often more, critical for power cables used in transportation electrification. However, there is little information as to what can be learned from grid experience that is useful in the emerging transportation applications.

Decades of research demonstrated that the life of cables in the legacy grid is dictated by the thermal, electrical, and mechanical operational environment. Conventional predictions of the life of legacy grid power cables are based on the measurement of partial discharges. The correlation of the measured discharge patterns with life inferred using historical knowledge of both pattern development and life. That knowledge is based on the cable material as well as thermal, mechanical, and electrical environment.

For the legacy grid, life assessment is useful for assuring power system reliability, but decades of experience have shown that cable failure in grid applications is relatively rare [1]. Consequently, reliable remaining life predictions are useful but generally not critical. Besides, in designing for the grid, increased size and weight can be acceptable if the increase leads to system reliability.

By comparison, aircraft impose more stringent constraints because they have a very different thermal, electrical, and mechanical environment than is encountered in buried utility cables as summarized in Table 2-1. In addition, smaller size and lighter weight are more important in transportation electrification than in the grid. This opens the opportunity to use different dielectric material in power cables for transportation than for the grid. New materials bring a cost to understand potentially novel life-limiting factors. A challenge is to balance the increase in cost with a commensurate reliability increase. For transportation, the weight must be transported for the life of the system, thus the weight also imposes an operating cost. Consequently, the design pressure is to use the smallest cable possible that has adequate life. So, life prediction is more important in transportation electrification than in the grid.

Moreover, emerging materials permit operation at higher temperatures than are common in the grid. So, while the detection of partial discharges was an important activity, there was not sufficiently comprehensive and diverse relevant data to use partial discharge characteristics to support life assessment in the relevant environment. Therefore, in this investigation, the focus was to use partial discharges to provide insight into a potentially different aging process and aging rates than were dominant historically.

This is critical because both military and civil aircrafts have been brought down by rare cable insulation failures. The electrification of aviation raises the voltage and power in cables which are as small as can be used safely, enhancing the need for reliable data.

Consequently, a fundamental challenge faced by aircraft electrification is to achieve reliable life predictions with novel materials and different environmental conditions than are typically encountered by grid power cables. The aircraft environment has different temperature, pressure, electrical, shock, and vibration environments than conventionally experienced by power cables in the grid. This report provides a combined theoretical and experimental approach to achieve a conservative, but useful, life estimate in the aircraft environment. The theoretical approach focused on the development of a model that incorporates sufficient details of the physics of failure to provide a life estimate without careful analysis of processes that provide little impact on life. Experiments were conducted to provide a statistical representation of the degradation rate as a function of the material initial defects distribution under nominally accelerated conditions. This would enable the model to have a quantitative rate constant that can then be used to predict aging under representative flight (i.e., cyclic) conditions. Moreover, this combined use of an analytical and experimental approach provides a strong foundation for continuously improved life predictions.

Table 2-1. *Relevant Differences between the Environments Faced by Legacy Grid and Aircraft Cables*

Failure Physics	Important Differences from Legacy Grid	Implications for Aircraft
Thermal	Aircraft operate at the dynamic temperature range that is influenced not only by the current variations but also by the external temperature variations.	Limited thermal management capability leads to the use of new materials. It is unlikely that new material development is needed because there are commercially available materials with promising properties. However, there is little or no life data available for the potentially improved cable materials. Earlier research showed thermal stresses stimulated void formation leading to electrically induced failure. While the fundamental physics of failure is likely the same in both applications, the rates would depend on the environment.
Mechanical	Aircraft shock and vibration levels are greater.	Shock and vibration produce mechanical stresses in the insulation that accelerate void formation. Higher failure probabilities at fixed terminations
Electrical	Aircraft have a much different electrical environment than the one for which grid cables are designed and tested.	Land-based systems designed for transients that do not occur in transportation. DC power has a higher partial discharge initiation voltage leading to longer life with a given void size. Pulse Width Modulation (PWM) square waveforms and 60 Hz produce different partial discharge patterns. The effect of those differences on insulation life is unquantified

2.2. Synopsis of Relationship between Theory and Experimentation

Technical understanding of the life of electric power cables is largely based on experience with the legacy grid. Future electric aircraft are likely to operate beyond traditional distribution voltages (i.e., 270V) due to the increased onboard electric power demand, and hence, the cabling adds an additional level of concern. Owing to the higher operational stresses that occur during in-flight operation, i.e. self-heating, the cable is most likely to fail at this critical period. That requires that precursors to failure be identified to permit replacement of cables before risk of in-flight failure. Fortunately, the current understanding of the physics of cable failure suggests that success in developing the required understanding is possible.

Conceptually, failure begins at defects in the cable. Over the decades, factory quality control has matured so that defect-free cables can be manufactured at the length and diameter needed for electrified aircraft. The screening test to verify high quality is to achieve a partial discharge initiation voltage significantly higher than the operating voltage. For the cables used in this study, tests at the manufacturer, at the University of Connecticut, and at the University of Texas at Austin all showed the cable samples were of high quality.

Consequently, the research hypothesis, based on decades of published research, was that the aging of the cable in service would progress as follows:

- The thermal and mechanical stresses would lead to the formation of voids, likely at the crystalline-amorphous boundaries in the polymer. This is a process that is expected to take months to years. The long time is because the voids must grow to characteristic sizes of greater than about a micrometer before they accelerate aging.

- The situation changes when the voids to about a micrometer and so can sustain an electrical discharge at the peaks of the applied voltage. Then the thermal/mechanical aging is augmented by electrical aging. This phase is expected to take from weeks to months from process initiation to cable failure and has two parts.
  - The electrons from the discharge attach to the void-surface molecules. They then can be transported through the polymer.
  - Plasma etching by the discharge leading to void growth and the growth of filamentary structures from the void. These permit longer free path for the plasma electrons in the void and consequently more energy deposited in the polymer.
- The final phase of failure occurs when the force between the electrons and the applied voltage cannot be sustained, and the insulation fails electrically and mechanically.

Legacy information suggested that the thermal-mechanical void growth would be very slow and there would be ample time to detect aging after the void growth reached the stage that that aging was electrically augmented. Since it would contribute little to the needed life detection, the thermal/mechanical process was not modeled. Experiments were conducted, however, that added confidence to the assumption of slow degradation under thermal/mechanical stress.

Theoretical descriptions were developed of the field enhancement at voids, of partial discharges within voids and of void growth. Because the parameters in the models were not sufficiently well characterized in the literature, experiments were designed to determine rate information for the various processes. Initial information was promising. The partial discharge patterns changed in ways consistent with the growth models. Additionally, the partial discharge energy could be measured with some accuracy, and this was expected to correlate with aging.

An unanticipated critical need for this research, however, was identified after the preliminary experimentation. The preponderance of the historical experimental evidence for void growth under partial discharges was accumulated using a conventional way to manufacture test voids. This approach produced a body of self-consistent data.

The research team was concerned that this data set was limited to voids that had about one million times the volume of the relevant voids. Conventional wisdom was that the size difference had little effect on cable life because, over that volume range, the amount of gas involved in a partial discharge was small compared to the void gas number density.

With the help of the NASA advisors to the program, the researchers identified an emerging laser-based technique for test void fabrication. This approach permitted exploration of the gap in void volume between naturally occurring voids and the conventional test voids.

The preliminary data demonstrated a previously undocumented behavior. As the void became smaller in diameter, the erosion of the polymer due to partial discharges migrated to the void periphery. Analysis showed that this, heretofore, unreported behavior could be predicted from Maxwell's equations and material properties. So, the phenomenon has a firm foundation in classical physics. But it may affect the failure rate as it tends to concentrate void growth. So, it requires more complete characterization.

A second likely relevant situation was observed but there was not time or budget for further exploration. It was noted that the smaller voids likely are more sensitive to effects of pressure and temperature than were the larger voids. This arises from a comparable amount of energy per partial discharge in all voids, but a considerably smaller amount of buffer gas in smaller voids. This is likely of some significance because an increase in pressure can raise or lower the partial discharge initiation voltage, depending on the operating point on the Paschen curve. And the increase in temperature and pressure can accelerate void growth.

While the growth of voids is important, the team also analyzed a second, potentially relevant process. This is the bulk conduction of electrons, driven by the electric field and augmented by the increases in temperature. This produces electrothermal aging which may accelerate aging beyond that due to void growth. While this was estimated theoretically, there was not time available to assess the relative contribution to aging experimentally.

3. LIFE MODELING

The major contributors to partial discharge behavior are the gaseous medium supporting the discharge and the electric field distribution based on electrode configuration and dielectric material properties. Generally, partial discharges exhibit one of three kinds of gas discharge [2][3]: Townsend discharge, streamer discharge and the leader discharge. Partial discharge phenomena can be divided into corona discharges, surface discharges and internal discharges (Fig. 3-1). Additionally, altitude is a key challenge for (hybrid) electrical propulsion in its insulation system design, as the partial discharge initiation voltage (PDIV) at 51,00 ft could be one fifth of that at sea level.

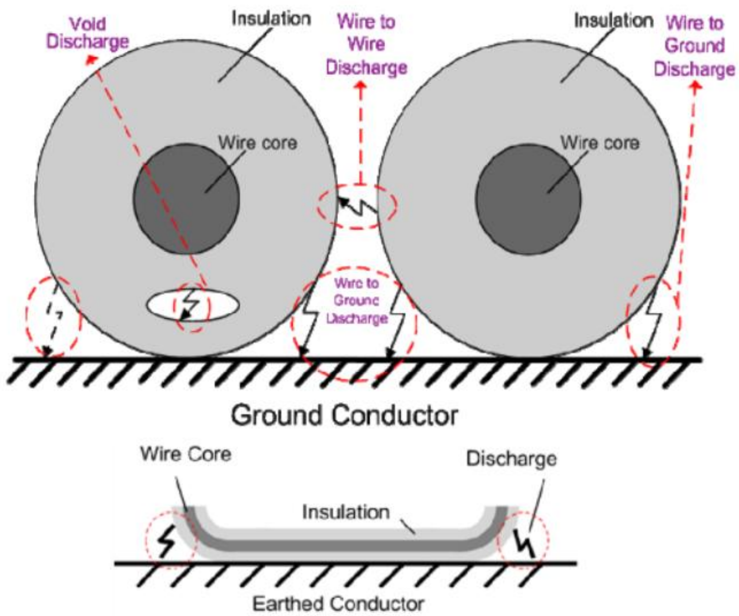

Figure 3-1. *Schematic Drawing of Possible Discharges for Aircraft-Wiring Including Internal and Surface Partial Discharges*

Townsend discharge takes place in a uniform electric field stress by the collision of free electrons with atoms or molecules to produce the secondary emission. It requires a large enough electric field to transfer adequate energy to the electrons between collisions, so the subsequent collisions produce more electron-ion pairs. The number of newly produced ions by collision is defined as primary ionization coefficient (α), distance between two electrodes and initial available electrons are the parameters in progression of this kind of discharge. A second form of Townsend equation was derived by including impact ionization of molecules by positive ions (β), Townsend's secondary ionization coefficient (γ), and attachment coefficient (η). The succession of avalanches will result in the formation of conductive channels (aka electric trees) and finally the breakdown of insulation once the channels create a conductive bridge across the insulation [4][5][6][7][8][9][10][11].

Streamer discharge has been defined by considering space charges for gas insulated medium subjected to high electric field stresses (αd >20) and non-uniform electric field. Electron avalanche initiated typically by thermally stimulated emission of an electron from the cathode will develop rapidly toward the anode. Spherical concentration of electrons (head of streamer) moving toward the anode broadens because of diffusion, and static remaining positive ions form the tail of the streamer. This formation of separate positive ions and negative electrons will induce space charges which will enhance the electric field (E-field) between electron head and anode, and positive tail and the cathode. This can initiate secondary electrons contributing to rapid development of the streamer.

In addition to collisional ionization and thermally stimulated emission as governing factors, volume thermal ionization in longer gaps at high E-field stresses or across dielectrics can result in another kind of discharge called leader discharge which produces large current flow. It has been generally accepted that precursor of the leader discharge is a series of streamers, and leader forms from the stem of streamer discharges in heated gas due to Joule effect. Charges transferred through this highly conductive channel to the tip of the leader can initiate another series of streamers, and again leader can be initiated from this streamer zone due to thermal ionization.

A higher electric field on the tip drives further propagation of a discharge. Two factors can reduce the electric field on the tip of the leader: (1) A longer leading channel can have higher voltage drop across the leader which reduces the electric field in the tip. (2) The induced opposite charges cover the tip of the leader and reduce the local electric field and prevent further development of the discharge and radial expansion of the leader channel. Positive leaders generate conversion zone in their tips within which cold streamer zone converts to hot leader channel; however, in negative leader, stepped propagation will occur and plasma inhomogeneity in the streamer zone forms a space stem. In this stage, the negative corona is in the same direction as the main leader, and positive corona is in the opposite direction. Space leader will occur due to the increase of Joule heating in the space stem. This process of space leader formation has been considered the fundamental stage in the leader progression [12].

3.1. Physical Process of Different Types of Partial Discharges

Corona discharge, based on the definition of IEC 60270:2000 [13], is the form of discharge occurring in gaseous media around the conductors remote from solid or liquid insulation. To understand the mechanism of this type of discharge, the phenomenology of positive and negative discharge should be considered separately. The behavior of ions and potential gradient would be different in positive and negative polarities. The space charge behavior and the electron attachment cross section for the gas or gas mixture medium can have significant impact on propagation of corona discharge [14]. In negative corona discharge, Trichel pulse activity is the initial phase [15]. These pulses convert to pulseless glow discharge at higher electric field intensities. Then, the glow discharges extend and develop into negative streamers.

In positive corona discharge, burst pulses develop accompanied by onset streamers. These burst pulses at high electric field condition develop into pulsating glow discharge. Pre-breakdown streamers occur before the final arc between electrodes.

Internal partial discharge is closed discharge that occurs in low permittivity regions areas inside the high permittivity dielectric materials. (Fig. 3-1). The electric field inside the void or any weak dielectric spot inside the electrical insulating materials is determined based on capacitive property of insulation and the void geometry under AC voltage. When a discharge takes place inside the void, residual charges accumulate at the gas-solid interface and the electric field induced by the charges reduces the electric field inside the void, which can suppress the next discharge because of the reduced internal E-field. Discharge recovery time inside the void depends on surface charge decay. Since DC discharge recovery time is much higher than AC recovery time, the partial discharge occurrence rate occurrence rate is lower for DC applied voltage [16]. In addition, in general, at room temperatures the PVID under AC is at a lower voltage than under DC due to the differences between the resistivity and permittivity ratios of air and the dielectric. The temperature dependence of the PDIV is much higher under DC because the resistivity of the polymer is more sensitive to temperature than is the permittivity.

Surface discharge occurs on the surface of dielectric exposed to high tangential electric field and is a type of dielectric barrier discharge [17] (e.g., Lichtenburg discharge). Special high voltage electrodes such as a needle and sphere generate a highly non-uniform electric field and initiate transport of injected charges on the surface. Polarity is important in any type of discharge in a non-uniform electric field.

The development of positive streamer discharge starts via attracting free electrons to the anode with sufficient energy to form the electron avalanche. The concentration of charged particles distorts the geometric electric field. A streamer forms where there is a high density of positive ions (front head). Streamer develops due to presence of seed electrons from photoionization and photoemission processes and terminates when the streamer tip electric field is not high enough to accelerate electrons sufficiently between collisions to ionize the molecules.

For negative streamer discharge, high energy electrons will accelerate away from the cathode. Low mobility positive ions settle in the vicinity of the cathode due to electron avalanche along the streamer discharge and form plasma [18].

Treeing breakdown is an important factor controlling the long-term breakdown process of polymer insulating systems, in which successive growth of partial degradation (treeing) takes place until the complete failure. In the laboratory, such treeing is typically initiated from the tip of a point electrode with radius of curvature less than 20 μm and can be divided into two stages: tree inception and tree propagation. The tree inception is defined as a point with an observable tree channel reaching a critical length of 20 μm, large enough to support the discharge [19].

The tree channel can be initiated at some time after the application of the voltage less than the breakdown stress, during which no gas discharge with a charge greater than 1 pC can be detected. In other words, there is an induction period for the tree inception that is a function of AC voltage and temperature, as shown in Fig. 3-2 [20].

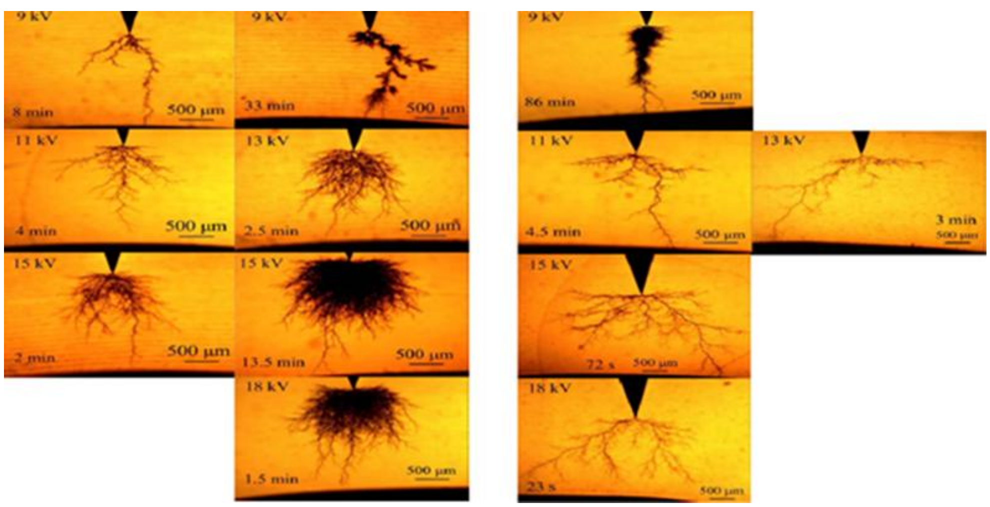

Figure 3-2. *Electrical treeing in XLPE at 50°C (left) and 90°C (right). Treeing at 50°C shows tendency of forming bush-type pattern while treeing at 90°C results all branch-type patterns with much faster propagation speed*

Upon the electric tree inception, the tree channel grows due to repetitive gas discharges within the channel. Its propagation is affected by the voltage waveform and magnitude, physical nature of polymer insulation, pressure, and temperature, etc. These result in patterns of tree shape, generally divided into branch-type trees and bush-type trees. For instance, tree propagation behavior in polyethylene at various temperatures as a function of time after the voltage application has been reported in literature [21]. At 30 °C, for instance, tree shapes at 10 and 12 kV are branch-type, while those at 14 and 16 kV change from branch-type to bush-type as time elapses. Tree morphology has been linked to the electron free path [22] which is a function of electron energy. So, tree shape and propagation depend upon the gas pressure and the chemical composition [23] of decomposed molecules inside the tree channel.

As the temperature and pressure equilibrate, the tree channel starts again to extend from one of the bush-type channels. At a temperature of 80 ^{o}C, the tree shape remains branch-type until complete puncture-through, because of the lowered gas pressure inside the tree channel due to increased gas diffusion at high temperatures. These observations are in general agreement with a recent paper in which treeing in XLPE was studied at 50 ^{o}C and 90 ^{o}C, as shown in Fig. 3-2, with the latter showing only branch-type trees growing with faster propagation speed.

In general, following observations have been obtained via extensive experiments regarding the tree propagation: (1) tree propagation is induced by gas discharge in the tree, (2) the discharges are generally pulses with durations of <0.1 μs; (3) the electric potential of the electrode transferred to the tip of the old tree channel through the conductive plasma produced by a gas discharge; (4) the diameter of the tree channel is of the order of μm and expands with repetitive gas discharges.

The approach for progressing from physics-based and empirical/data- informed modeling of small length scale defect generation and failure phenomenon to a reduced order life model has been developed. A summary of the physical mechanisms in the proposed framework and a keyworded description of each step can be found in Fig. 3-3.

Physical/numerical mechanism	Approach
Dimensionality	2.5 (interfacial) & 3 (fullscale)
Pre-treeing (induction period)	Induction period
Crack propagation	Phase Field
Field enhancement at voids	Continuous Surface Force
PD within the crack/void/tree	Drift Diffusion + Immersed Boundary Method
Charge Transport and field distortion in bulk (MC)	Monte Carlo/Green's function
Flash temperature (electrothermal aging)- reversible effect	Monte-Carlo/Fourier's function
Flash temperature (electrothermal aging)- irreversible effect	Monte-Carlo/Localized pitting
Full-scale computational tractability	Physics-based AMR
Post-AMR curvature correction	Discrete sampling of fully-resolved solution

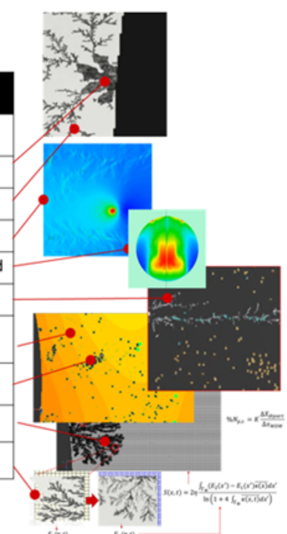

Figure 3-3. *Summary of the physical mechanisms in the proposed framework and a keyworded description of how they are addressed.*

3.2. Defect Propagation

In the last few decades, models were proposed to characterize the degradation mechanism of cable insulation [24][25]. The models can be divided into two main categories, namely, statistical models and physics-based models. Statistical models use statistical analysis to describe the failure of dielectric solids by fitting experimental data to statistical distributions, including Weibull distribution [26], log-normal distribution [27], and Johnson SB distribution [28]. Different from statistical models, physics-based models include the mechanisms of one or more physical processes, such as the dielectric breakdown model [29][30] the discharge-avalanche model [31] and the field-driven tree-growth model [32]. Pietronero et al. proposed that dielectric breakdown processed are stochastic, and the growth of an electrical tree is not just governed by the local electric field but over the points of the highest probability of growing. Dissado et al. [33] describe the electrical tree propagation through a discharged-avalanche model. However, the model requires some parameters, such as the characteristic time and the fractal dimension, which are hard to measure in practice.

While existing models provide insight into the mechanism of electrical treeing, the simulation of tree propagation is based mainly on statistical models or by reconstructing the intricate microscopic details. In this work, inspired by the similarity between dielectric breakdown and brittle fracture, a phase-field model is introduced to simulate the initiation and propagation of electrical treeing.

3.2.1. Defect Tracking in Space and Time

The free energy formulation adopted here is an extended variation of the form originally developed to simulate crack growth in materials [34][35][36][37]. The direct handling of the microscopic details in the process zone can be avoided by employing a Griffith-type energy criterion of the propagation of an electrical tree. This is consistent with the project objective to provide reliable estimates of growth rate.

The current formulation accounts for the role of electrical stress (i.e., Maxwell's stress) on the growth of the electrically induced channels/cracks. This phase field formulation is informed by an electric field model. The phase field formulation for electric-tree propagation is an interface tracking approach based on the principle of free energy minimization during crack formulation where the free energy, E_Φ, is expressed as,

$$E_\Phi = \int dV \left[\frac{1}{2} D_\Phi (\nabla\Phi)^2 + V_{DW}(\Phi) + \frac{\mu}{2}\Theta(\Phi)(\epsilon^2 - \epsilon_c^2)\right] \quad \text{(I-1)}$$

Here, Φ is the state of the material (= 1: broken, = 0: unbroken) and $\epsilon_c$is the critical strain rate. $V_{DW}$is a double-well potential, e.g.

$$V_{DW} = \frac{1}{4}\Phi^2(1-\Phi)^2 \quad \text{(I-2)}$$

The Allen-Cahn free energy minimization during crack propagation,

$$\frac{\delta E_\Phi}{\delta \Phi} = -m\frac{\partial \Phi}{\partial t} \quad \text{(I-3)}$$

The phase field transport equation is:

$$m\frac{\partial \Phi}{\partial t} = \gamma\nabla^2\Phi + U'(\Phi) + \delta'(\Phi) * (\varepsilon_\Phi - \varepsilon_c) + H(f_E - f_{cr})\frac{\partial f_E}{\partial \Phi} \quad \text{(I-4)}$$

where,

1. Φ, is the phase-field with its value indicating the status of the material ($\Phi = 1$, indicates cracked material, i.e., electric tree, $\Phi = 0$ indicates non-cracked bulk).
2. The term to the left of the equal sign drives the kinetic of the crack propagation with m as the kinetics/mobility coefficient. The first term on the right controls the thickness of the crack (width of the tree channel) with γstanding for the surface energy across defect/bulk interface.
3. The second term on the right hand is a double-well potential which is proportional to bulk material properties and fracture toughness and serves as an energy barrier for crack growth.
4. The third term captures thermal stresses.
5. The last term is the electric stress where $H(f_E - f_{cr})$ is Heaviside step function with f_{cr} related to the local electric breakdown limit of the material and f_E is the electric stress.

The electric stress term is expanded as follows,

$$\frac{\partial f_{\mathrm{E}}}{\partial \Phi} = [-6(\Phi^2 - \Phi^3)\Delta\epsilon][(\nabla\Psi \cdot \nabla\Psi)] - \frac{\epsilon(\Phi)}{2}\frac{\partial}{\partial\Phi}(\nabla\Psi)^2 \quad \text{(I-5)}$$

Here, $\Delta\epsilon$ is the permittivity differential between the bulk and polymer. An asymptotic-based electric field model captures the effect of the discontinuity of polarization across the tree channel on the direction of the electric field in the polymer's bulk. With Ψ being the electric potential which is derived through perturbation of full Poisson equation for electric field distribution in the bulk:

$$-\nabla\Psi = \vec{E} = \vec{E}_{ext}(x) + \vec{E}_T(\vec{x});\ \vec{x} \in \Omega \quad \text{(I-6)}$$

The first term on the right-hand side of the equal sign is the geometric (background E-field) which follows a standard Laplace (charge-free) or Poisson equation:

$$\nabla \cdot \vec{E}_{ext} = \nabla^2(\Psi_{ext}) = 0 \quad \text{(I-7)}$$

The 2nd term on the right-hand side, $E_T(x) = -\nabla\Psi_T$ refers to the "distortion" of the electric field as the result of permittivity jump across the defect. Assuming the region within the channel ($\Phi = 1$) is highly polarized, one can infer $\epsilon_T \gg \epsilon_B$ where ϵ_T and ϵ_B, respectively correspond to electric permittivity in the tree channel and in the bulk. Under this assumption, one can write the distorted electric potential Ψ_T as:

$$\Psi_T = \Psi_0 + \gamma\Psi_1;\ \gamma = \frac{\epsilon_B}{\Delta\epsilon}; \Delta\epsilon = \epsilon_T - \epsilon_B \quad \text{(I-8)}$$

The zeroth order term, Ψ_0, is solved through the following transport equation [38]:

$$(f'(\Phi)\nabla\Phi) \cdot \nabla\Psi_0 + f(\Phi)\nabla^2\Psi_0 = (\nabla f \cdot E_{ext}) - \frac{\rho_0(\mathbf{x})}{\epsilon_0};\ \rho_0(\mathbf{x}) \sim O(1) \quad \text{(I-9)}$$

And the first order term, Ψ_1 is solved through:

$$(f'(\Phi)\nabla\Phi) \cdot \nabla\Psi_1 + (f + 1)\nabla^2\Psi_1 = 0 \quad \text{(I-10)}$$

For $\frac{\epsilon_T}{\epsilon_B} \sim O(10^4)$, the first order approximation above will yield estimated error of $O(10^{-8})$ against the full-blown solution to the Poisson Equation ($\nabla^2\Psi = -\frac{\rho(x;\, x \mapsto \Omega_\Phi)}{\epsilon(x)}$), so it is acceptable for this analysis.

The model assumes an already "initiated" electric tree with some *ad hoc* charge distribution (ρ_0) and hence focuses on the degradation mechanics rather than the electrostatics of the problem. The model assumptions and restrictions are provided in Table 3-1.

Table 3-1. *Defect propagation model assumptions and restrictions*

Assumption	Restriction
All mechanical properties are isotropic, $E, \nu,\ K_I \neq f(\Phi(\mathbf{x}),\ \mathbf{x})$	E, and ν can be spatial (anisotropic and/or statistical)
Thermal properties are function of crack location, $\eta = f(\Phi(\mathbf{x}), \mathbf{x})$	Inputs needed for defect properties (degenerated polymer)
Electrical properties in the bulk are constant, $\epsilon_B \neq f(\mathbf{x})$	Will have to reformulate the asymptotic analysis otherwise
External field is established in presence of no space charge	Can switch to Poisson solver if this isn't the case
Space charge is abundant in the defect (highly polarized, $\epsilon_T \gg \epsilon_B$)	The electric field model is based on this assumption. Higher order terms will be needed if $\epsilon_T \gtrsim \epsilon_B$
Current formulation is for DC field; $E \neq f(t)$	Electric transport equations can be solved in Fourier space and transformed into temporal space in AC field

A series of simulations were conducted with a typical set of input parameters for material properties and some notional inputs for charge density within the tree channels. These simulations demonstrate the ability to produce electric tree structures and to understand how sensitive this structure is to the numerical values of these parameters.

A snapshot of defect structure for two hypothetical charge densities with similar material properties is shown in Fig. 3-4. The associated E-field distribution with the distorted E-field, which is kept up to the 1st order term in the asymptotic expansion, eq. I-8 is also shown to demonstrate how the E-field is altered as the result of the permittivity discontinuity across the defect.

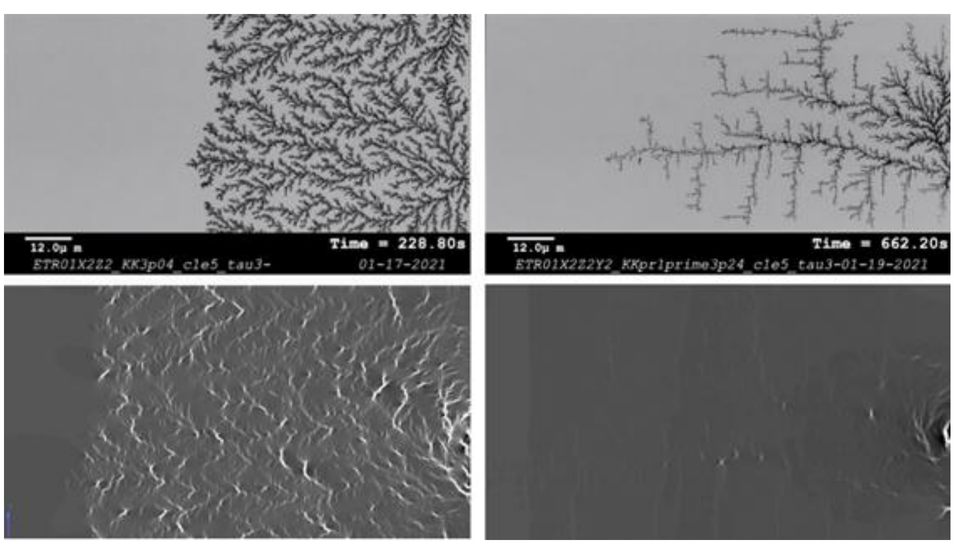

Figure 3-4. *Electric-tree propagation (top) and corresponding electric field distribution (bottom) for two hypothetical charge density inputs: q = 10^4 C/m^3 (left), q = 5x10^3 C/m^3 (right)*

3.2.2. Thermal Effects

The third term in the phase field formulation can be recast to capture variation of bulk properties with temperature as well as accounting for thermal stresses as the result of temperature gradient. Specifically, the driver term in phase field formulation takes the following form [39].

$$\varepsilon_{\phi} = \frac{1}{4(1-\nu)}\left(\varepsilon_{kk} - 2T(x)\right)^2 + \frac{1}{2(1+\nu)}\left(\frac{\delta_{ij}\varepsilon_{kk}}{2}\right)^2 \quad \text{(I-11)}$$

$$\varepsilon, \nu = f(T) \neq f(\phi) \quad \text{(I-12)}$$

Where the temperature is solved through energy transport equation,

$$\frac{DT}{Dt} = \alpha_T(\mathbf{x})\nabla^2 T; \mathbf{x} \in \mathbf{\Omega_B} \cup \mathbf{\Omega_T} \quad \text{(I-13)}$$

$\alpha_T$is thermal diffusivity of the bulk including defects and cracks,

$$\alpha_T = \alpha_B f(\Phi) + \alpha_T\left(1 - f(\Phi)\right); f(\phi) = 4\Phi^3 - 3\Phi^2 \quad \text{(I-14)}$$

The evolution of the electric tree, which is impacted by changes in bulk modulus with temperature at 22 °C, 75 °C and 100 °C, can be found in Fig. 3-5. Please notice, part of the plot is reproduced from reference [40], in order to demonstrate the PE bulk properties changes with the temperatures. It can be observed that, because of the dependence of the bulk modulus dependency on the temperature, it appears that higher temperatures reduce the density of the defect channels and yield a slightly faster progression rate. This observation seems to be consistent with previous experiments of the effect of temperature on electric treeing [41].

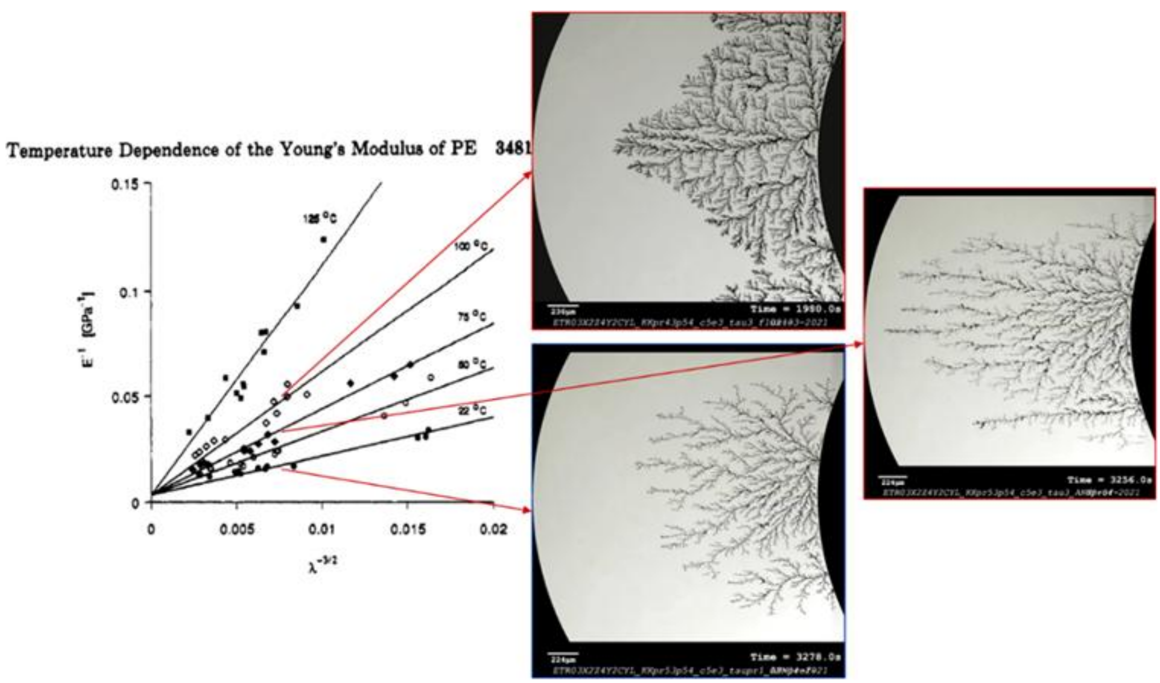

Figure 3-5. *Impact of bulk modulus temperature dependency on electric tree formation*

3.2.3. AMR (Adaptive Mesh Refinement) for Extension to 3D at Full Scale

The phase field method has stringent resolution requirements to accurately predict the interface location and its evolution over time. An Adaptive Mesh Refinement (AMR) meets those requirements in the region where the interface is located without having to penalize the computation elsewhere in the domain. The requirement for mesh adaption is based on the location of the interface, $\nabla\Phi > 0$, and the level of refinement, n, is determined based on the characteristics of the interface,

$$\frac{\Delta x(\mathbf{x})}{\Delta x_0} = n^{-1}(\mathbf{x}); n = f\left(d_0(\mathbf{x}), \alpha(\mathbf{x})\right) \tag{I-15}$$

where $d_0 = \sqrt{\frac{E}{\sigma}}$ and $\alpha = \frac{d_0}{\gamma}$, are directly linked to local bulk properties (elasticity modulus, surface energy and diffusion coefficient) [42]. This allows for efficient calculation of interface evolution in three-dimensional space and an example is shown in Fig 3-6. Here the bulk is geometry is represented through a relatively coarse grid, sufficient to resolve field distribution (as well as its distortion due to defects and voids, see next section), and the interface location is adaptively refined with the level of refinement linked to local bulk properties. One can also conceivably implement a coarsening criterion after the defect tip has sufficiently progressed downstream which significantly reduces the computational overhead at the expense of introducing error into the total electric field calculation.

Figure 3-6. *Schematic illustration of Adaptive Mesh Refinement (AMR) for Phase-Field simulation of electric tree propagation*

While AMR makes it possible to perform calculation of phase field at the length scale of the component, it tends to smear out the details of the tree morphology that would have otherwise been captured if using a uniform cartesian grid. While macroscopically, these details may be of little relevance, the curvature associated with the tree morphology near the tip can affect overall electric stress prediction in the bulk and could potentially result in an overestimation of life under tree propagation.

To alleviate this problem, a discrete sampling approach has been developed. In this approach the tree front is sampled discretely at a given time over the bulk (referred to background) grid and for each sample, an overset uniform fine grid is generated (referred to as foreground grid) within which a phase field stepping is conducted to extract tree morphology. The calculated tree in the background at a given time is then subtracted from the foreground tree and the difference is used to calculate source term that needs to be added to the Poisson equation in the bulk to reproduce the electric stress. A sampling correction factor is applied which is related to the number of samples. When the correction factor approaches 1, the number of samples increases in order to cover the entire tree front.

A schematic of discrete sampling approach is presented in Fig. 3-7. The computational saving associated with AMR compared to a fully resolved simulation (2D) as well as the overhead associated with discrete sampling method is summarized in Fig. 3-8. In this figure, the black line corresponds to a fully resolved calculation (no AMR and no discrete sampling) and the colored lines correspond to AMR with discrete sampling calculations, where β is an indication of the size of the samples (for fully resolved calculations) and f refers to the frequency of discrete sampling over the course of phase field simulation. For example, if f equals to 50, it implies calling the discrete sampling algorithm every 50 phase field time-steps. Expectedly, larger sample size and more frequent sampling increases the computational overhead, eventually approaching the fully resolved calculation.

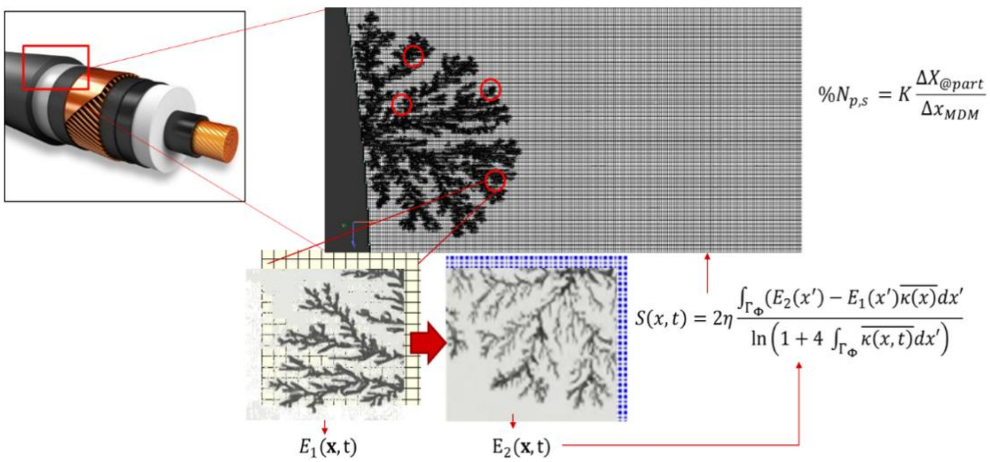

Figure 3-7. *Discrete sampling for curvature correction*

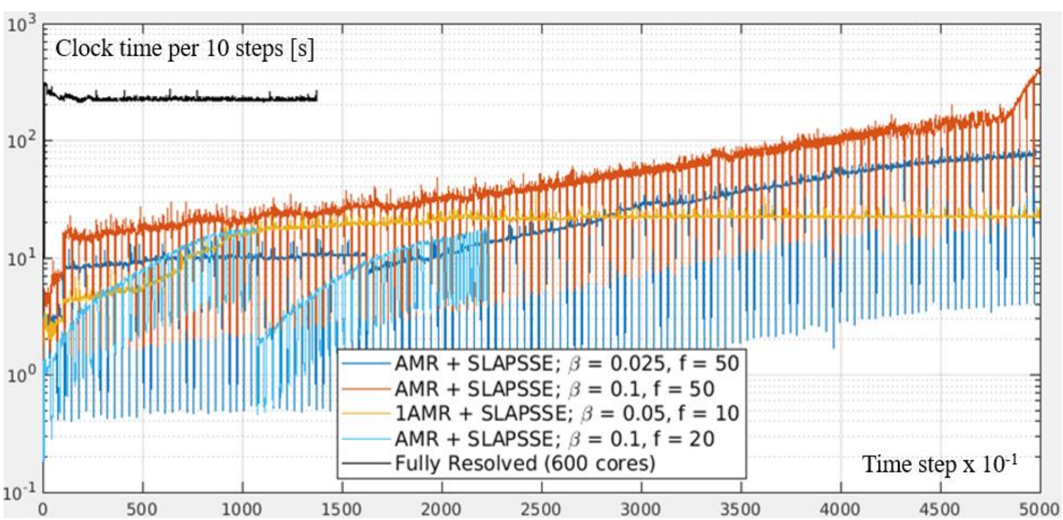

Figure 3-8. *Computational time decreases enabled by ARM and discrete sampling approach. Note: SLAPSSE -Spatially Largely Asynchrony Process for Simulation of Simultaneous Events*

3.3. Continuous Surface Field (CSF) Method

When an applied electric stress over some distance exceeds the breakdown strength of the polymer, the partial dielectric breakdown will be expected to occur with a small time-lag, and then the tree channel is formed. Breakdown is a weak link phenomenon. The field is applied to a cable, for example, and the partial discharge occurs at the location at which the lowest voltage meets initiation criteria.

The electrical field at the tip can be approximated as $\frac{2V}{R\ln\left(1+\frac{4D}{R}\right)}$ with R being the cavity/protrusion radius of curvature and D being the characteristic electrode-to-electrode distance across which voltage V is applied. If the tip field, modified by the surrounding space charge, exceeds the intrinsic breakdown strengths of the polymer, the tree channel is initiated purely due to the partial dielectric breakdown of the polymer. A modified version of Poisson equation is needed to retrieve field enhancement as the result of asperities/cavities in the bulk or along conductor/insulator interface.

For an arbitrary cavity located in space as shown in Fig. 3-9, the field is enhanced due to the curvature at the cavity wall. In reality, and if the cavity was to be perfectly resolved, this would result in a boundary condition along the interface. This could potentially lead to excessive computational penalties if each individual cavity and asperity is tracked and resolved.

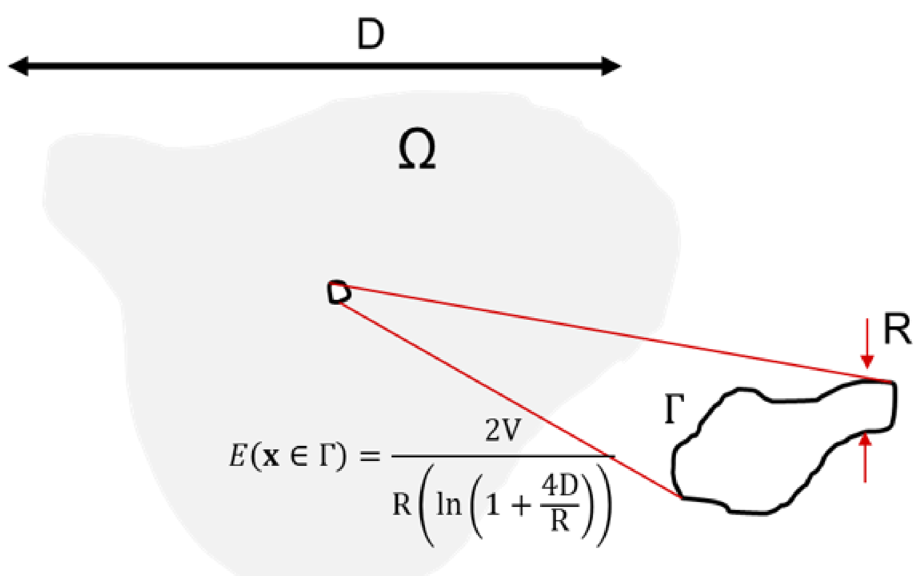

Figure 3-9. *Arbitrary cavity in space with curvature R*

The alternative approach developed here represents a statistical distribution of voids and cracks with quantifiable curvature with a source term in Poisson equation, hence this is a Continuous Surface Field (CSF) method. The approach presented here is inspired by the Continuous Surface Force approach [43] where the effect of surface tension on an arbitrary liquid or gas interface is represented through a source term in the momentum transport equation. Similarly, the objective here would be to account for the role of cavities and protrusions on the electric field distortion through a source term in the Poisson equation. The formulation takes the following form:

$$-\nabla^2\Psi = \nabla \cdot E_{ext} = \frac{\rho_0}{\epsilon} + S(\vec{x} \to T_i); \quad \text{(I-16)}$$

$$\Psi(x_1) = \Psi_{ext},\ \Psi(x_2) = 0 \quad \text{(I-17)}$$

Where the right-hand side is the spatially defined source term as function of curvature distribution of the voids and cavities:

$$S(x) = \frac{2\Psi_{ext}\kappa(\vec{x}_3)\nabla\eta(\vec{x})}{ln(1+4D\kappa(\vec{x}_3))} - \frac{\rho_0}{\epsilon_B} \quad \text{(I-18)}$$

The snapshot of the electric tree, which is calculated with some arbitrary voids within a 2D bulk, is shown in Fig. 3-10, with the comparison between the fully resolved approach and CSF approach.

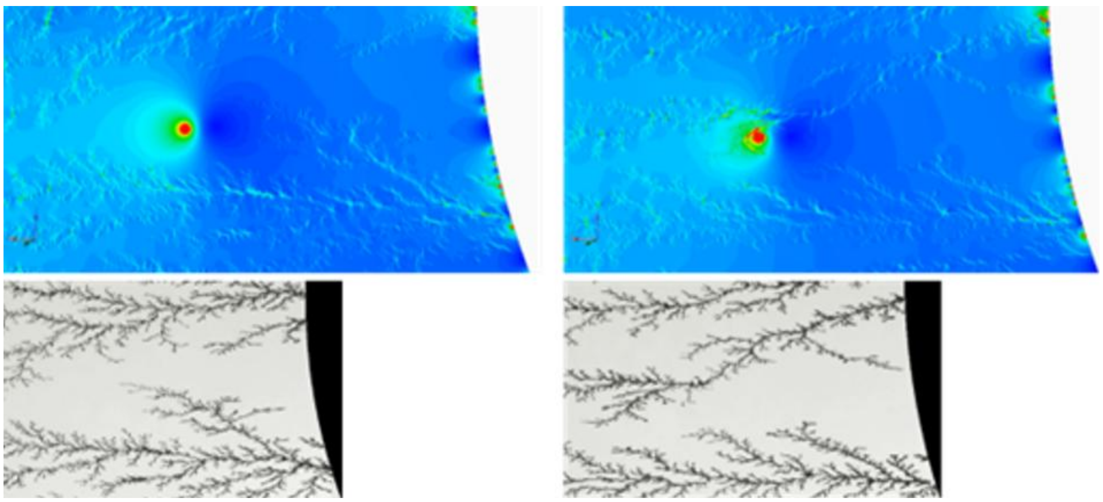

Figure 3-10. *Snapshot of electric field distribution and tree structure using (left) fully resolved cavity distribution and (right) cavities represented through CSF*

The CSF approach largely retrieves the field distribution and resultant defect structure, except for slight disparities when the defect is approaching the actual defect location. It is worth noting that the computational overhead of CSF is approximately 20 times smaller than the fully resolved counterpart for this demonstration, which makes it a viable approach especially extending it to the full-scale simulation. In addition, in this approach, only a statistical representation of void/defect curvature distribution will be sufficient to retrieve their impact on bulk field distortion.

3.4. Electromechanical Aging

Besides material degeneration as the result of electric stress and tree propagation, the material can undergo the so-called "aging" due to electromechanical effects. The key mechanics include pre-treeing zone of crazing formation during induction period, localized material damage as the result of charge/interface interaction in the bulk, and void generation as the result of environmental effects (e.g., thermal cycling, mechanical stress, etc.).

3.4.1. Pre-Treeing Void Generation/Craze Formation

The tree channel can be initiated at some time after the application of the voltage less than the breakdown stress, during which no gas discharge with a charge greater than 1 pC can be detected. Various models have been proposed to account for this induction period, such as the interaction between high energy electrons accelerated by the electric field and the end radicals of polymer structure [44], fatigue breakdown due to the Maxwell mechanical stress associated with repeated voltage application [45], a zone of crazing, and electro-mechanical fracture under space charge limiting field [46][47]. For instance, the crazing zone model describes that under the repeated electro-mechanical stress induced around the needle point by AC voltage application works, the induced mechanical stress perpendicular to the direction of the electric field appears in an elastic material such as a polymer by which the crazing might be caused starting from a micro-defect such as a micro-void in the polymer when the stress exceeds a critical value. At a stage, the crazing grows into a void-crack. Thus, the induction period of tree inception corresponds to the time to the appearance of void-cracks by way of crazing.

Here, an "induction-period" model for the zone of crazing has been adopted which accounts for the material degeneration of an existing void/crack prior to formation of an electric tree. Under low field and at low temperature, carriers can only transport between these localized states through hopping or tunneling. The model is based on an earlier work on "zone of crazing" where the Maxwell's pressure is computed as the result of charge transport through trapping and de-trapping:

$$p(t) = \epsilon E_l^2(t)\left(\frac{V_0\kappa(x)}{E_l(t)} - 1\right) \quad \text{(I-19)}$$

Due to the intermittent nature of this phenomenon, stress is accumulative (analogous to fatigue stress). Therefore, the accumulative stress is computed throughout time,

$$P(t) = \int_0^t p(t')dt' \quad \text{(I-20)}$$

The material breakdown occurs when accumulated stress exceeds a critical value, $P > P_{crit}$. An example of crazing zone around different initial void topologies can be found in Fig. 3-11. Interestingly, the morphology and size of this zone of crazing is dependent on the initial morphology of the void. The spherical void appears to be resulting in more "regular-looking" zone of crazing, while the irregularities of the non-spherical voids tend to extend into the crazing region.

It is also worth noting that as the result of more branching structure of the crazing region in the latter case, the subsequent crack propagation appears to be denser compared to the scenario of spherical void. One should note that the sparse appearance of the tree channels in the right-hand Fig. 3-11 is due to grid coarsening implementation, which is triggered some time after the crack front progresses downstream.

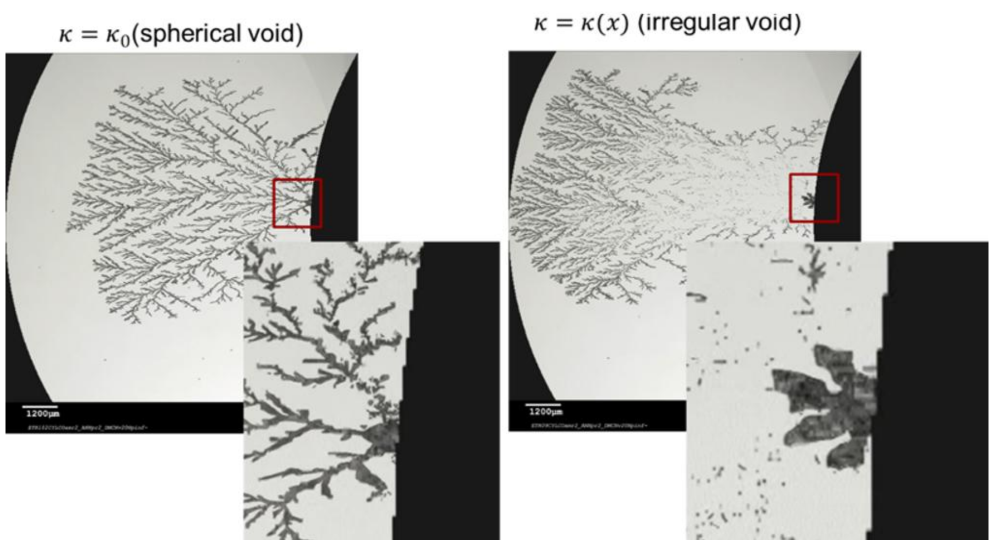

Figure 3-11. *Crazing zone around different initial void topologies*

3.4.2. AMR (Adaptive Mesh Refinement) for Extension to 3D at Full Scale

It is postulated that the polymer can suffer from localized degeneration (leading to polymer de-crosslinking and low-density regions in the bulk) due to charges colliding with interfaces of voids and trees. A schematic figure of such phenomenon is shown in Fig. 3-12 [48].

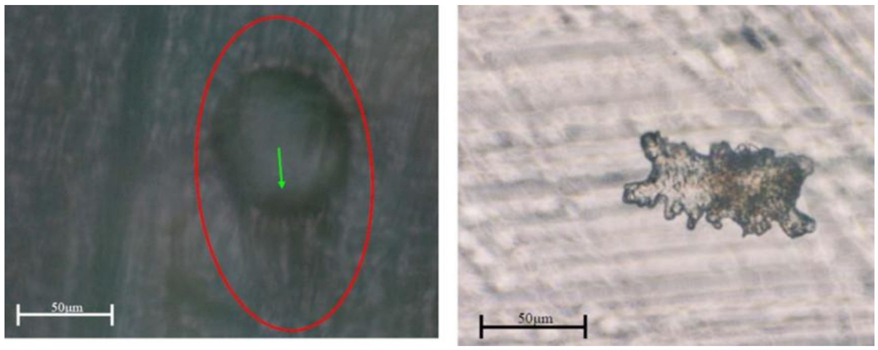

Figure 3-12. *Examples of localized degeneration due to charges colliding with interfaces*

This process happens over a much longer timescale than the tree propagation itself, but nonetheless could have ramification on overall electric stress and on how a given void evolves prior to tree initiation. A Monte-Carlo framework is employed for discrete charge transport in the bulk to incorporate the effect of charge collision onto existing interface in the polymer (the interface refers to any existing void/crack and developing electric tree channels within the polymer).

Upon impact of a given charge carrier to the interface, the resultant "flash-temperature" at the point of impact and throughout the entire bulk is calculated. The material then undergoes reversible and irreversible property charges as the result of this temperature change. The idea in the modeling approach is to calculate temperature rise as the result of ion/charge impact onto the interface. Due to linearity of energy transfer problem, if the temperature rise of one impact is calculated, then the total temperature rise can be simply superposed as the result of N impacts by:

$$\Delta T_{tot}(\vec{x},t) = \sum_{i}^{N(t)} \Delta T_i(\vec{x},t)\ ;\ \vec{x} \in \Omega;\ \ N(t): \#\ of\ impacts\ at\ time\ (t) \qquad \text{(I-21)}$$

The "flash temperature" rise as the result of one impact at location x_0 and time 0 (time axis can simply shifted by the collision time) is calculated through Fourier transform of the energy equation and leads to the following formula:

$$\Delta T(\hat{x},t) = \frac{q}{\rho c_p (4\pi t)^{3/2}} exp\left(\frac{-|\vec{x}-x_0|}{4\alpha t}\right) \qquad \text{(I-22)}$$

Where the heat generation rate, q, is related to the kinetic energy of the charge carrier:

$$q_i = m_i V_i^2 = m_i \left(\frac{d\vec{x}_i}{dt}\right)^2 = m_i \left(\frac{d\vec{x}_i}{dt}(t=t_0)\right)^2 = m_i \left[\frac{\vec{x}_0 - x(t_0-dt)}{dt}\right]^2,\ \vec{x}_0 = \vec{x}(t=t_0) \qquad \text{(I-23)}$$

The distinction between reversible and irreversible property change is addressed through some critical temperature criteria, above which the material undergoes a "pitting" damage (hence irreversible), and below which the material properties would be a function of temperature. While the variation of mechanical properties as function of temperature is straightforward, there is more empiricism when it comes to electric properties. For example, the electric conductivity can have noticeable variation with temperature [49][50],

$$\sigma(\mathbf{x},t) = \sigma_0 \left(\frac{E(\mathbf{x})}{E_0}\right)^{\nu} \exp\big(\alpha(T(\mathbf{x},t) - T_0)\big) \quad \text{(I-24)}$$

Which is adopted in the present framework.

A demonstration of localized degeneration as the result of charge impact is presented in Fig. 3-13. The darker regions in the right-hand figure correspond to the pitting regions as the result of charge impact which, interestingly, serve as new defect initiation sites due to local rise in the electric stress. As the result of these new initiation "sites", the ultimate defect distribution appears denser with larger accumulated electric stress in the polymer as shown in Fig. 3-14.

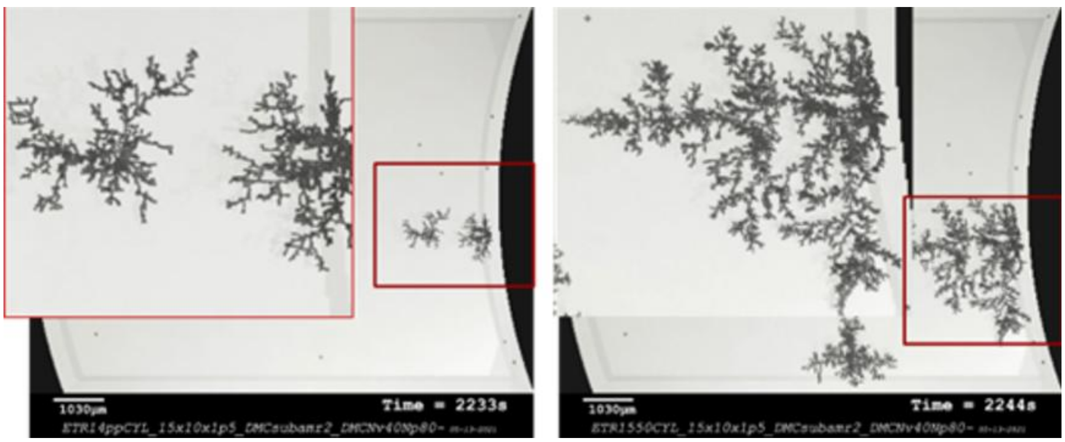

Figure 3-13. *Demonstration of defect propagation in presence of reversible property variation induced by charge impact (right) compared to an electric-treeing only simulation (left)*

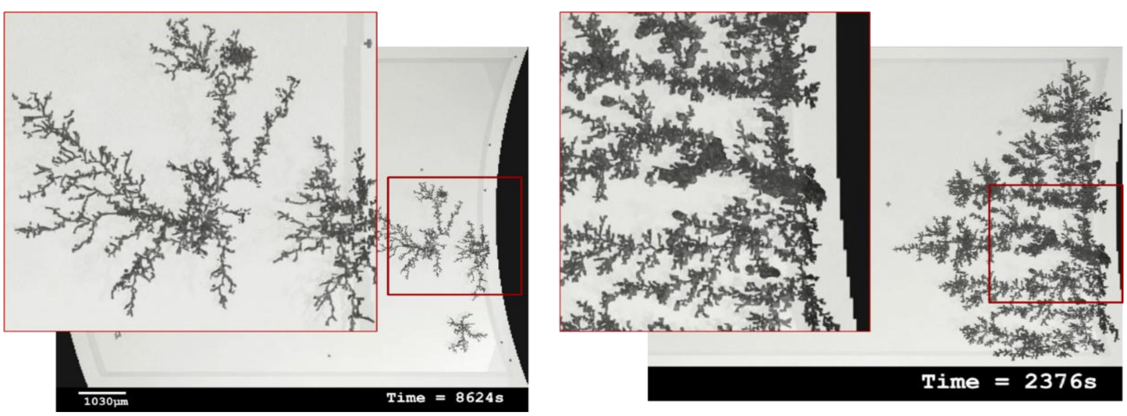

Figure 3-14. *Demonstration of localized irreversible degeneration (pitting) as the result of charge impact (right) compared to an electric-treeing only simulation (left)*

3.4.3. AMR (Adaptive Mesh Refinement) for Extension to 3D at Full Scale

For a DC field, charge relaxation at a void/defect interface is largely driven by absorption in the bulk as the external field has a non-zero average [51]. Charge accumulation in the bulk, driven by bulk electric properties and partial discharge activity in void/defect can distort the external E-field. Due to the stochastic nature of discharge-induced charge generation and absorption, this charge concentration, however, is dispersed and a continuum "charge cloud" approach, which is typically used for electrostatic problems is not valid.

Instead, a Monte-Carlo approach for generation and transport of charges and an analytical solution of Poisson equation with discrete sources is used to derive the resultant electric potential. The charges are being tracked as Monte-Carlo walkers through:

$$\text{for } \vec{x} \in \Omega_B: \quad \vec{x}_i(t) = \hat{E}(\hat{x})(2Ddt)^{\frac{1}{2}} \cdot \hat{x} + \hat{x}_i(t - dt) \tag{I-25}$$

$$\hat{x} = \sqrt{-2 \ln u}\, {}^{sin}_{cos}(2\pi v); \tag{I-26}$$

where $0 < u, v < 1$

At any given time, the electric potential as the result of a given charge at an arbitrary location, x_{pi} can be calculated as:

$$\Psi_i(\vec{x}) = \vec{\rho} G_i(\vec{x}: x_{pi}) = \frac{-\rho}{4\pi|\vec{x} - \vec{x}_{pi}|}; G \to 0, x \to \infty \tag{I-27}$$

In the presence of N charges at a given time, the electric potential then is a simple superposition of all the individual potentials:

$$\Psi(\vec{x}) = \sum_i \Psi_i(\vec{x}) = \frac{\vec{\rho}}{4\pi} \sum_i \frac{1}{|\vec{x} - \vec{x}_{pi}|} \tag{I-28}$$

As the result of this approach, field distortion in the bulk due to the presence of discrete charges is accounted for with minimum computational penalty. An instantaneous snapshot of charge distribution in the bulk is shown in Fig. 3-15 with the presence of electric tree and the resultant field distortion. The charge carriers travelling in the bulk (left hand figure), are colored based on emission origin: orange color indicates emission from voids or defects within the polymer and green color indicates emission from the tree channel interface. It is also noted that the emitting charges have statistically invariant bipolar distribution.

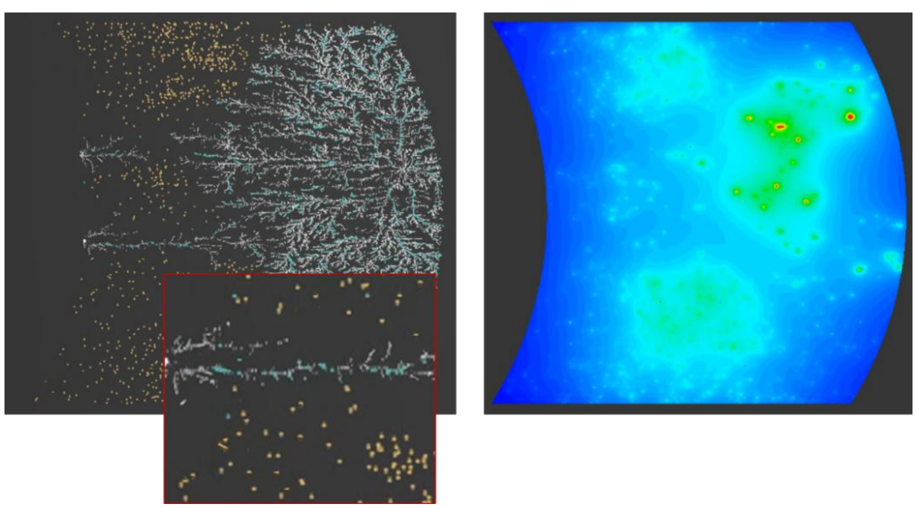

Figure 3-15. *Instantaneous tree structure and charge distribution in the bulk (left) and the resultant electric field distortion (right)*

3.5. Charge Transport due to Partial Discharge

Models of partial discharges have also received research attention as they improve our physical understanding and, in some cases, allow conclusions to be drawn on conditions within defects [52]. The foundational work in partial discharge modelling in polymer voids began with the work of Niemeyer in the 1990's [53]. More recently finite element and finite difference models have been developed that allow the electric field to be determined throughout the system [54][55][56][57].

Drift diffusion formulation: The formulation here is adopted by previous works on partial discharge modeling using drift diffusion model for three charged species which considers electrons and positive and negative ions. While this is an established approach and has been used in recent work on discharges in air in the literature, it is worth noting that in the premise of the integrated framework of polymer degradation due to these electric activities, it is possible to expand this model to more physically representative formulations, for example, plasma hydrodynamics models [58][59][60].

The model solves drift diffusion equations for the number densities of electrons ne, positive ions np and negative ions n_n

$$\frac{\partial n_e}{\partial t} = \alpha n_e|\vec{W}_e| - \eta n_e|\vec{W}_e| - \beta n_e n_p - \nabla \cdot \vec{\Gamma}_e + S_{\text{ph}} \tag{I-29}$$

$$\frac{\partial n_p}{\partial t} = \alpha n_e|\vec{W}_e| - \beta n_n n_p - \beta n_e n_p - \nabla \cdot \vec{\Gamma}_p + S_{\text{ph}} \tag{I-30}$$

$$\frac{\partial n_n}{\partial t} = \eta n_e|\vec{W}_e| - \beta n_n n_p - \nabla \cdot \vec{\Gamma}_n \tag{I-31}$$

where S_{ph} is the photoionization rate,

$$S_{\text{ph}} = \sum_{i=1}^{3} S_{\text{ph}i} \tag{I-32}$$

where each $S_{\text{ph}i}$ solves a Helmholtz equation

$$\nabla^2 S_{\text{ph}i} - (\lambda_i p_{O_2})^2 S_{\text{ph}i} = -A_i p_{O_2}^2 S, \tag{I-33}$$

And

$$S = \xi I;\ I = \alpha n_e|\vec{W}_e| \tag{I-34}$$

The corresponding fluxes for different charge carriers, Γ_i are,

$$\vec{\Gamma}_e = n_e\vec{W}_e - D_e \nabla n_e \tag{I-35}$$

$$\vec{\Gamma}_p = n_p\vec{W}_p \tag{I-36}$$

$$\vec{\Gamma}_n = n_n\vec{W}_n \tag{I-37}$$

and ξ = 0.0022 for the physical conditions under consideration [61]. S will be referred to as the photoionization source and is directly proportional to the collisional ionization rate [62], I. W_i corresponds to drift velocities for different charge carries,

$$W_i = \mu_i E^{\upsilon} \tag{I-38}$$

where α, η and β are the ionization, attachment, and recombination coefficients respectively; D_e is diffusion coefficient for electrons. The swarm parameters introduced by Kang are used in this work [63]. Poisson equation is used to solve for the electric field,

$$\nabla^2\Psi = \frac{-\rho}{\varepsilon_0\varepsilon_r}, \vec{E} = -\nabla\Psi \tag{I-39}$$

where charge density, ρ, is simply,

$$\rho = e\left(n_p - n_e - n_n\right) \tag{I-40}$$

The use of three charged species, electrons, and positive and negative ions, to simulate discharges in air has been widely used in the literature [64][65]. The demonstration/verification of this formulation is conducted for a spherical void surrounded by epoxy resin between parallel plate electrodes. The temporal evolution of electron and positive ion densities over a partial discharge cycle is shown in Fig. 3-16. In absence of a quantitative comparison, due, in part, to missing data (e.g., recombination and attachment coefficients), this formulation produces consistent partial discharge behavior with those presented previously [66].

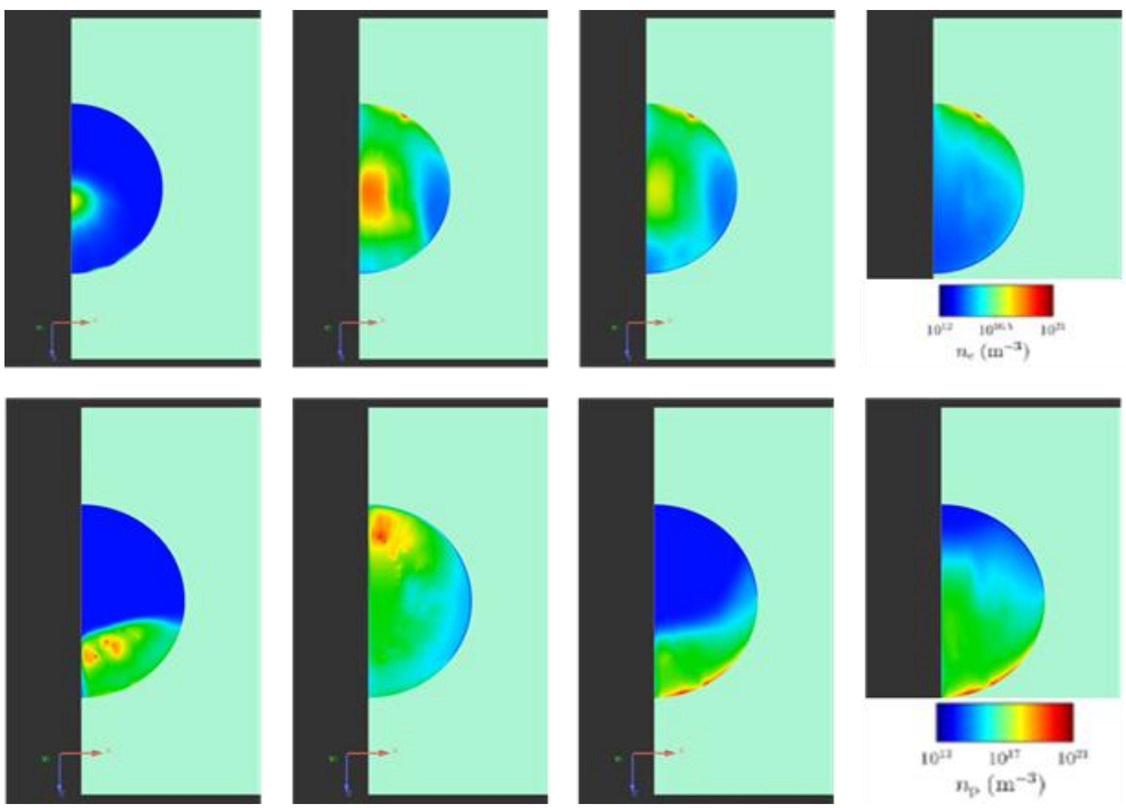

Figure 3-16. *Discharge dependent variables. top: electron number density, bottom: positive ion density. Temporal evolution from left to right: 1 ns, 20 ns ,30 ns, 100 ns*

In addition, one can calculate the apparent current pulse on the measuring electrode through,

$$I = \int_S J' dA \, ; \; J' = \frac{\partial}{\partial t}(\mathbf{n} \cdot \mathbf{D}) \tag{I-41}$$

where **D** is the electric displacement field,

$$\mathbf{D} = \epsilon_0 \epsilon_r \mathbf{E} \tag{I-42}$$

The calculated current for the spherical void demonstrator is shown in Fig. 3-17. Current pulses that are qualitatively like those observed in this work, i.e., with a magnitude in the range of mA with a growth time scale in the region of 5 ns and a decay in the region of 20–30 ns, have been reported in experimental and simulation work in the literature [67]. Partial discharges with these current pulses have been described as 'streamer-like' by Morshuis [68] and corresponded to the initial stages of discharge activity. The condition of this model is designed to replicate the experimental conditions.

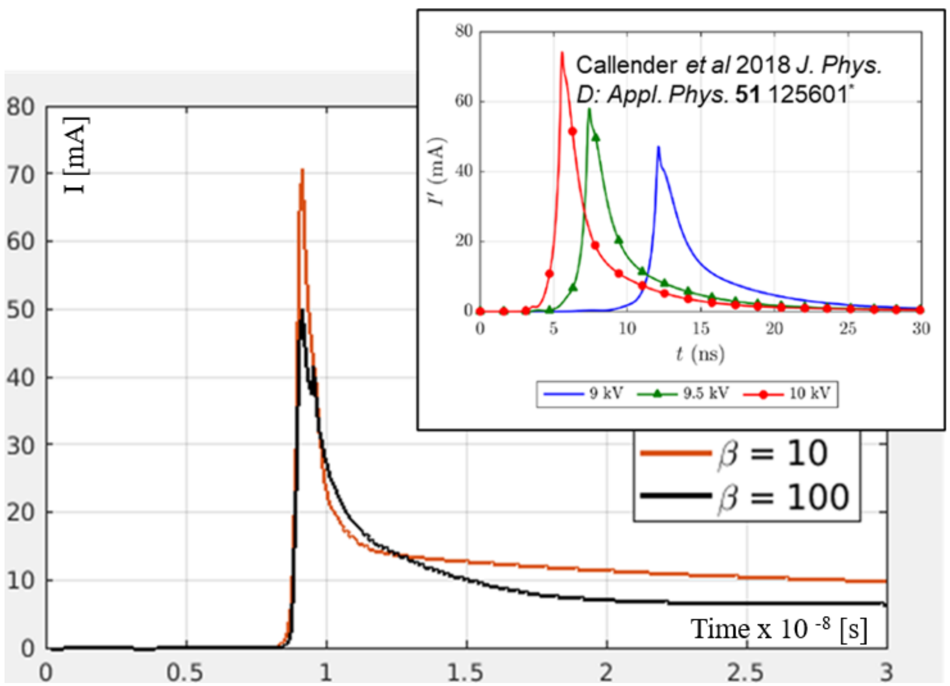

Figure 3-17. *Predicted apparent current on ground electrode at different applied voltages*

3.6. Immersed Boundary Method for Arbitrary Topologies

A conformal grid approach for solving the transport equations can become computationally intractable when dealing with complicated void and defect topologies, like within the electric tree channels. An Immersed Boundary Method (IBM) is adopted here for solving charge transport equations. In this approach, the computational grid remains Cartesian (same as the one used for defect propagation) and cells associated with the voids and tree channels are marked for partial discharge simulation as shown in Fig. 3-18.

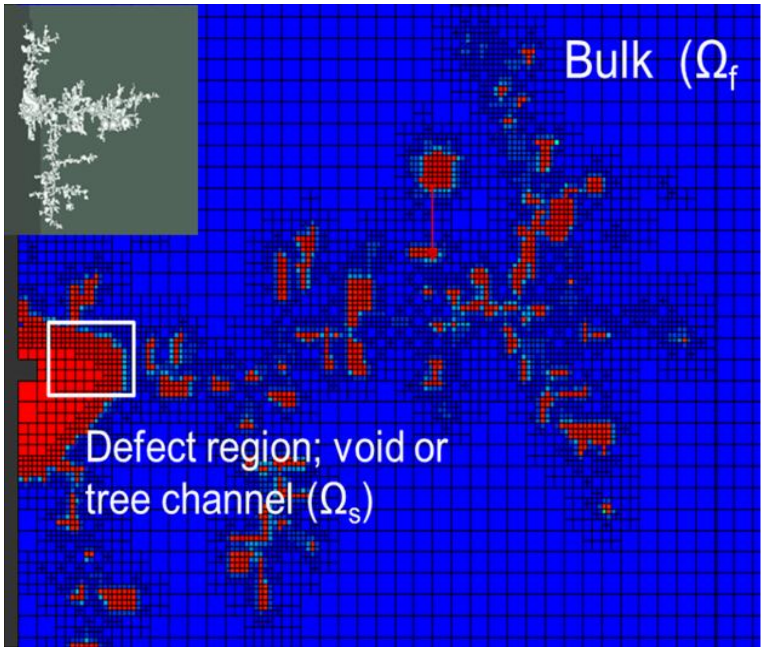

Figure 3-18. *Schematic illustration of Immersed Boundary Method (IBM)*

The charge and electric field transport equations take the following form,

$$\frac{\partial n_e}{\partial t} + b\nabla\Phi \cdot \nabla n_e = \sum S_e - \beta n_e n_p + \int_{\Omega_s} \boldsymbol{F}(s,t)\delta\big(\boldsymbol{x} - \boldsymbol{X}^e(s)\big)ds \ ; \boldsymbol{x} \in \boldsymbol{\Omega_s} \tag{I-43}$$

$$\nabla^2\Phi = -\frac{\sum\rho}{\epsilon}; \boldsymbol{x} \in \boldsymbol{\Omega_s} \cup \boldsymbol{\Omega_f} \tag{I-44}$$

The last term in the right-hand side of Eq. I-45 is the virtual boundary source term, which is added to satisfy the boundary condition,

$$\frac{\partial n_e}{\partial \boldsymbol{n}} = \boldsymbol{n} \cdot \big(a_e b_e n_e \nabla\Phi \ - \gamma b_p n_p \nabla\Phi\big) \tag{I-45}$$

$$\boldsymbol{F}(s,t) = \alpha \int_0^t \partial_n n_e(s,\tau)d\tau + \beta\partial_n n_e(s,t) \tag{I-46}$$

The accuracy of the boundary condition implementation is dependent on the grid resolution across the void interface. In the current framework, the interface is adequately resolved, due to the AMR methodology. This approach offers a practical way of resolving the charge distribution within voids of arbitrary shapes, an example of which is shown in Fig. 3-19. The void topology is adopted from the defect propagation simulation results and corresponds to the initial pre-treeing aging stage of the process.

As expected, the charge migration appears to be predominantly in the direction of applied electric field and to be less affected by features that are orthogonal to the direction of the external field. There also appears to be local enhancement of charge generation at the interfacial crevices.

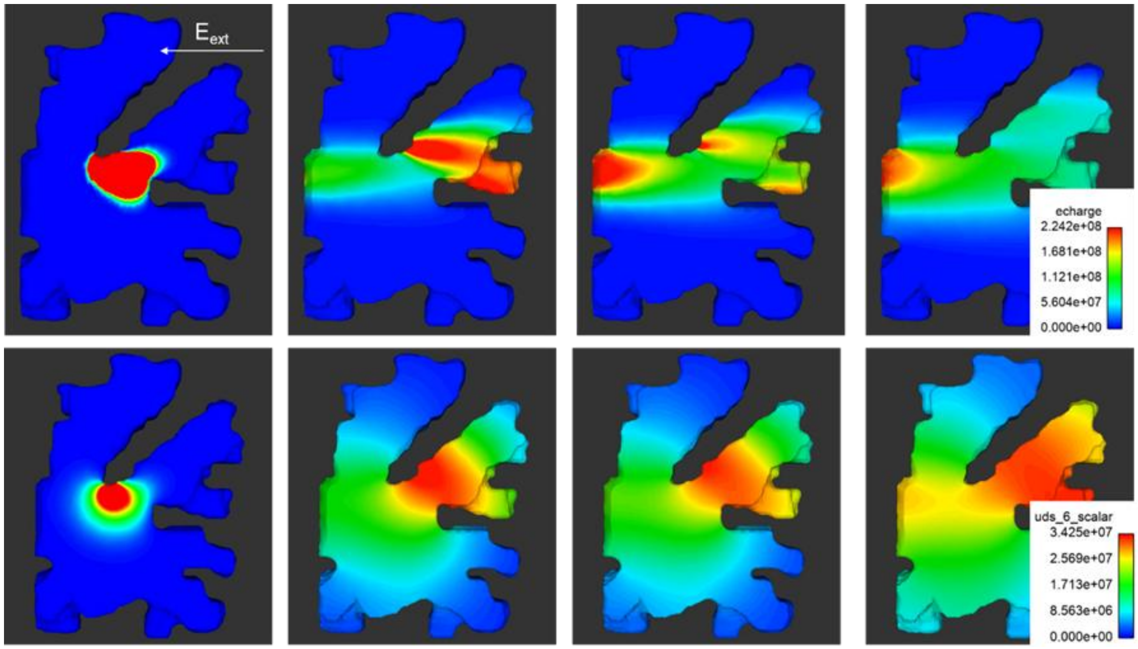

Figure 3-19. *Discharge dependent variables, top: electron number density, bottom: photoionization source term. Temporal evolution from left to right: 1 ns, 5 ns ,10 ns, 20 ns. Void spatial extend is ~100 μm*

3.7. LAPSSE for Defect Growth and Partial Discharge

So far, the focus has been on capturing key physical mechanisms at their appropriate spatial and temporal scales. For instance, the crack propagation approach assumed a specific charge distribution to calculate the field distortion due to the discontinuity of the crack, and the resultant electric stress. However, the charge distribution is driven by the relevant physical mechanisms in the voids and defects. A challenge arises because the characteristic time scale of a partial discharge (10-6 s) is vastly different from the timescale associated with tree propagation (100 s) making the simultaneous simulation of the two mechanisms computationally challenging.

This challenge is met using a method referred to as LAPSSE (Largely Asynchronous Simulation of Simultaneous Events). This approach creates a framework to integrate physical mechanisms with vastly different characteristic timescales. This methodology was originally developed for simulation of supercooled crystallization of water together with droplet condensation and droplet dynamics and is presented here for simulating the impact of bulk charge transport and Partial Discharge on electric tree propagation. The LAPSSE integration is a critical step towards full integration of the physics-based model of insulator degradation which allows integration of other physical mechanisms as they are developed.

The phase-field description of degradation and the partial discharge model allow simulation of electric-field induced defect propagation and charge transport within the voids. The two physical mechanisms, while coupled, develop at vastly different timescales (~101-102 s vs. 10-6-10-5 s, respectively) making the brute-force simulation of the two together computationally intractable. The projected computational cost is demonstrated in Fig. 3-20, if brute-force simulation of the two-events (first series of bars: NPARTIAL DISCHARGE = 106) are used, versus if only a selective number of partial discharge events are simulated at a given degradation (PF) timescale (all other bars).

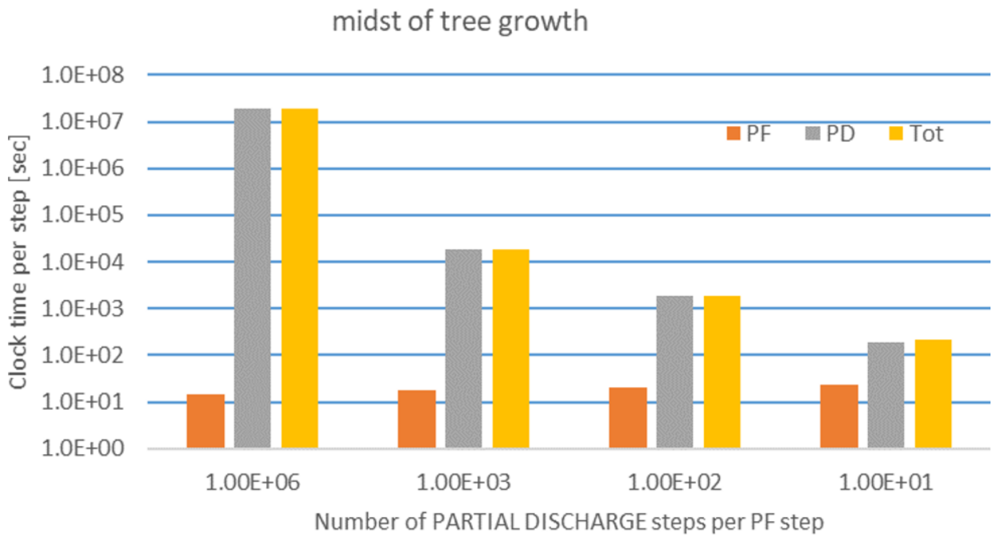

Figure 3-20. *Computational cost of not addressing timescale issue*

In LAPSSE framework, the "slow event" (here the propagation of the defect) is solved at fully resolved temporal resolution, while the "fast event" is solved discretely and the solution between the discrete events are approximated to create a continuous solution over the slower timescale. The approximation is called "inter-LAPSSE". The schematic illustration of the inter-LAPSSE that integrates defect propagation and partial discharge mechanisms is shown in Fig 3-21.

3.7.1. Inter-LAPSSE Establish Initially Sampled Solutions

A one-time solution for charge distribution at a given partial discharge timescale is generated using the transport equations, namely,

$$for\ 1 < i < N_{PD}: \frac{\partial \rho_{\pm}}{\partial t} + (\vec{u}_e \cdot \nabla \rho) = \sum S_\rho \tag{I-47}$$

$\rho_{\pm i}(\vec{x}, t)$ is identical for all instances.

3.7.2. Sample Initial Charge Distribution for Partial Discharge Events

Next, discrete "initial" solutions are sampled from the partial discharge cycle solution generated in the previous step,

$$for\ i\ \in\ < 1, N_{PD} >: \quad \rho_{\pm}(\vec{x}, 0) = \hat{\rho}_{\pm}(\vec{x}, \hat{t} \in \Delta t_0) \tag{I-48}$$

This establishes a non-trivial charge distribution within the voids which is provided from a partial discharge solution through random sampling. This approach is motivated by the fact that in operation partial discharge events are likely to occur while there is residual charge in the cavity from previous partial discharges.

3.7.3. Discretely Sample Partial Discharge Solutions

The initial solution sampled in step B is used to calculate a partial-discharge-induced charge distribution for the corresponding discrete events. The charge transport equations are solved similar to the past with the exception of the boundary and initial conditions.

$$for\ i\ \in\ <1, N_{PD}>:\ \frac{\partial \rho_{\pm}}{\partial t} + \left(\vec{u}_{\rho} \cdot \nabla \rho\right) = \sum \rho_{\pm}\,; \tag{I-49}$$

$$\rho_{\pm}(t=0) = \hat{\rho}_{\pm}(\vec{x}) \tag{I-50}$$

$$\nabla^2 \Phi_{PD} = \frac{\sum \rho_{\pm}}{\epsilon};\ \ 0 < t < \Delta t_{PD} \tag{I-51}$$

3.7.4. Inter-Event Projection

The approach is to approximate charge distribution between subsequent discrete events (for which full solution is obtained in Step C) without solving the partial discharge systems. We assume at any intermediate time, $\mathrm{t} = \mathrm{t}_{\mathrm{i}*};\ \mathrm{t}_{\mathrm{i}} < \mathrm{t}_{\mathrm{i}*} < \mathrm{t}_{\mathrm{i}+1}$:

$$\Phi_{i*}(\vec{x}) = \frac{\Phi_{i}(\vec{x}) + \Phi_{i+1}(\vec{x})}{2} \tag{I-52}$$

which implies that the electric potential varies linearly between subsequent partial discharge events.

This leads to the following equation for $\rho_{\pm}$:

$$\rho_{\pm}(\vec{x}) = \rho_{\pm}(\vec{x}) exp\left(-\frac{t - t_i}{t_{i+1} - t_i}\right) \tag{I-53}$$

which implies an exponential decay of charge distribution from one event to another. Substituting this expression into the charge transport equation, the total charge distribution then takes the following form:

For $t_i < t < t_{i+1}$,

$$\rho_{\pm}(\vec{x}, t) = \hat{\rho}_{\pm i} exp\left(\frac{b_{\pm}}{2D_{\pm}} \nabla \widehat{\Phi}_{i} \cdot (x - x_0)\right) exp\left(\frac{-t - t_i}{t_{i+1} - t_i}\right) \tag{I-54}$$

The computational approach is summarized in Fig. 3-21.

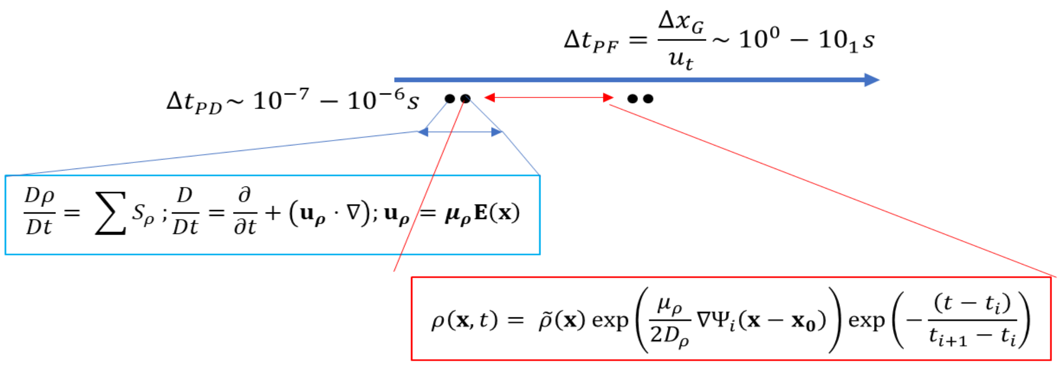

Figure 3-21. *Schematic illustration of inter-LAPSSE for the integration of Partial Discharge and PF solvers*

This gives rise to a continuous charge distribution over the full timescale without having to solve for the set of partial discharges at all partial discharge times. The partial discharge model renders the charge distribution within the voids and tree channels and not within the insulator's bulk. Consequently, this specific inter-LAPSSE formulation is relevant only to coupling between partial discharge and degradation models in the voids and cracks.

The computational (free) parameter, of course, is the number of sampled partial discharges. NPARTIAL DISCHARGE, to be simulated at any time-step. It can be shown that a computational convergence can be achieved beyond a certain number of simulated partial discharges. The evolution of electric tree structure with number of partial discharges (NPARTIAL DISCHARGE) at similar physical times in a 2D simulation is shown in Fig. 3-22. At low NPARTIAL DISCHARGE (which implies very discrete partial discharge events), the model grossly underpredicts the electric stress as the result of partial discharges in the tree channels. The tree structures at NPARTIAL DISCHARGE = 128 and 256 seem to indicate numerical convergence at this sampling rate. Note that identical solutions for two different NPARTIAL DISCHARGE are not expected due to the statistical nature of this approach.

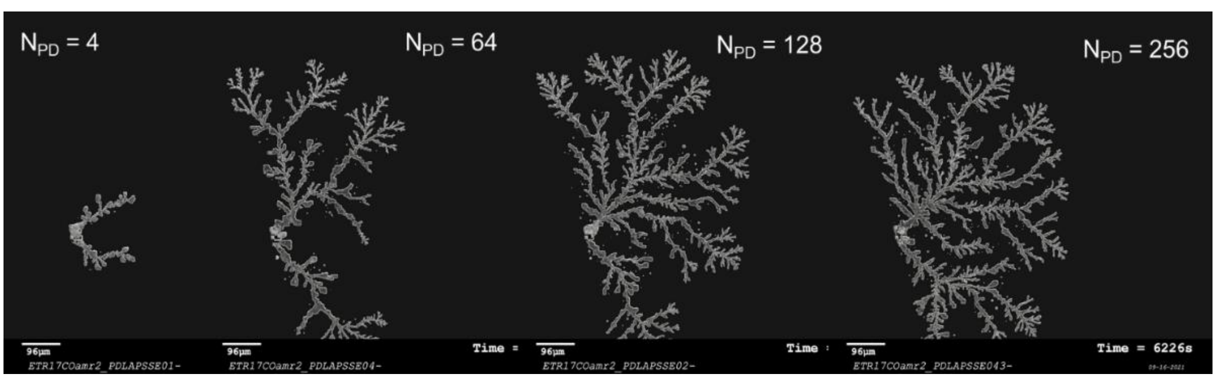

Figure 3-22. *Variation of electric tree structure at similar physical time with number of simulated partial discharge events, $N_{PARTIAL\ DISCHARGE}$*

The variation of electric free energy as well as the partial-discharge-induced charge distribution for simulations with different NPARTIAL DISCHARGE is shown in Fig. 3-23. Though quantitatively different, the free energy curve and the charge distribution become effectively independent of number of sampled events beyond NPARTIAL DISCHARGE = 128. The computational overhead associated with LAPSSE framework is plotted in Fig. 3-24, which shows the increasing computational cost as the number of partial discharge events increase.

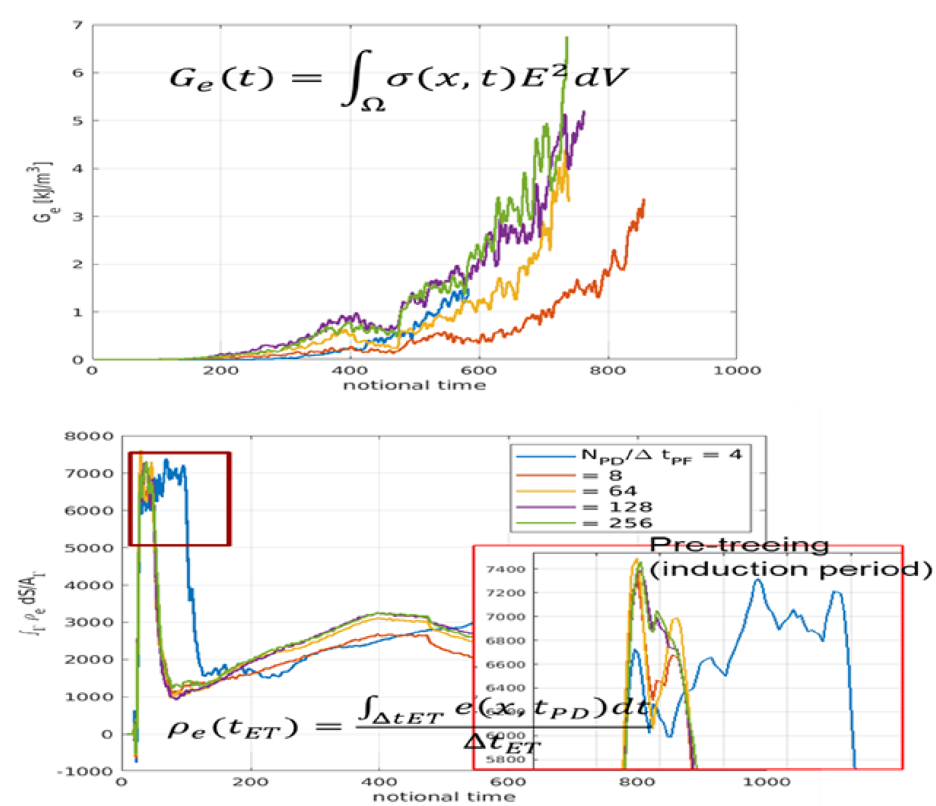

Figure 3-23. *Variation of free energy associated with electric stress (top) and charge distribution in the void as the result of Partial Discharge with number of simulated Partial Discharge events, N*$_{PARTIAL\ DISCHARGE}$ *(bottom)*

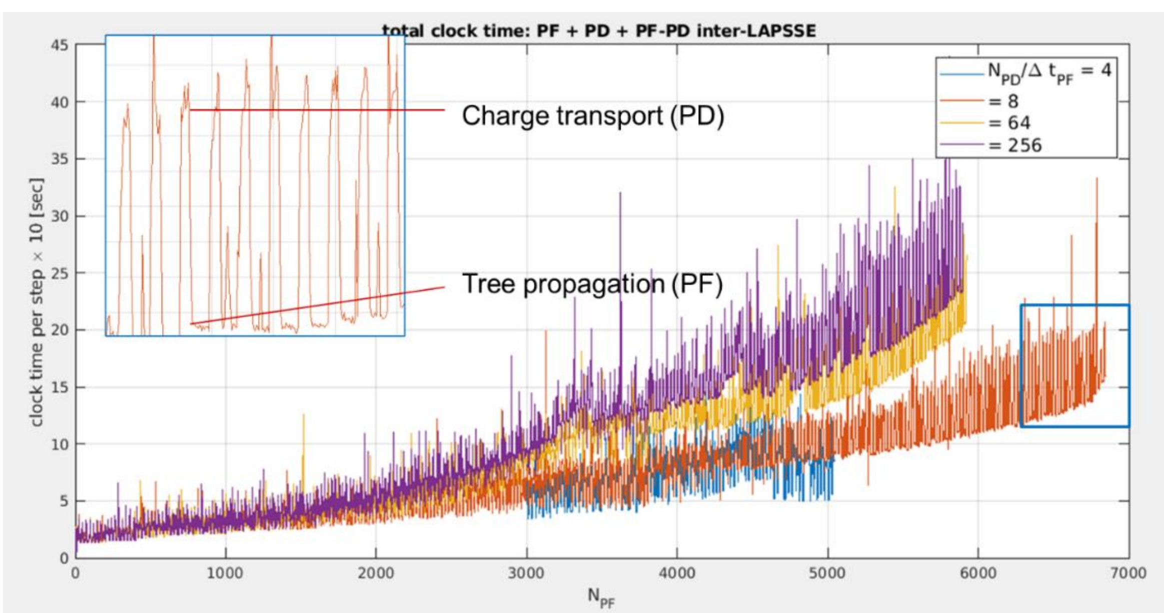

Figure 3-24. *Computational breakdown of different physical mechanism over physical time (N*$_{PF}$*) and its variation with number of simulated partial discharges, N*$_{PARTIAL\ DISCHARGE}$

This integrated framework can be used to study the effect of various operating parameters. For example, in Fig- 3-25, it shows how the gas pressure (i.e., operating ambient pressure) influences charge dynamics and hence the resultant electric stress generated in the bulk.

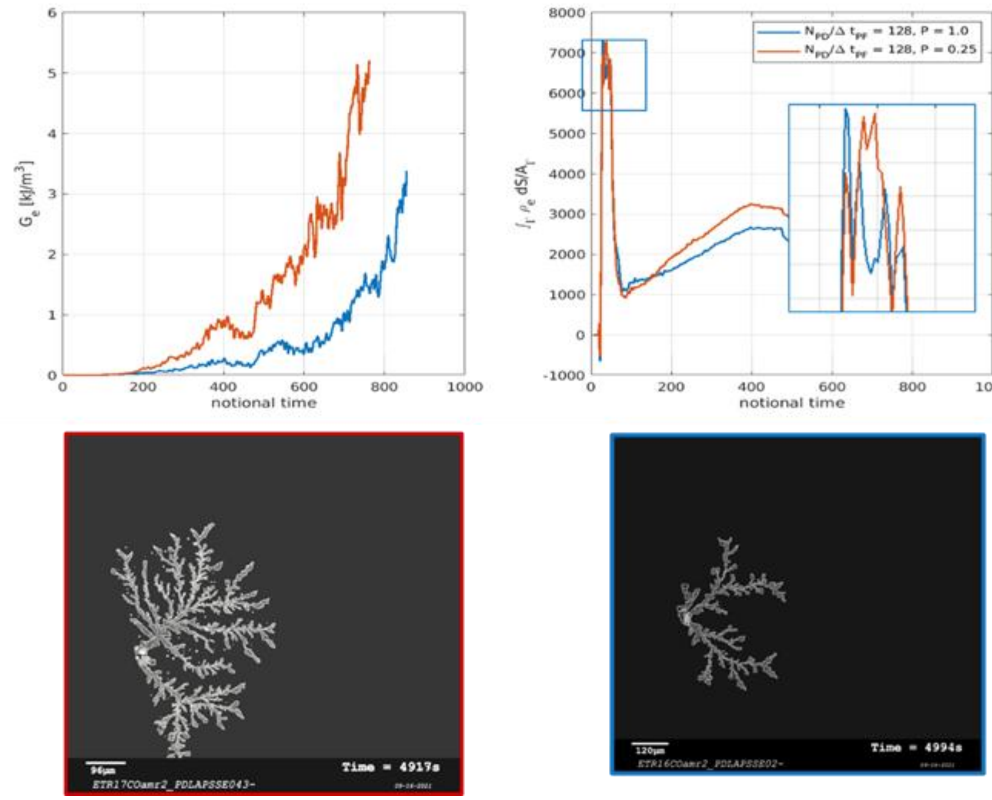

Figure 3-25. *Example showing the model's ability to predict effect of operation parameters (pressure) on life*

3.8. Immersed Boundary Method for Arbitrary Topologies

The previous section describes the inter-LAPSSE for integration of partial discharge and phase field events. Here, the approach to integrate the electromechanical aging phenomena (which is captured through Monte Carlo simulation of charge transport in the bulk) is discussed. The primary challenge is that the characteristic time scale of charge transport resides somewhere between characteristic time of a partial discharge and the one of crack propagation.

A key question to address is how to calculate electric field, $E(\vec{x})$, at the Monte Carlo time steps (t^m) given that information is available at the two subsequent crack-growth time steps, t^n and t^{n+1}.

The solution to the electric field is available at t^n and $^{tn+1}$ through,

$$\vec{E} = \vec{E}_{ext}(x) + \vec{E}_T(\vec{x}) = -\nabla\Psi_{ext} - \nabla\Psi_T;\ \vec{x} \in \Omega \text{ and } \Psi_T = \Psi_0 \quad \text{(I-55)}$$

$$(f'(\Phi)\nabla\Phi)\cdot\nabla\Psi_0 + f(\Phi)\nabla^2\Psi_0 = (\nabla f \cdot E_{ext}) - \frac{\rho(\mathbf{x})}{\epsilon_0} \quad \text{(I-56)}$$

Only the zero[th] order term is kept for the sake of simplicity. The charge distribution, $\rho(\mathbf{x})$, is obtained through:

$$t_i < t < t_{i+1}, \rho_{\pm}(\vec{x},t) = \rho_{\pm i} exp\left(\frac{b_{\pm}}{2D_{\pm}}\nabla\Phi_i \cdot (\vec{x} - x_0)\right) exp\left(\frac{-t-t_i}{t_{i+1}-t_i}\right) \quad \text{(I-57)}$$

The crack interface location, tracked through Φ, at intermediate times, t^m is proposed to be tracked to an analytical approximation of the phase field equation:

$$\Phi(t^m) \simeq \left(\Phi(t^n) - \Phi(t^{n+1})\right) \exp\left(-\frac{t^m - t^n}{\Delta t_{PF}}\right) + \Phi(t^{n+1}) \quad \text{(I-58)}$$

Substituting this expression into the above yields:

$$f'\left(\Phi^*(t^m)\right)\nabla\Phi^*(t^m)\cdot\nabla\Psi_0^m + f\left(\Phi^*(t^m)\right)\nabla^2\Psi_0^m = \left(\nabla f\left(\Phi^*(t^m)\right)\cdot E_{ext}\right) + \frac{\rho^m}{\epsilon T} \quad \text{(I-59)}$$

Although this equation technically must be solved at every MC step (t^m), in practice, the solution to this equation is computed at statically sampled Monte Carlo steps and linear interpolation is performed to get the solution at other steps. Going back to the Monte Carlo formulation for bulk charge transport:

$$\vec{x}_i(t^m) = \vec{E}^m(\vec{x})\sqrt{2D\Delta t_{mc}} + x_i(t^{m-1}) \quad \text{(I-60)}$$

$$\vec{E}^m(\vec{x}) = \nabla\Psi_T^m(\vec{x}) \quad \text{(I-61)}$$

The tree growth in the presence of bulk charge transport (left) and an instantaneous snapshot of the partial-discharge-induced charge distribution in the tree channels as well as the induced electric field due to charge migration in the bulk are shown in Fig 3-26.

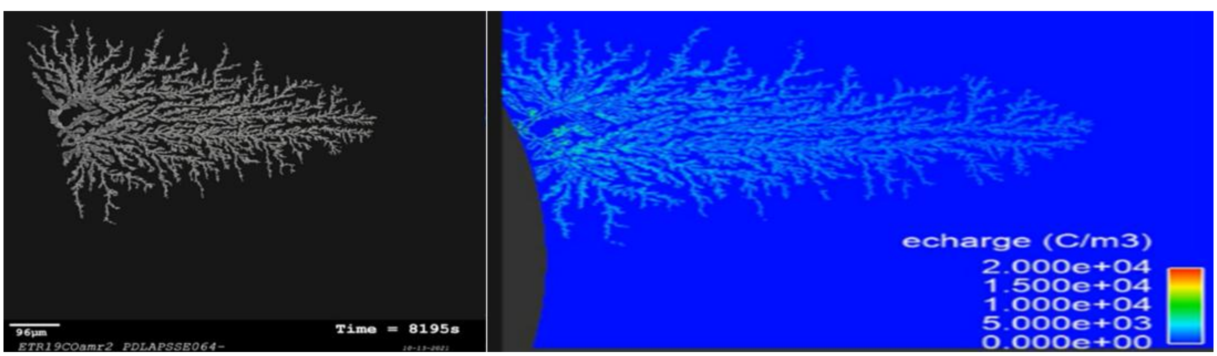

Figure 3-26. *Tree growth example as calculation*

Compared to the non-coupled calculations the electric degradation is significantly more aligned with the direction of the electric field. The bulk-charge-transport-induced field (image on the far left) has scattered characteristics due to the scattered nature of the charge distribution in the bulk. The instantaneous image, therefore, may not reflect the actual impact.

The significance of bulk charge transport on tree propagation is shown in Fig. 3-27. While the structure of the tree appears largely unaffected by the charge dynamics in the bulk (with a disclaimer that this is a

2D demonstration), the propagation seems to be significantly accelerated due to the additional electric stress induced by charge transport in the bulk.

The integrated life model is based on tracking free energy. Thus, the ultimate implication of various degradation and aging mechanisms on a sample's free energy for a hypothetical system is presented in Fig. 3-27. The change in the slope of energy increase (negative slope indicates increase in electric stress) at the onset of tree initiation and increasing contribution of electric stress due to bulk charge transport are some of the observations from this plot. The subsequent reduction of electric stress associated with electric tree (red line) is a numerical artifact which is caused by re-coarsening of the background grid at "old" tree channels.

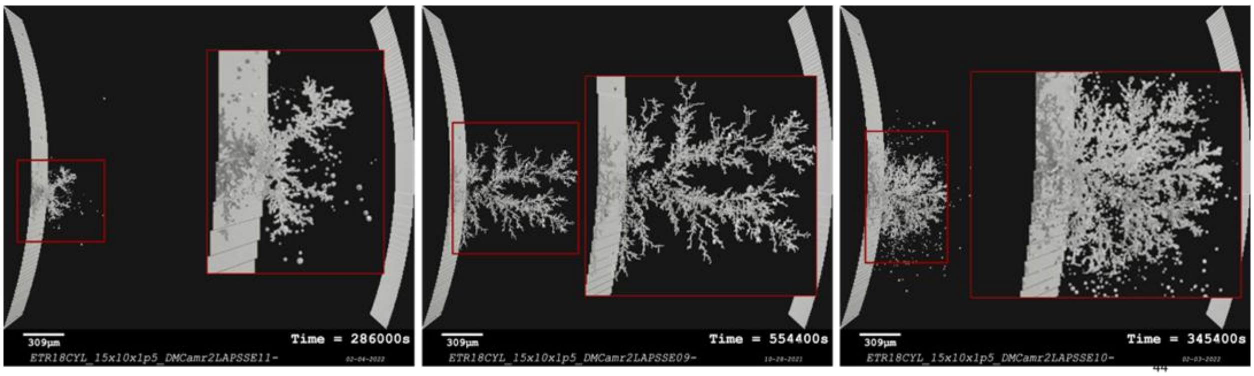

Figure 3-27. *Tree Propagation with and without bulk charge transport Included. Pressure and Temperature for each subset*

3.9. Immersed Boundary Method for Arbitrary Topologies

The goal of this model is to develop a tool to estimate the life of the polymer when it is subject to electric degradation. To that effect, a free energy approach, adopted from [69] is proposed. In this approach, the total free energy of the system is calculated based on contribution of different mechanisms over time. It is argued that the propagation of the crack is "unfavorable" when the free energy is positive and therefore is largely driven by the electric (or other) sources of stress. Once the free energy becomes negative, the propagation of the crack is favorable which results in its runaway, giving rise to the end of life.

The life model has three major pieces. First, it uses the Miner simplification to transform the transient temperature, pressure and voltage profiles that the insultation will be exposed to in the actual aircraft installation, into a periodic set of quasi-steady profiles that will be more easily used by the aging and degeneration models. For example, a cable is exposed to a time variant temperature over the time length of a 2-hour typical mission, which contains 15 minutes at the lowest temperate (at various times throughout the mission) and 30 minutes at the higher temperature (again at various times throughout the mission). The Miner simplification algorithm would calculate the average temperature for the remaining 75 minutes and then apply a step temperature versus time profile, from minute 0 to 15 at the lowest temperature, 15 to 90 at the mid-level temperature, and 90 to 120 at the highest temperature.

The second major piece calculates the total bulk stress based on the strain energy in the bulk, induced mechanical stress, electric stress and crack geometry. The degradation model feeds field and tree information into this "Total Bulk Stress" block of the Life Model.

$$G(t) = G_c(t) - f_M d - f_e(t)\delta(t) + 2\gamma a(t) \qquad \text{(I-62)}$$

$$G_c = \frac{K_{IC}^2(t)}{E'(t)}; E'(t) = \frac{E(t)}{1-\nu^2} \quad \text{(I-63)}$$

$$F_E(t) = \sigma(t)E(t)^2, \quad \text{(I-64)}$$

$$V_{tr}(t) = \int_\Omega \Phi(t)dV \quad \text{(I-65)}$$

$$A_{tr}(t) = \int_\Omega \nabla\Phi(t)dV \quad \text{(I-66)}$$

The first term $G_c(t)$ accounts for electric strain in the bulk (blue line in Fig. 3-28) and the resulting decrease in material strength over time, represented by a decrease in the Gibbs free energy. This term is calculated from field information and material property information, which come from the degradation model (red line in Fig. 3-28). The second term $f_M(t)$ accounts for mechanical stress. The third term $f(e)\delta(t)$ is the Maxwell electric stress caused by the electric trees over time, predicted by the degeneration model (orange line in Fig. 3-28), while the fourth term $2\gamma\alpha(t)$ captures the stress relief afforded by the cracks in the form of surface energy (yellow line in Fig. 3-28). This data all comes from the degeneration model. The net Gibbs free energy is expressed by the Gibbs free energy formula which aggregates all these terms (black line in Fig. 3-28).

Finally, the Health Assessment Model uses empirical data to determine the Gibbs free energy at which useful life has ended. In Fig. 3-28, a forming tree represents the output of the degeneration model (the Life Model). The red arrow shows a potential end of life when net Gibbs free energy reaches "0".

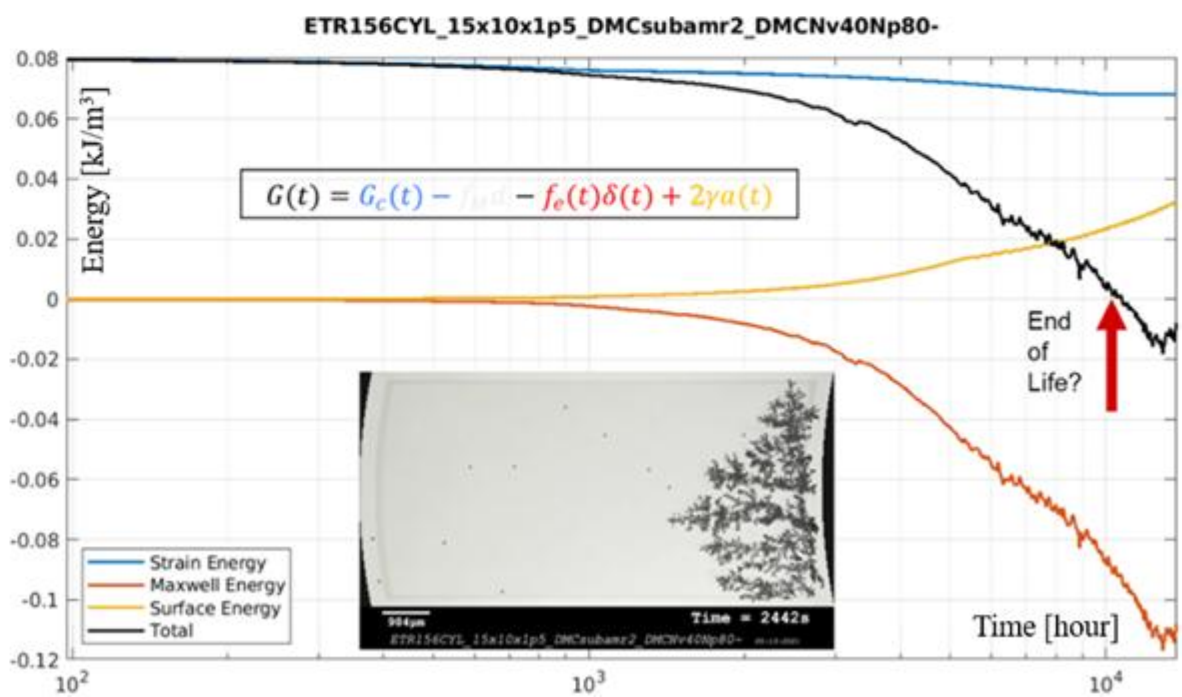

Figure 3-28. *Life model: an example output*

4. EXPERIMENTAL INVESTIGATIONS

The theoretical approach focused on the development of a life model based on the best available information about expected dominant failure mechanisms. However, the evidence to support this model and make reliable predictions is limited by the lack of experimental data. The lack of data arises because the application provides an unprecedented environment for parameters that have been shown to influence aging.

One difficulty is that the targeted cable material in this project, PFA, is not a material used traditionally in the electric power grid. A new material is beneficial in this application to provide lighter weight cables at higher operating temperatures than are widely encountered in the grid. These are enabling properties for aircraft electrification.

The 2nd difficulty is the operational environment, specifically, the temperature, electrical environment, and the levels of shock and vibration, which are very different from those in the legacy grid. Consequently, while the physics of insulation material failure is expected to be similar, the failure rate is likely to be quite different. Experimental data are needed to populate the model with reasonable failure rates.

The analysis in this project and decades of cable studies have indicated a general progression of cable life, which can be expressed by a power law equation as below:

$$L = A \cdot E^{-n} \qquad \text{(II-1)}$$

where, L is the cable life, E is the applied electric field, and A and n are material constants, with n called the voltage endurance coefficient.

When the eq. (II-1) is shown on a log-log plot, it produces the green line as shown in Fig. 4-1. Thus, the physics-based framework presented in Section 3 aims to predict the rate of material degradation through phase-2 and phase-3, assuming some empirical knowledge of phase-1 aging (which is predominantly thermomechanical and process-centric). However, insulation aging is a complex process because it depends on the use environment. In transportation electrification, the need to minimize size and weight combined within a complex electrical, thermal, and mechanical environment may lead to a different prediction, which can be represented by the purple line in Fig. 4-1.

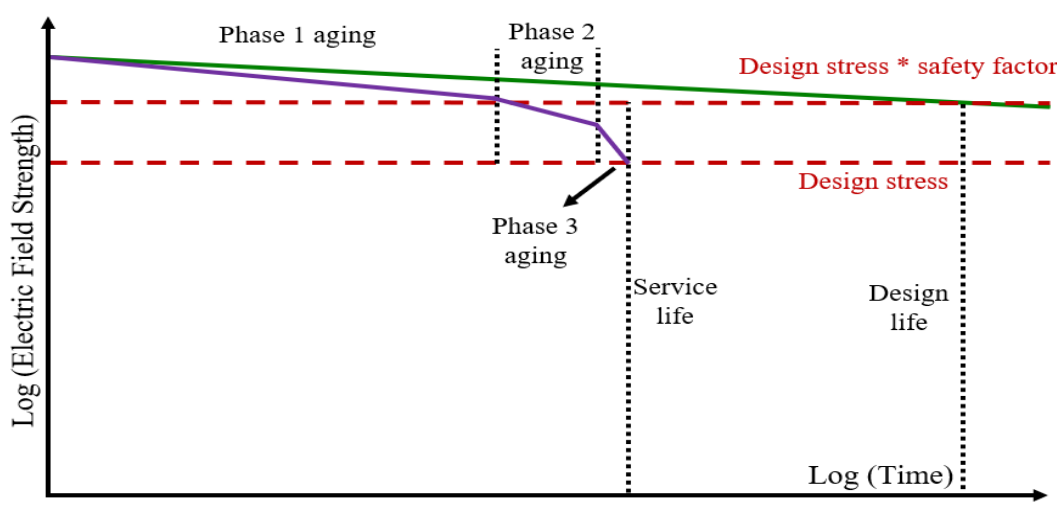

Figure 4-1. *Generic cable aging curve*

Keeping to the purple line in Fig. 4-1, Phase 1 aging is presumed to be dominated by the growth of nanometer-sized voids to micrometer-sized voids, primarily due to thermal-mechanical stress. The electric effects are expected to be of lower significance in this phase because the electric field in the void is small. Such small E-field stress cannot accelerate electrons to a sufficient energy level to collide and, therefore, ionize the neutral gas atoms or molecules in the void. After a void grows to a size of a few microns, there can be sufficient energy to produce ionization leading to an increase in pressure and temperature.

When cable life prediction moves to Phases 2 and 3, the electric effects dominate. This transition in the physics of failure led to the researchers to consider investigating two failure paths. The first path was to accelerate the thermal-mechanical void growth, while the other was to accelerate the electrically driven void growth.

4.1. Thermal-Mechanical Aging

The plan for the testing of the power cable, PFA (perfluoro alkoxy) cable (AWG 10), matured through discussions with experts at RTX Technology Research Center (RTRC), Habia, the University of Texas at Austin and the University of Connecticut. The PFA material is appealing for the aircraft electrification application because it has superior thermal and electrical performance that suggests small cables can function well in the environment. In addition, the material is known to be resistant to stress cracking, raising the possibility of long life. However, since PFA is a relatively new material for cable insulation, there is not extensive life data available in any thermal, mechanical, and electrical environment, let alone for the environment found in electrified aircraft.

To investigate the Phase 1 thermal-mechanical dominated cable aging, we generated a fixture and thermal cycling to simulate the cable operation condition. Showing in Figure 4-2, we bend the cables around 1-inch diameter and 2-inch diameter aluminum tubes and fastened them on to the fixture. Thermal aging of the bent (mechanical stressed) along with un-bent cables is executed in a thermal cycling chamber (Fig. 4-3). This yields a uniform temperature in the dielectric rather than the nonuniform distribution produced when the cable is heated via the center conductor. This was done to determine if the higher volume of high temperature material would accelerate thermal aging. The thermal cycle testing profile can be found in Fig. 4-4.

The aging assessment is done via partial discharge measurements. The goal was to determine how many cycles are needed to stimulate the growth of a void to a size that would support partial discharge. Moreover, all the cable dielectric is subjected to the applied electric field at the same time.

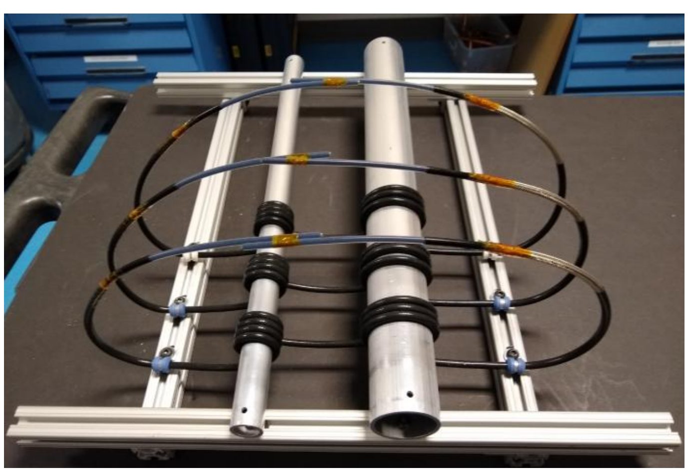

Figure 4-2. *Three cables bent and fixed for thermal aging with some mechanical stress*

Figure 4-3. *Thermal cycling chamber at RTX Technology Research Center (RTRC)*

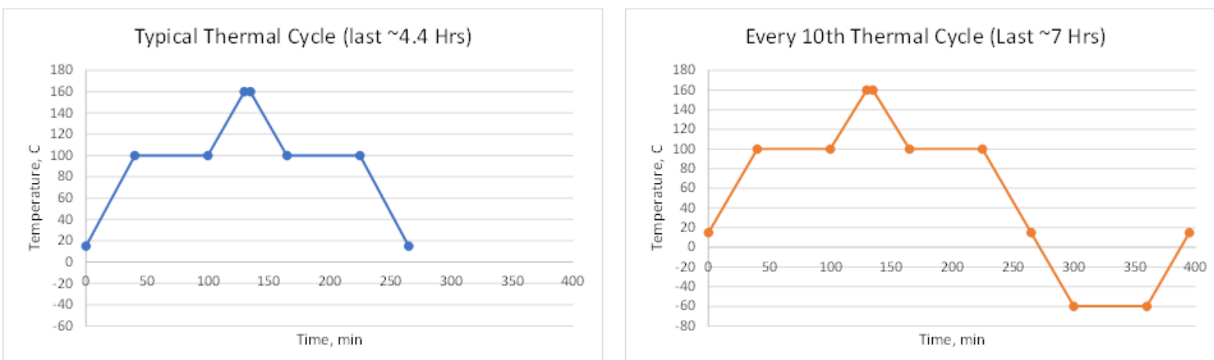

Figure 4-4. *Thermal aging testing profile, nine typical cycles (left chart) and every 10th cycle with -60 °C soaking (right chart)*

During this project, six PFA cables constituted the test cohort. They were aged and tested for partial discharge activity to identify the growth of voids due to thermal-mechanical stresses. The conditions of the six cables are listed below in Table.4-1, while the cable inner structure and the dimensions of each layer are shown in Fig. 4-5.

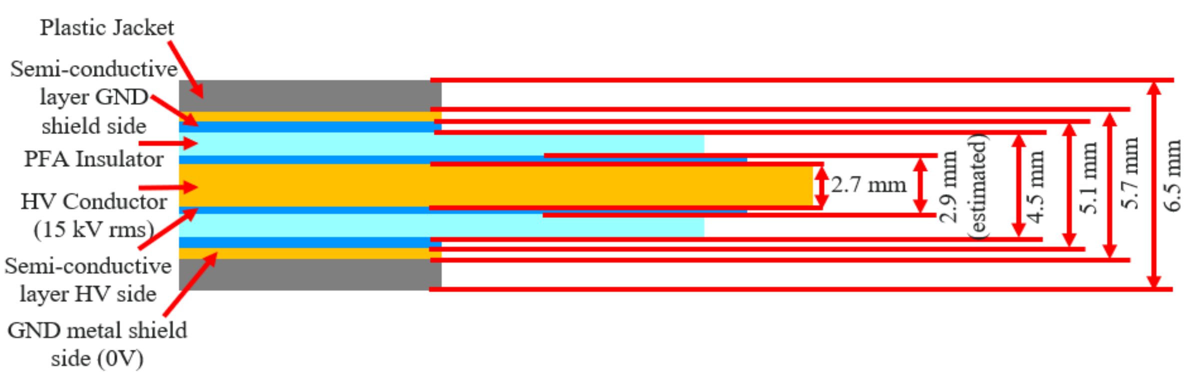

Figure 4-5. *The cable inner structure and measured dimensions for each layer*

Table. 4-1. *Conditions for the six PFA coaxial cables received from RTX Technology Research Center (RTRC)*

ID	Description	Length (inch)	Bending	Aging Cycle
1	PFA coaxial cable with semiconductive and shielding layer	80	Yes	800
2		80	Yes	0
3		80	No	0
4		80	No	1950
5		80	Yes	1950
6		80	Yes	1950

Reliability in partial discharge testing requires detailed electric-field analysis, guard ring design, and proper test setup construction. This is required to achieve confidence that any measured discharges are due to voids in the cable and not due to electric field enhancements in other parts of the test apparatus. Guard rings were designed and built to shield the E-field and eliminate the possible surface discharges along the cable ends. The hole diameter for the guard ring was 5 mm, and the edge-to-edge diameter of the ring was 65 mm, as shown in Fig. 4-6.

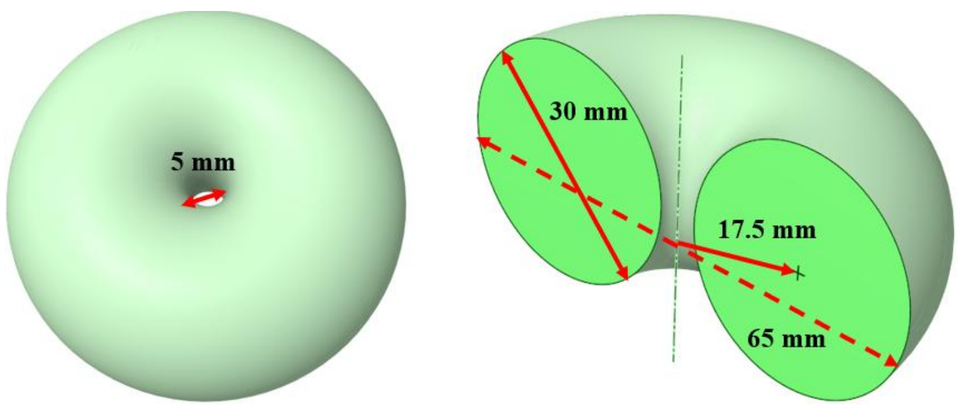

Figure 4-6. *The guard ring dimensions*

The key results of the electric field analysis can be found in Fig. 4-7. Two major conclusions followed. First, the E-field intensity along the metal-to-air and insulator-to-air interfaces is well controlled. Surface discharges should be eliminated under this structure with excitations up to 15 kV rms. Second, the guard ring design has a shielding effect of ~5 cm distance from its center. This should be sufficient to cover the cable section from the oil tank to the rings.

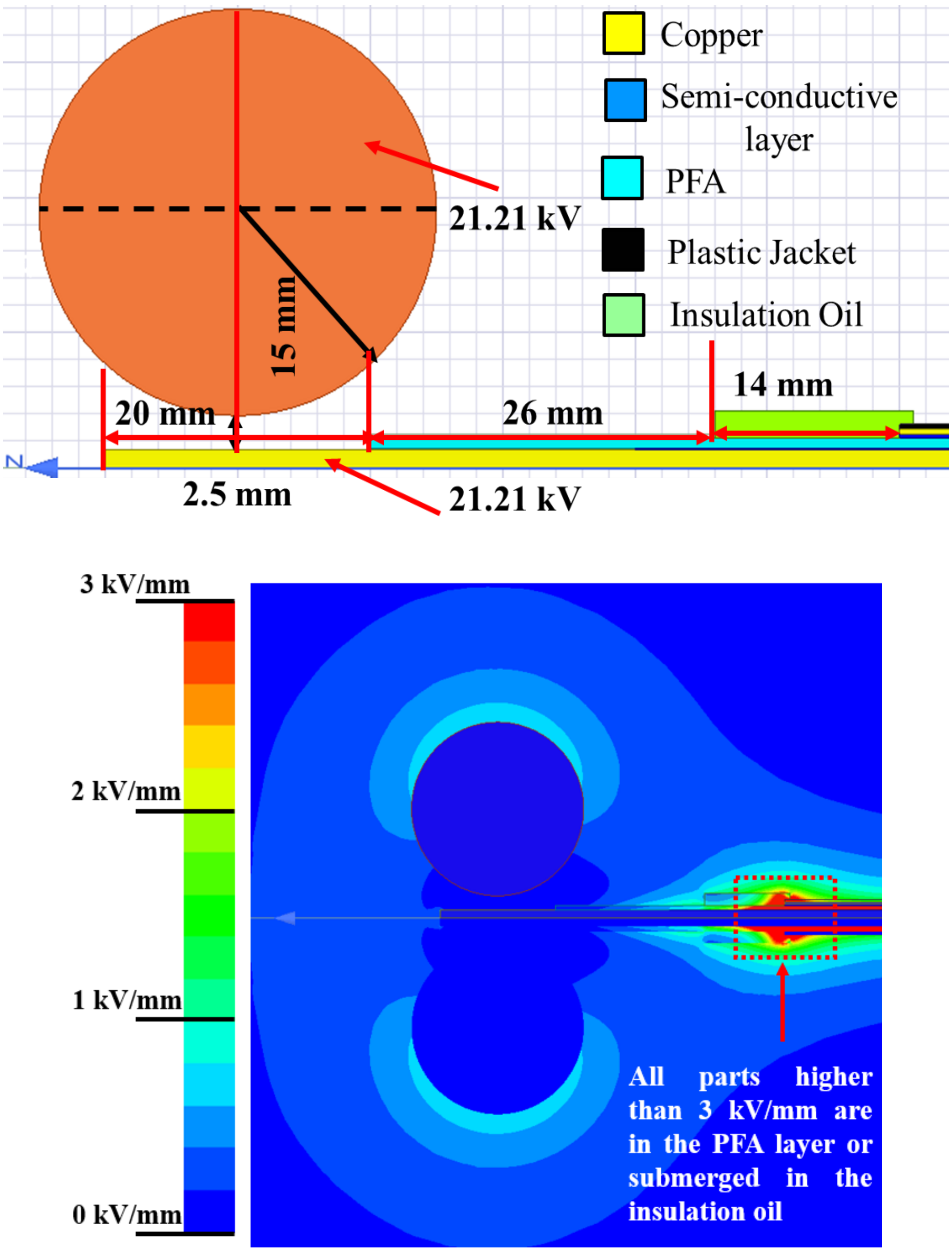

Figure 4-7. *The parameters applied in the simulations and E-field analysis results*

The connections for the PFA cable on the metal frame during the test with guard rings and the important details can be found in Fig. 4-8.

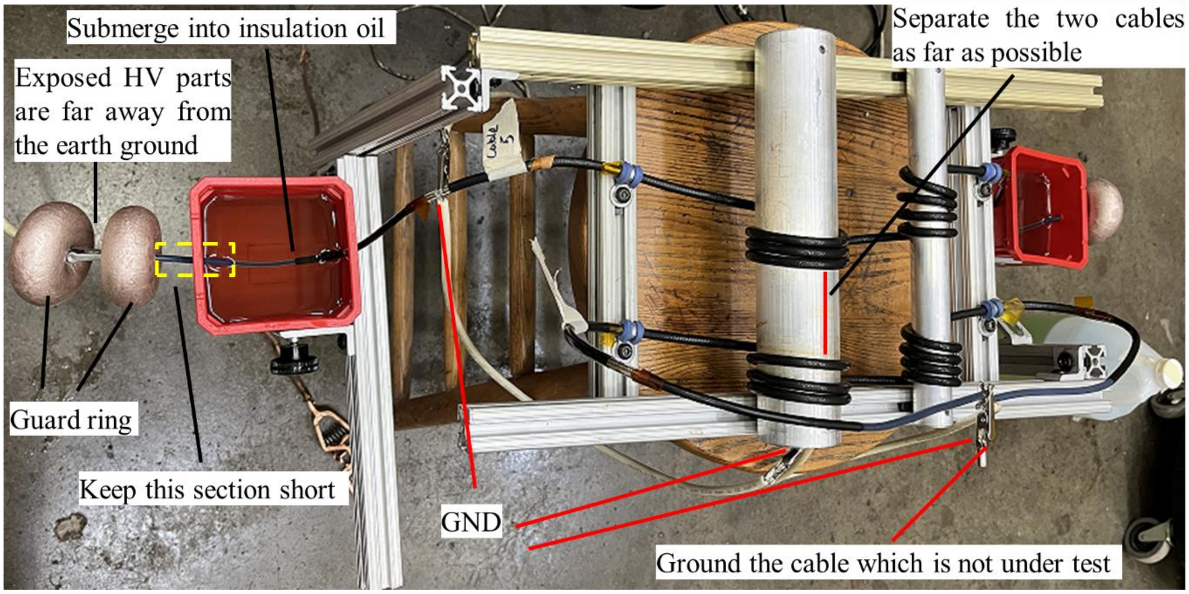

Figure 4-8. *The connections for the PFA cable on the metal frame during the Partial Discharge test with the designed guard rings and important details marked*

The diagram of the PD test setup can be found in Fig. 4-9. An oscilloscope can capture the PD data and a high frequency current transformer (HFCT) is applied as the partial discharge sensor. A commercial capacitor with a built-in voltage divider scales excitation voltage for measurement, which also provides phase information of the excitation. This device is designed for 24 kV rms AC and frequency range from 30 to 300 Hz. Thus, the entire setup, which includes the high voltage filter and voltage measurement device, is discharge free at least up to 20 kV rms.

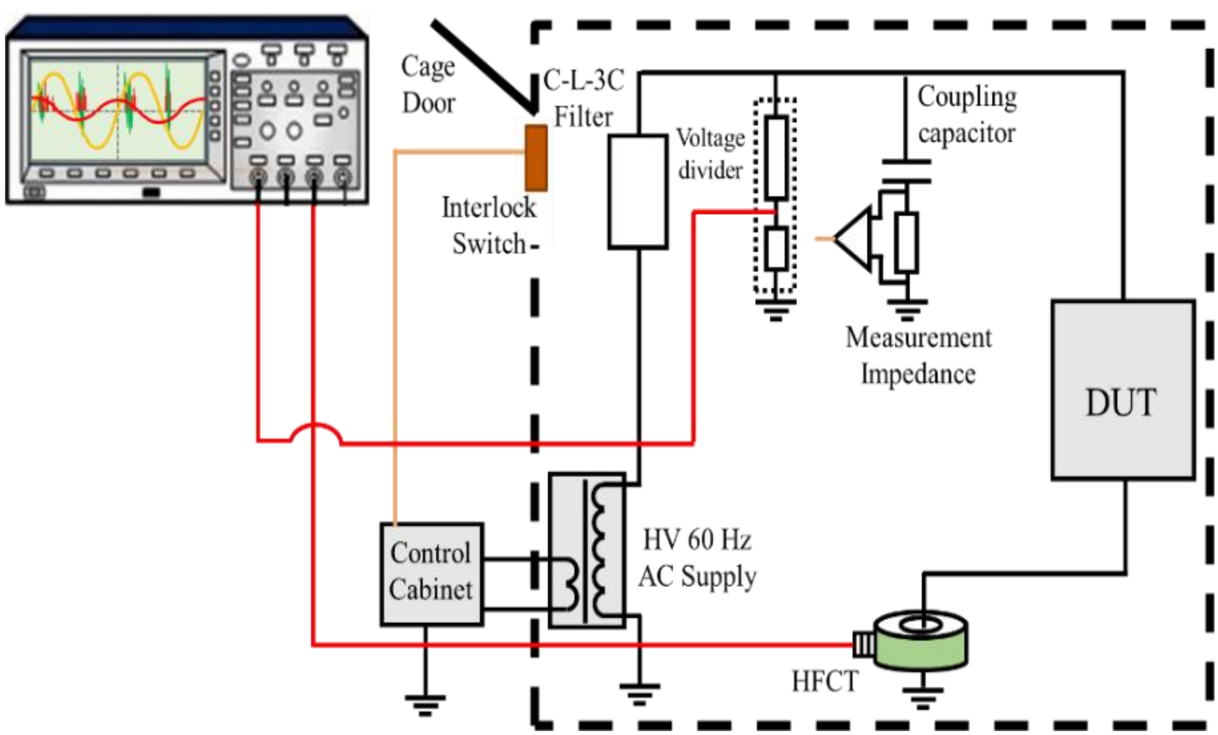

Figure 4-9. *The schematic of the entire Partial Discharge measurement setup*

Before measuring partial discharges in a cable, a standard discharge calibrator is used to inject 100 pC into the system and to check the system response. As shown in Fig. 4-10, the captured pulse magnitude is about 30 mV under the scope channel bandwidth up to 20 MHz.

The high voltage power produces a background noise of about 1 mV. Since the charge level is proportional to the pulse magnitude and usually a pulse can be identified as a partial discharge event if its magnitude is more than two times of the background noise, the sensitivity of the entire setup is around 7 pC. Without high voltage on, the background noise of the lab is about 1.3 mV (~4 pC). Therefore, the system's maximum sensitivity is ~8 pC.

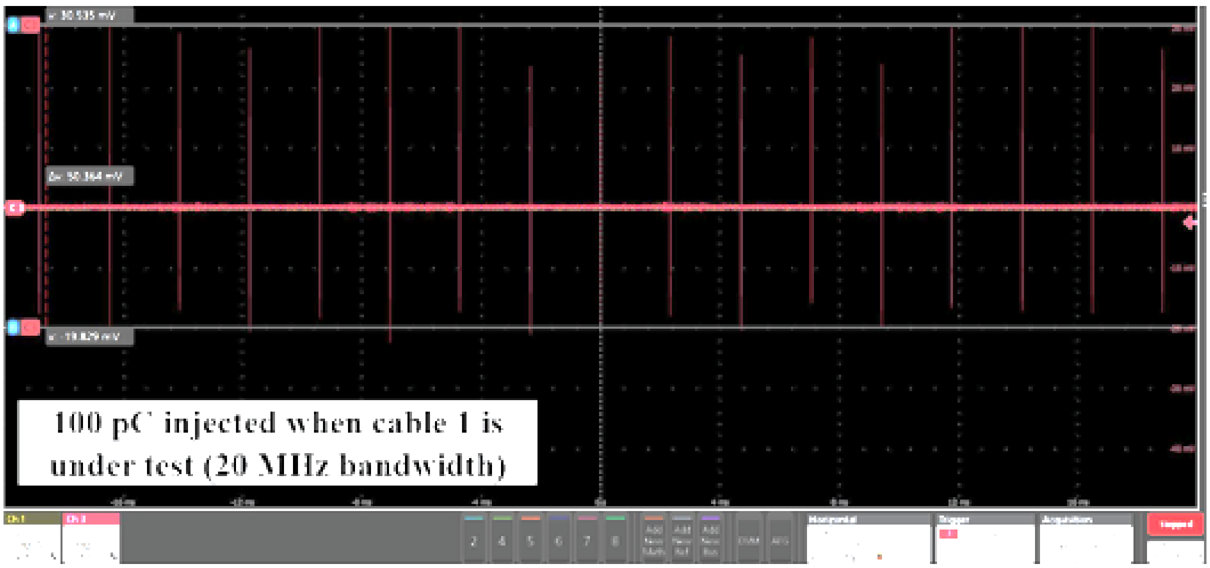

Figure 4-10. *Captured pulses on the scope when 100 pC pulses are injected into the system via a calibrator*

For cables 1, 4, 5 and 6, no PD pulses (~10 pC) can be identified at 15 kV rms excitation level. While statistically significant testing would require more time, these results suggest that for this PFA-insulated cable, thermal mechanical aging may be sufficiently slow for cost-effective use as power cable in electrified aircraft.

4.2. Electrical Aging

The electrical contribution to aging becomes dominant when a void grows to a characteristic size of 1 - 10 µm. In that size range, voids near the inner conductor begin to have a sufficiently strong electric field that a transient electrical breakdown can occur in the gas inside the void (also known as partial discharge). As highlighted in the process model, at this point, higher energy electrons are produced that can accelerate the failure rate.

For decades, three-layer sandwiches of dielectric material, which has a hole in the middle layer between two solid layers, have been used as test surrogates for PD in voids of the cable insulation. The approach has provided significant insight into the effects of internal partial discharges.

Extrapolation over orders of magnitude in void size is required, however, to relate the processes measured in laboratory testing in laboratory testing to behavior in service. This is because while the relevant void size in practice is of order several micrometers, the smallest hole achievable for the three-level sandwich typically has a diameter of a few millimeters.

The development, outside of this project, of laser drilling, however, opened the possibility of an assessment of void-size effects. This is because the emerging technology supports the drilling of holes in polymer sheets as small as about 10 µm diameter. This research shows there is a behavioral difference in partial discharges that is void-size dependent.

4.2.1. Partial Discharges in Dielectric Voids

Fundamentally, a partial discharge occurs when the electric field in a void is sufficiently high so that a discharge can propagate from one side of the void to the other. In addition to adequate field strength, there must be an electron available to initiate the discharge. There has been a tendency to attribute the initial charge to previous discharges or radiation. While these effects are relevant when present, it is likely that, thermally, there are always charges trapped at the interface.

An important distinction exists between the dielectric void and the behavior of gas between metal electrodes. Specifically, the dielectric void supports both induced and trapped charge, while in a metal-electrode system, there is only the charge induced by the external field.

Conceptually, the dielectric and the void constitute a voltage divider. At this level of approximation, the E-field in the void is given by the voltage drop across the void divided by a relevant void dimension.

For the materials of interest, it is generally true that for a given applied external voltage, the DC void field is smaller than the AC void field. The polymer is characterized by a dielectric constant ε1 and a resistivity ρ1. Similarly, the gas in the void has values ε2 and ρ2. If an AC voltage is applied, the voltage across the void is given by geometry and the ε ratio. For DC, the void voltage is given by the geometry and the ρ ratio. If the geometry is the same, i.e., the same sample, and the same magnitude of AC and DC voltages are applied, we would expect the void voltages to be different because the ε ratio is different from the ρ ratio. While it is not necessarily true in general, for the relevant polymers, the ratios are such that the DC void voltage is less than the AC void voltage for the same applied voltage magnitude.

A generally used parameter to characterize void behavior is the partial discharge initiation voltage (PDIV). That is the lowest external voltage applied to the system that produces a discharge in the void. Because of material properties, the PDIV for DC is generally higher than that for AC voltage. Therefore, at the same voltage magnitude, there is a greater natural immunity to partial discharge aging under DC than under AC.

4.2.2. Pressure, Temperature, and Compositional Changes

Morshius [71] points out that there are changes in the PD signature with overvoltage, i.e., voltages greater than the PDIV. For a given sample and time, he measured surface resistivity along the gas-polymer interface at the void, finding that it decreased. He attributed the decrease to discharge byproducts, most likely acid due to moisture and/oxygen content, while he ignored pressure, temperature and diffusion effects in the relatively large experimental void studied.

Each PD deposits energy in the gas of the void, which increases the temperature of the gas. Due to the fundamental behavior of gases, e.g., the ideal gas law, the temperature increase produces a related change in the gas pressure. This research project has shown the pressure forces gas along the interfaces in a three-layer test sample.

While this is a confounding factor in accelerated aging, in service, there is a mitigating effect. Although each PD increases the gas temperature and pressure, the thermal conductivity and the mass diffusion through the polymer seek to achieve equilibrium between the gas in the void and the ambient conditions. Consequently, there is likely a rate of energy deposition that is benign, but there is no modeling nor experimentation exploring this condition.

4.2.3. Trapped Charge

Niemeyer [71] summarizes the role of trapped charge in voids. Others [72] have investigated to understand in more detail how the induced and trapped charges affect partial discharge initiation in a void. Recently, the role of trapped charge has gained increasing significance with the growth of power electronics, which has introduced pulse width modulated (PWM) waveform. These waveforms introduce higher frequencies, which produce voltage reversals in times short compared to trapped charge decay. By comparison, lower frequency high voltage systems that have traditionally been the focus of cable life measurements.

PWM waveforms [73] produce partial discharge patterns that differ significantly from those produced under sinusoidal 50/60 Hz excitation. The observed pattern behavior is hypothesized to result from superposition of a signal encouraging space charge growth along with another encouraging electron release.

There can also be a slower trapped charge dynamic under DC due to the dynamics of electric conductivity. Assuming the same physics of a trapped charge as Niemeyer reported, in equilibrium and with no field, there should be some density of trapped charges at the void polymer interface. As a DC voltage is applied, the conduction in the polymer tends to concentrate one polarity of charge on one surface of the void and the other on the opposite surface. Specifically, depending on the E-field direction, electrons will flow to one surface and become trapped, while the field has the electrons preferentially flowing from the void interface resulting in "holes" (to use the language of semiconductors). This will be in addition to any induced charge.

To assess the effects of void surface and insulation bulk resistivities, an appropriate model, based on Gauss's law and current density continuity equation in 2-dimensions, is used:

$$\nabla^2\varphi = -{}^{\rho}/_{\varepsilon} \tag{II-2}$$

$$^{\partial\rho}/_{\partial t} = -\nabla\cdot\boldsymbol{J} = -\nabla\cdot(\sigma\boldsymbol{E}) = \nabla\cdot(\sigma\nabla\varphi) \tag{II-3}$$

where, φ is the scalar electric potential, ρ is the charge density, ε is the permittivity, $\boldsymbol{J}$ is the current density, $\boldsymbol{E}$ is the electric field, and σ is the electrical conductivity. In general, conductivity is a function of the E-field stress and temperature, so the conductivity gradient is included in the simulation. The governing equation can be rewritten as:

$$-\nabla\cdot\left(\sigma\cdot\nabla\varphi + \varepsilon\cdot{}^{\partial\nabla\varphi}/_{\partial t}\right) = 0 \tag{II-4}$$

In a 2-D cylindrical coordinate system, Fig. 4-11, the anode is set at a DC potential while the cathode is set as 0 V. The boundary on the right is set at zero flux, which means that the E-field along the *r* direction is zero on the boundary of the coupon. The interfaces are addressed in the governing equation.

To address sidewall conductivity, a 100 µm thick, conductive layer between the defect and polymer is assumed. Under repeated PD, the electrical resistivity of this interface may become lower than that of the bulk material. The governing equation is solved via finite difference method.

For the model, the relative permittivity of air and copper electrode is 1, while the relative permittivity values of the polymer and surface are both 2.3. The electrical conductivity of air is $5\cdot10^{-15}$ S/m and the electrical conductivity of the polymer is expressed using the following empirical equation:

$$\sigma PP(r,z) = \sigma PP^0 \left({|E(r,z)|}/{E_0} \right)^v \tag{II-5}$$

where $\sigma_{PP}(r, z)$ is the polymer electrical conductivity. $E(r, z)$ is the electric field stress. v is a fitting coefficient. σ_{PP}^0 is PP conductivity when the field equals E_0.

The model can also include the effect of the temperature field by integrating the thermal dynamic equation. In the study, σ_{PP}^0 is chosen as $5\cdot10^{-14}$ S/m; E_0 is selected as 10 kV/mm and v is selected as 2, which are numbers from data fitting [74].

Initially, it is assumed that the surface conducting layer has the same properties as bulk polymer to represent an unaged void. To study the transient current flow in the coupon, two conceptual parallel planes are defined as z = 0 (plane 1) and z = -0.4 mm (plane 2) with region 1 being between planes 1 and 2 (Fig. 4-11). Any difference between current flows across the planes is due to the charge decay in region 1. The uniform volume charge density on the layers has a value of 5.25 C/m^3. This value is chosen so that the electric field in the defect, with the deposited charge layers, is slightly lower than the partial discharge inception field. The discharge-induced charge generates a field in the opposite direction to the DC background field. The electric field distribution for the initial condition is obtained using Gauss's law as shown in Fig. 4-12. The average initial field in the defect is about 4.5 kV/mm, which is lower than the discharge inception field of 4.6 kV/mm.

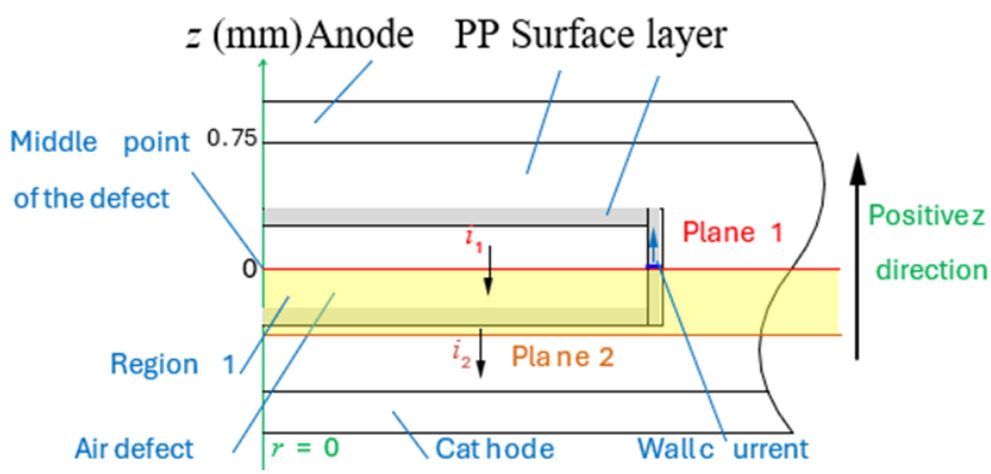

Figure 4-11. *Diagram of the test coupon in 2D cylindrical coordinate system (cylindrical defect)*

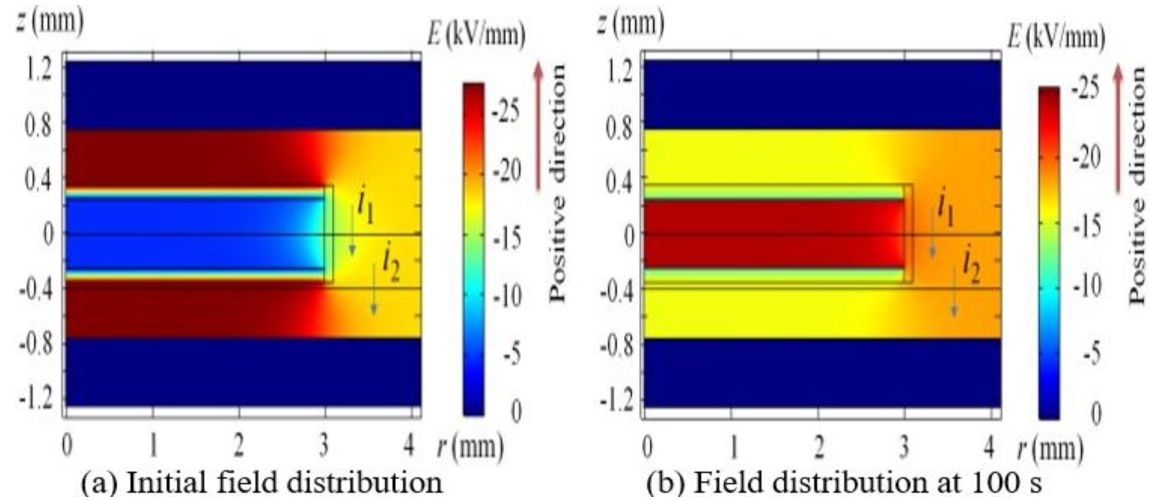

Figure 4-12. *Electric field distribution in the test coupon with the initial space charge density of 5.25 C/m^3 in surface layer (σ_0: $5\cdot10^{-14}$ S/m)*

To investigate charge decay, it is assumed that no partial discharges are initiated in the void as the charge decays and the field increases. The field distribution at 100 s is shown in Fig. 4-12 (b). The average field in the void is about 24.5 kV/mm.

The currents across planes 1 and 2 are shown in Fig. 4-13 (a). The total space charge in region 1 is shown in Fig. 4-13 (b). As time increases, the total charge in this region decays. Most of the space charge moves towards the cathode and gradually leaves region 1. The interface charge density is determined by the substraction between $\varepsilon_{air}E_{air}$ and $\varepsilon_{dielectric}E_{dielectric}$. Thus, in the steady state, the electric field is resistively graded.

If the bulk electrical conductivity of polymer is decreased by a factor of five to estimate sensitivity to this parameter, the charge decay rate also decreases, as shown in Fig. 4-14.

In a second case study, it is assumed that the surface-layer conductivity is one and two orders of magnitude higher than in the previous case, reflecting potential aging caused by previous discharges. With this higher conductivity, most of discharge-induced charge quickly moves to the surface-layer boundary and then slowly migrates to the electrodes (Fig. 4-15). The electric field at the midpoint of the defect is always in the same direction as the DC background field. The rate of field change only slightly increases as the surface-layer conductivity increases.

In the third case study, the initial space charge densities on top and bottom surface-layers are increased to -8.25 and 8.25 C/m^3, so that the total net field in the defect is in the opposite direction to the background field. In this analysis, σ_{PP0} is still chosen as $5\cdot10^{-14}$ S/m and the conductivity of the surface-layer is assumed to be 20x that of the polymer. The initial field distribution and the field distribution at 50s are shown in Fig. 4-16. Even though the initial field at the midpoint of the defect is in the opposite direction of the background field and the conductivity of surface-layer is 20x that of polymer, the electric field in the surface-layer of the defect wall is still in the same direction of the DC background field. Thus, no upward current was observed on the defect wall.

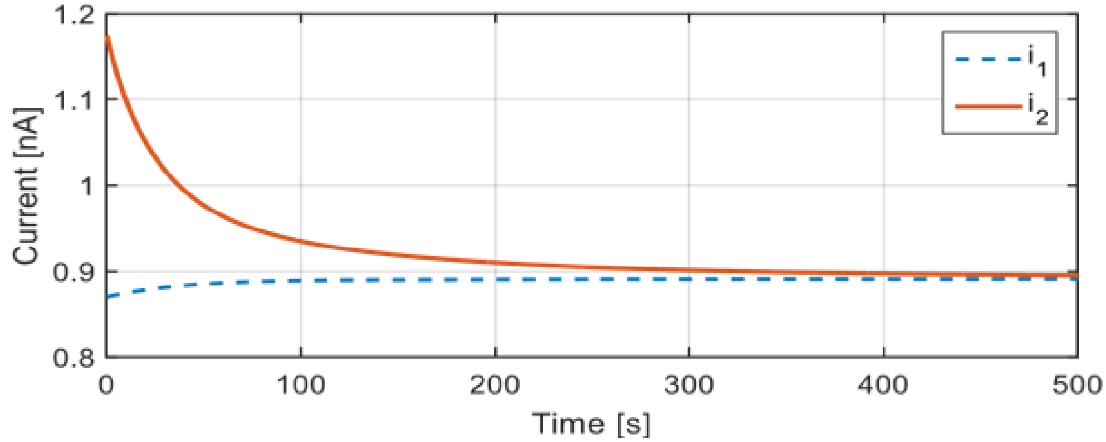

(a) Current flows across planes 1 and 2

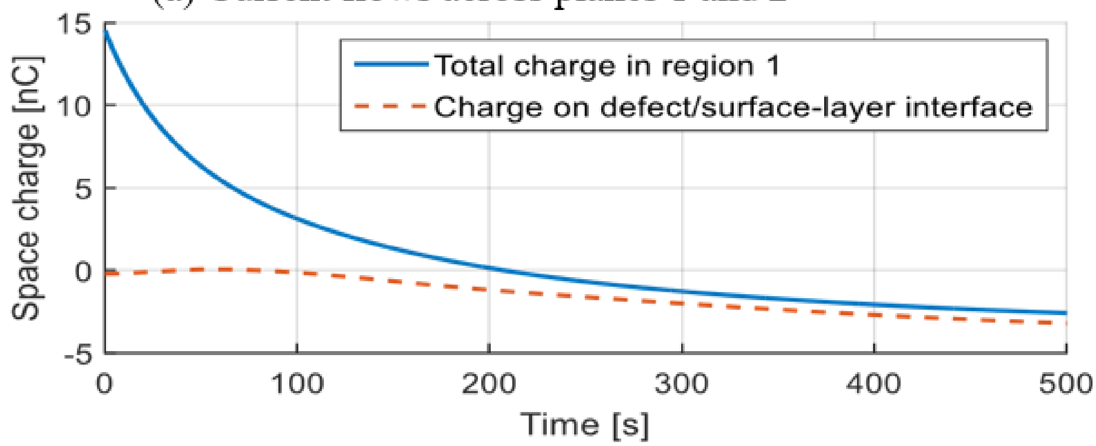

(b) Charge decay in region 1 and charge on interface

Figure 4-13. *Current flow and charge decay in the coupon (σ_0: $5 \cdot 10^{-14}$ S/m)*

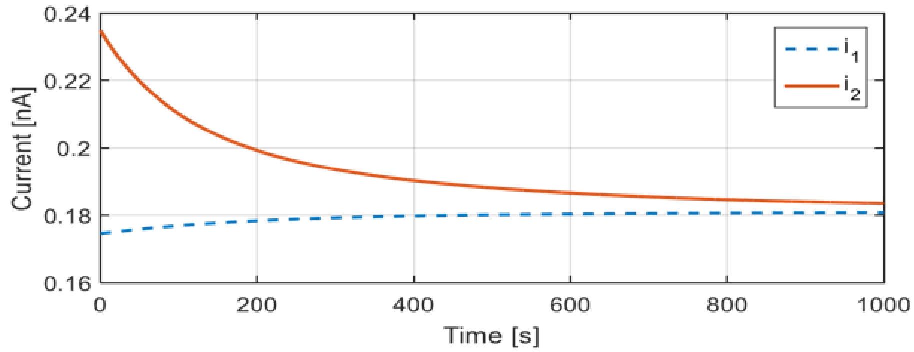

(a) Current flows across planes 1 and 2

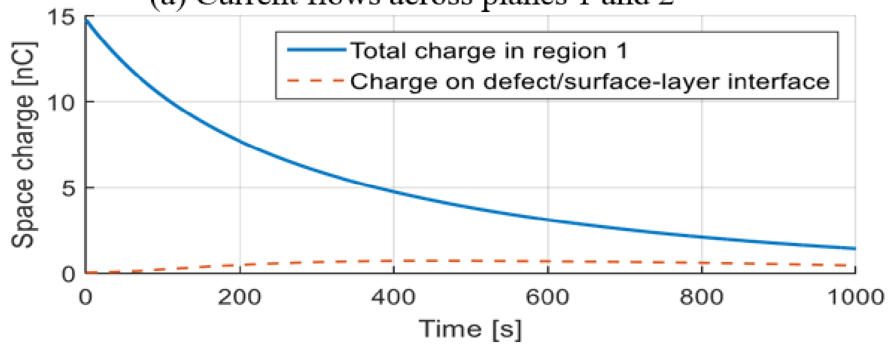

(b) Charge decay in region 1 and charge on interface

Figure 4-14. *Current flow and charge decay in the coupon (σ_0: 10^{-14} S/m)*

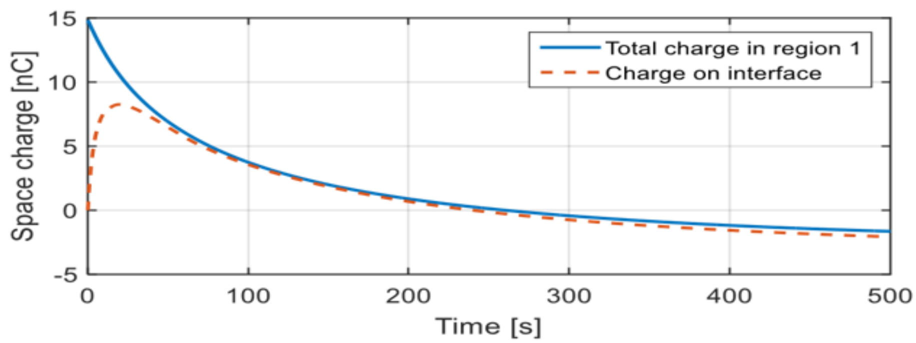

(a) Surface layer σ_0: $5 \cdot 10^{-13}$ S/m

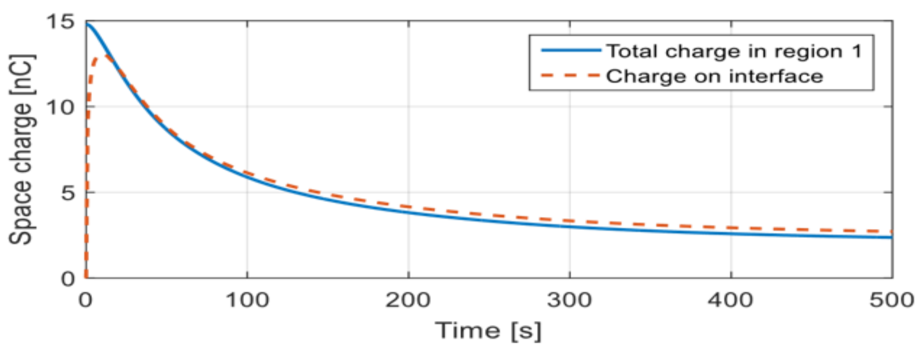

(b) Surface layer σ_0: $5 \cdot 10^{-12}$ S/m

Figure 4-15. *Charge decay in region 1 and charge on interface*

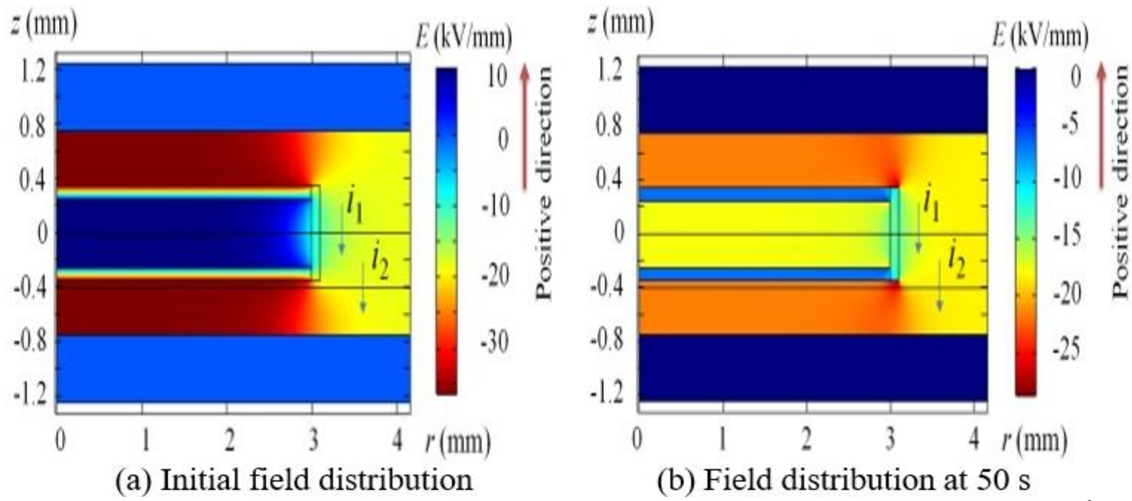

Figure 4-16. *E-field distribution in the coupon with the initial space charge density 8.25 pC/m*^{3} *in the surface-layer*

Fig. 4-17 (a) shows that the change rate of field at the midpoint of the defect slightly increases as the surface-layer conductivity increases by three orders of magnitude. To quantify the current flow on the defect vertical wall, the total current at the middle point of the defect surface vertical wall is calculated and this current is defined as defect sidewall current. The sidewall currents with various surface layer conductivities are shown in Fig. 4-17 (b). The result indicates that even though the midpoint field is in the opposite direction of the DC background field, no upward defect sidewall current was observed.

The bulk insulation properties also influence the DC interfacial charge behavior in internal voids. This hypothesis is indirectly supported by an independent experimental test [75]. Explicitly considering the current flowing through the bulk dielectric provides a more complete explanation for a charge decay mechanism in solid dielectric, which is consistent with published observations [76][77].

Consequently, for completeness, the sensitivity of current flow on the defect sidewall was examined by varying the bulk volume conductivity and surface layer conductivity. The polymer volume conductivity, σ_{PP}^0 , was varied between $5 \cdot 10^{-14}$ S/m and $5 \cdot 10^{-12}$ S/m; the surface-layer conductivity, $\sigma_{surface}^0$, was varied between $5 \cdot 10^{-14}$ S/m and $1 \cdot 10^{-9}$ S/m. If no charge is on surface layers, the wall current flows downward and the current is negative based on the positive wall current direction. To make the current flow upward, equal amounts of negative and positive charges must be deposited on top and bottom interfaces. The initial space charge density on top and bottom interfaces was selected to ensure that the wall current could reach a positive value. When the wall current flows upward, charge recombination takes place.

If the initial charge density is below the surface shown in Fig. 4-18, the current on the defect sidewall is always in the same direction as the background field; otherwise, for points with charge density above the surface, the current on the defect side wall could be opposite to the background field. This suggests that charge recombination can happen when the initial charge density is above the boundary surface in Fig. 4-18. In our case, to generate a wall current in the direction opposite to the background field, the space charge density needs to be larger than 11.2 C/m^3. Consequently, the resulting initial field at the midpoint of the defect needs to be higher than 23.3 kV/mm and be in the opposite direction of background field. This extreme condition is physically not feasible. Since a partial discharge can only reduce the field in the cavity to at most zero but not reverse its direction, such high discharge amplitudes leading to these large values is physically unrealistic.

This simulation shows that conduction in the bulk insulation may be the main channel for discharge-induced charge decay, i.e., more significant than conduction along the void surface. This observation leads to the conclusion that the partial discharge intensity under DC excitation may be mainly determined by the volume conductivity and the applied voltage.

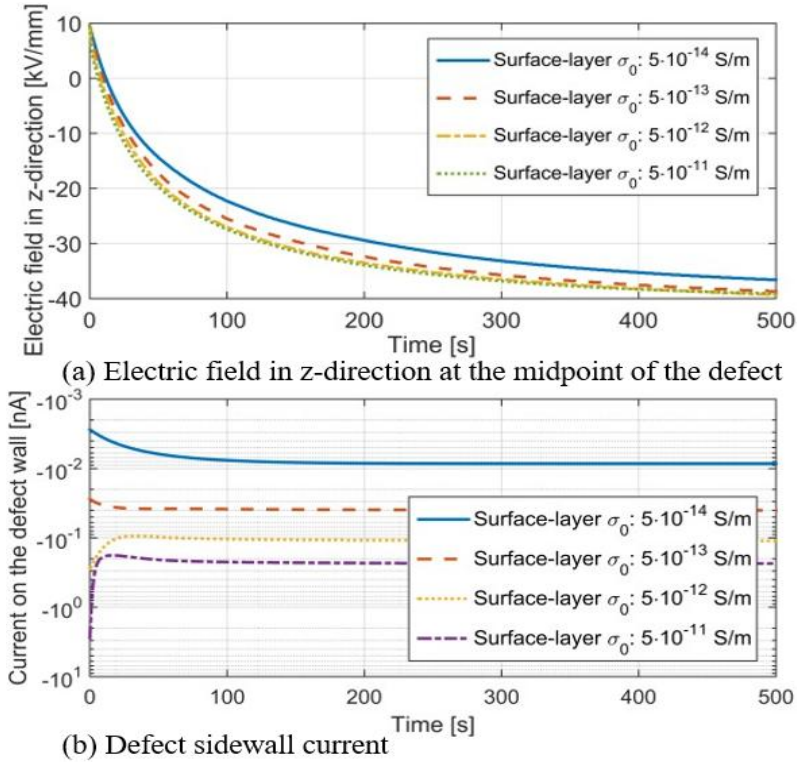

(a) Electric field in z-direction at the midpoint of the defect

(b) Defect sidewall current

Figure 4-17. *The numerical simulation results with the initial surface-layer charge density of 8.25 C/m^3*

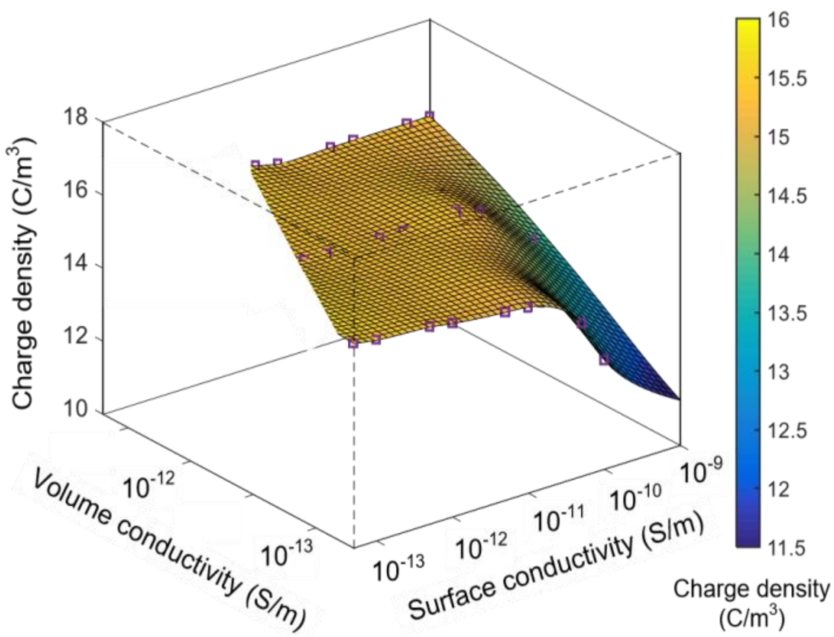

Figure 4-18. *Charge density boundary where defect wall current direction changes sign: for charge densities below the boundary surface, the wall current direction is always the same as the background field; for points above the surface, the wall current is opposite to the background field for a certain period, which will result in charge recombination.*

This heretofore unreported simulation was done outside of this project but informed the experimental approach. The authors acknowledge the contributions of Xianyong Fang and Angello Gattozzi to the understanding of the relative contributions of bulk and surface conductivity for a void.

4.2.4. Space Charge

While interfacial trapped charge can have a significant influence on the void field it is not the only space charge effect. There is also a space charge effect if the cable is used to transmit DC power. Space charge can provide an additional contribution to the void field. Fig. 4-19 shows published data on the phenomena [78].

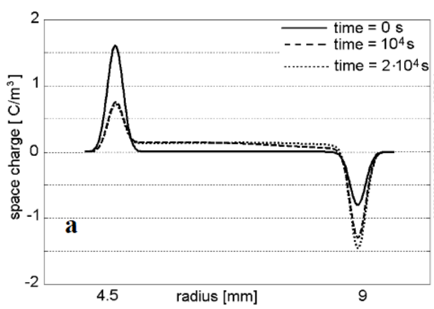

Figure 4.4.a.
Calculated space charge patterns.

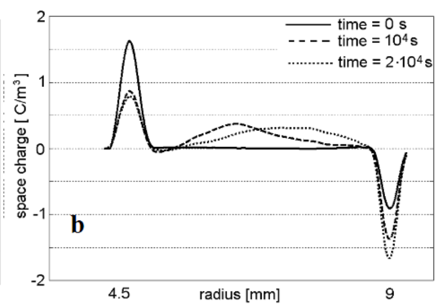

Figure 4.4.b.
Measured space charge patterns.

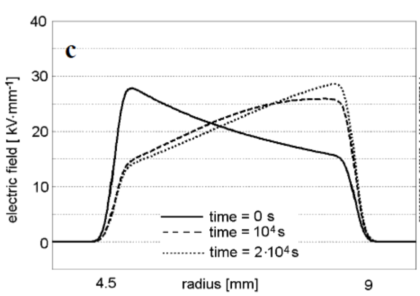

Figure 4.4.c.
Calculated electric field patterns.

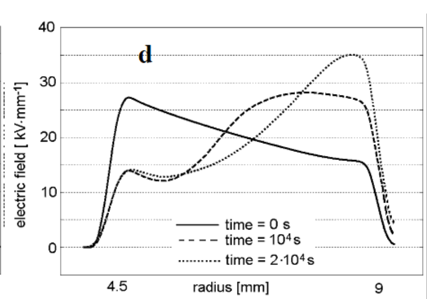

Figure 4.4.d.
Measured electric field patterns.

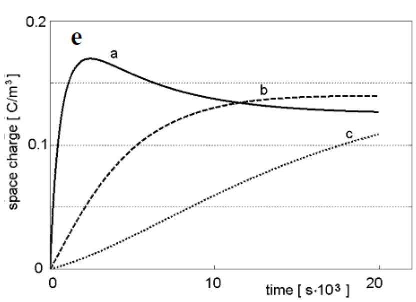

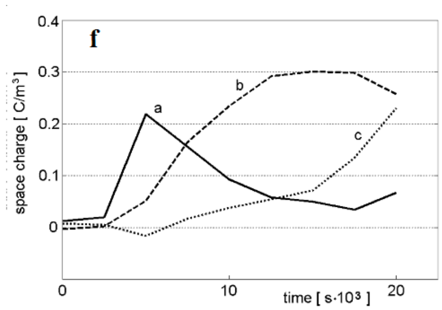

Figure 4.4.e,f. *Evolution in time of space charge in specific locations of a MV XLPE cable. e) Experimental patterns. f)Calculated patterns.*
a) near the inner semicon; r = 5 mm;
b) in the middle of the insulation; r = 6.75 mm;
c) near the outer semicon; r = 8.5 mm.

Figure 4-19. *Space charge simulation and experimental results [74]*

4.2.5. Applicability of Paschen Curve in Voids

The paper [79] asserts and quotes others that the classical Paschen curve is at least approximately applicable in a void. The reason for concern is that the Paschen curve is based on measurements using metal electrodes. The assumed difference is that the electron distribution is different on a dielectric surface than on a metal surface.

4.2.6. Surface Erosion

Studies in a large void, 40 mm diameter, verify the existence of surface erosion and cracking after prolonged partial discharges. The authors, however, attribute the distribution of damage to changes in surface resistivity [80]. This is unlikely because the emission of the initial electron is due to the trap depth of the initiating electron and the local electric field. The paper does not report any efforts to control for water and oxygen which would lead to acid formation by the discharges [81]. The research did, however, detect erosion followed by cracking. The researchers attributed the cracking to electron bombardment without consideration of any role pressure may have caused.

4.2.7. Void Shape

Voids caused by manufacturing defects can be any shape, but for the lengths of cables needed in electric aircraft, manufacturing defects are anticipated to be rare to nonexistent. More likely, void source is growth due to thermal-mechanical cycling. In this case, the void is likely to grow at an interface between crystalline and amorphous regions in the polymer. This probably leads to the most common shape to be quasi-ellipsoidal. Thus, experimental studies on spherical or cylindrical voids are likely to yield valid information.

4.2.8. Surface Resistivity

Surface resistivity in a void is complex because it straddles classical and quantum physics. There are two phenomena that are of interest, liquid formation and trapped charges. It is well documented, that if partial discharges are produced in a void that was assembled in normal air containing O_2 and H_2O, a liquid is produced and that liquid is an acid.

The effect was documented in this research, Figure 46a which showed that it occurs in PFA samples as well as in conventional cable polymers. Thermogravimetric (TGA) testing showed that prior to the partial discharge testing, there were no volatile compounds like water trapped on the PFA surface as shown in Fig.4-20 (b). It is probable that H, C and O in the air of the void will lead to liquid formation.

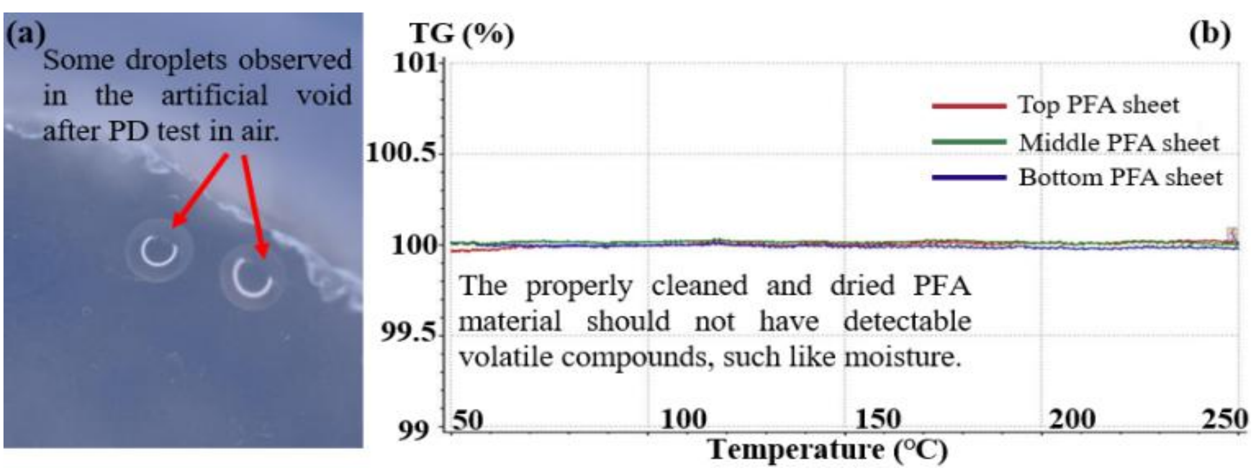

Figure 4-20. *(a) Micrograph of droplets on the PFA surface in the void following extended PD testing in air (b) Tests show no volatile compounds are released from the PFA sheets over the range of 50 °C to 250 °C before the partial discharge test*

As was previously published and re-verified by this research, the acid will not be produced if, for example, the void is fabricated in an atmosphere of dry nitrogen. However, if an acid coats the void interface, it will produce a higher surface conductivity compared to the effective surface conductivity due to the polymer itself. It is also possible that the acid will not coat the full surface but will be concentrated at the lowest point in the void.

In addition to the distribution of the acid produced, the dependance on constituent concentration and other aspects of the environment are unknown. This is critical for applications in electrified aircraft. Voids formed by thermal-mechanical stresses are filled with gases that diffuse from the external environment, but the external air environment varies on time scales shorter compared with diffusion time.

Adding to the complexity is the variety of materials in the diffusion path. The major diffusion path is radially from the cable conductor. On the outside of the cable is a jacket that is impervious to the diffusion of some materials, e.g., ozone. Inside the jacket are a wire mesh and a semiconductor layer, both outside of the insulating polymer. Thus, it is the diffusion through this complex structure rather than just through the primary insulating material that determines the concentration of the gas inside the void.

Since the ends of the cable are not hermetically sealed, there is also longitudinal diffusion. While this is critical for pressure equalization, the effect of this phenomenon on the constituents of the gas in the void is unstudied. So, it is unclear as to whether there will be a critical concentration of O_2 or H_2O when the energy deposited by the partial discharge is adequate to initiate acid formation. In this research, the influence of this confounding factor was eliminated by operating in dry nitrogen rather than air. More data and modeling, however, are needed to predict whether there is an operational problem due to this phenomenon.

Even without the challenge of acid coating, there are ambiguities surrounding the concept of surface resistivity at the polymer-gas interface at the void. Fundamentally, the electron conduction mechanism is likely dominated by trapping and de-trapping of the electrons by the polymer chains [82]. Niemeyer [83] captured this conceptually for the interface with the notional equation:

$$\dot{N}_e = \frac{A}{e} S \cdot exp - [\frac{\phi - \sqrt{\frac{eE}{4\pi\varepsilon_0}}}{kT}](1 - {}^{\eta}/_{\alpha}) \quad \text{(II-6)}$$

The important factor in this equation is the exponential. This gives the probability of de-trapping an electron as a function of the applied field. The trap depth is given by Φ. kT is the thermal energy available, and the parameters under the square root sign indicate the energy provided by the electric field. The most likely assumption is that this trapping and de-trapping activity occurs throughout the polymer. It is likely the fundamental process leading to the resistivity.

In operation, it assumes that electrons flow from a lower electrode to an upper electrode. This will provide excess electrons at the lower void interface and de-trap the electrons at the upper interface. This affects the real charge density as well as the induced charge density. Along the vertical edge, electrons will be absorbed by the traps, and will be emitted either into the polymer or the air gap stochastically.

This means that the surface resistivity should be voltage dependent because the probability of moving an electron by the electric field is a function of the electric field strength. So, it is a relatively meaningless term. This is consistent with the analysis in the Trapped Charge section.

4.3. Electric Aging Under Partial Discharge in Void

The electrical-mechanical-thermal growth of voids in polymeric insulation is a factor in cable life. To study the fundamental process fundamentally, the community has used a three-level sandwich of the dielectric material under test, in Fig. 4-21 [84][85][86][87][88][89][90][91][92][93][94][95][96][97][98]. A hole is made in the middle layer to provide a location for partial discharge development.

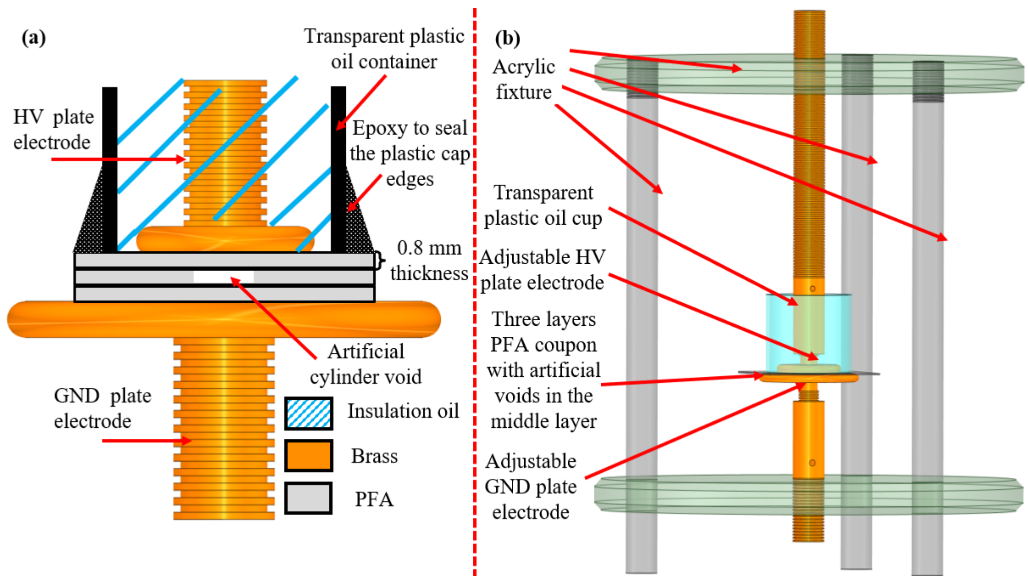

Figure. 4-21. *PFA accelerated aging test with internal PD (a) An artificial void test sample with parallel plate electrodes (b) Adjustable test fixture to hold the three-layer PFA test coupon between two electrodes*

Advances in laser drilling have made it possible to drill holes with diameters as small as 10 µm, permitting an investigation into the changes in phenomena that can be expected in the void diameter range from 10 micrometers to a few thousand micrometers. Differences are expected because, for the conventional geometry, the middle layer is of constant thickness. Consequently, changes in diameter over that range can lead to changes in void volume of about five orders of magnitude. At a macro level, the changes can be separated into changes in the electric field distribution and changes in the pressure and temperature, which are related via an appropriate gas law. Partial discharges deposit energy in the gas, raising temperature and pressure. In addition to coupling via a gas law, each parameter returns to equilibrium with the ambient conditions via different diffusion processes.

4.3.1. Experimental Approach

The schematic for the experimental setup is shown in Fig. 4-22. The line frequency (60 Hz) sinusoidal excitation is selected throughout the various tests. For partial discharge testing, a high frequency current transformer (HFCT) or a standard measurement impedance converts the partial discharge current to a measurable pulse signal. A C-L-3C filter reduces noise from the power supply. This setup supports AC partial discharge tests up to 30 kV with background noise lower than 10 pC. The experiments are performed in a cylindrical stainless-steel tank, which is approximately 3 meters long and 1 meter in diameter. At atmospheric pressure, this test chamber is discharge-free up to ~20 kV rms.

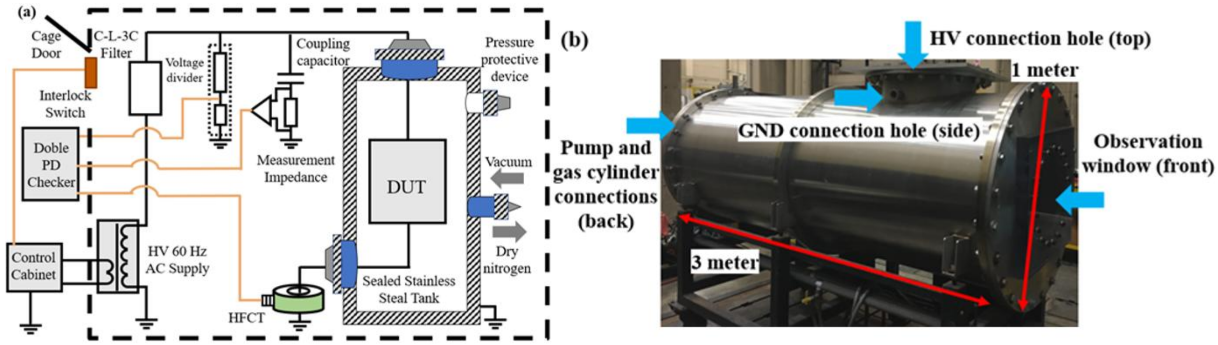

Figure. 4-22. *(a) The schematic for the long-term PD aging test setup with (b) picture of the sealed stainless-steel tank in use*

4.3.2. Analytical Approach

The focus of this investigation is the prediction of the variation of the electric field distribution in the void for the range of void sizes. A conventional approach would be to use finite element analysis. A boundary-element approach was chosen, however, as experience has shown the approach to be straightforward and robust in these situations. A summary of the analytical approach is presented in Appendix I.

4.3.3. Electric Field Simulation Results

In this section, multiple simulation cases have been conducted to understand how the electric field (E-field) distribution in the void can be influenced by the geometrical parameters of the test samples and the relative permittivity of the selected insulation material. All the simulation cases can be divided into four categories, which will be mentioned as Case 1, Case 2, Case 3, and Case 4 in the following part. The major parameters of these four categories can be found in Table 4-2 and the difference among these simulation cases can also be identified there.

Table 4-2. *Major geometrical parameters of the test samples and the relative permittivity of the selected insulation material applied in different simulation categories*

	Insulation Material Relative Permittivity	Void Diameter (µm)	Top and Bottom Layer Thickness (µm)	Middle Layer Thickness (µm)	Void Corner Radius (µm)
Case 1	2.06	2000	800	800	A
Case 2	4	2000	2000	2000	B
Case 3	2.06	100	X	X	Fixed
Case 4	2.06	100	Y	800	Fixed

* A, B, X and Y are variables which mean parameter sweepings are applied for that simulation case and geometrical dimension as indicated in the table.
**The same variable X occurs in two locations of Case 3 which means the values of those two geometrical dimensions are always the same during the parameter sweeping study.

Five different situations are analyzed to provide insight into the electric field distributions that can occur within a void. Case 1 considers a 2000 µm diameter void, which is deemed representative of the large, mechanically produced voids in existing studies. Additionally, the electric field magnitude along the void periphery is further affected by the curvature of the void corner. For example, the void corner curvature affects PD initiation, which is influenced by the trapping of charges at the corner of the void ceiling. The geometry used in this simulation is shown in Fig. 4-23 and results are reported in Fig. 4-24.

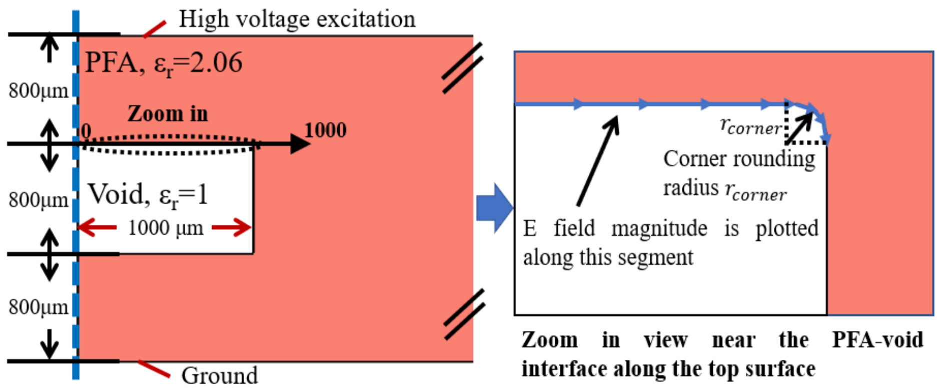

Figure. 4-23. For a void of the 2000 μm diameter, the electric field is calculated along the void ceiling and plotted along the highlighted segment for various corner rounding radii. The voltage magnitude applied in this simulation is 12 kV rms under 60 Hz sinusoidal excitation

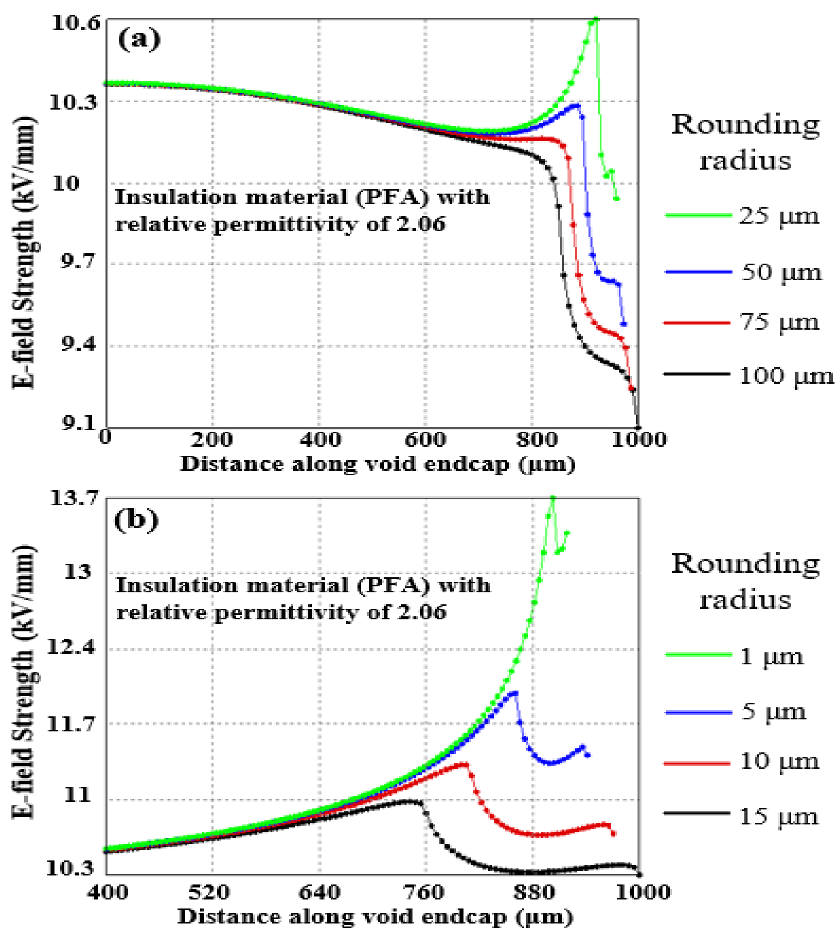

Figure. 4-24. Case 1 simulations: the electric field distribution along the void ceiling as an example with the 2000 μm diameter, under various corner rounding radii, (a) 100 μm, 75 μm,50 μm, and 25μm and (b) 15μm, 10μm, 5 μm, and 1 μm

Fig. 4-24 (a) and (b) show that before the corner rounding radius drops below 50 µm, the peak E-field will be at the center of the void. By comparison, when the corner rounding radius becomes smaller than 50 µm, the peak E-field will be at the corners. A smaller corner rounding radius will exhibit an even more intensified E-field magnitude along the corner than the center. Mechanical drilling or cutting produces relatively large corner radii, leading to minimal edge enhancement of the electric field.

In Fig. 4-23, the relative permittivity is selected to be 2.06. Commonly used polymeric dielectrics, such as XLPE, PP, EPR, PVC, typically have permittivity ranging between 2 and 4. Thus, as shown in Fig. 4-25, for the Case 2 simulations, after increasing the relative permittivity to 4, the peak electric field strength increases, but it has negligible influence on the electric field distribution in or near the void region. By comparing Fig. 4-24 and Fig. 4-25, the higher relative permittivity of the dielectric results in a larger E-field growth at the corners. The difference between the E-field magnitude near the corner and the void center increases more than three times as the relative permittivity of the polymer material in use is doubled.

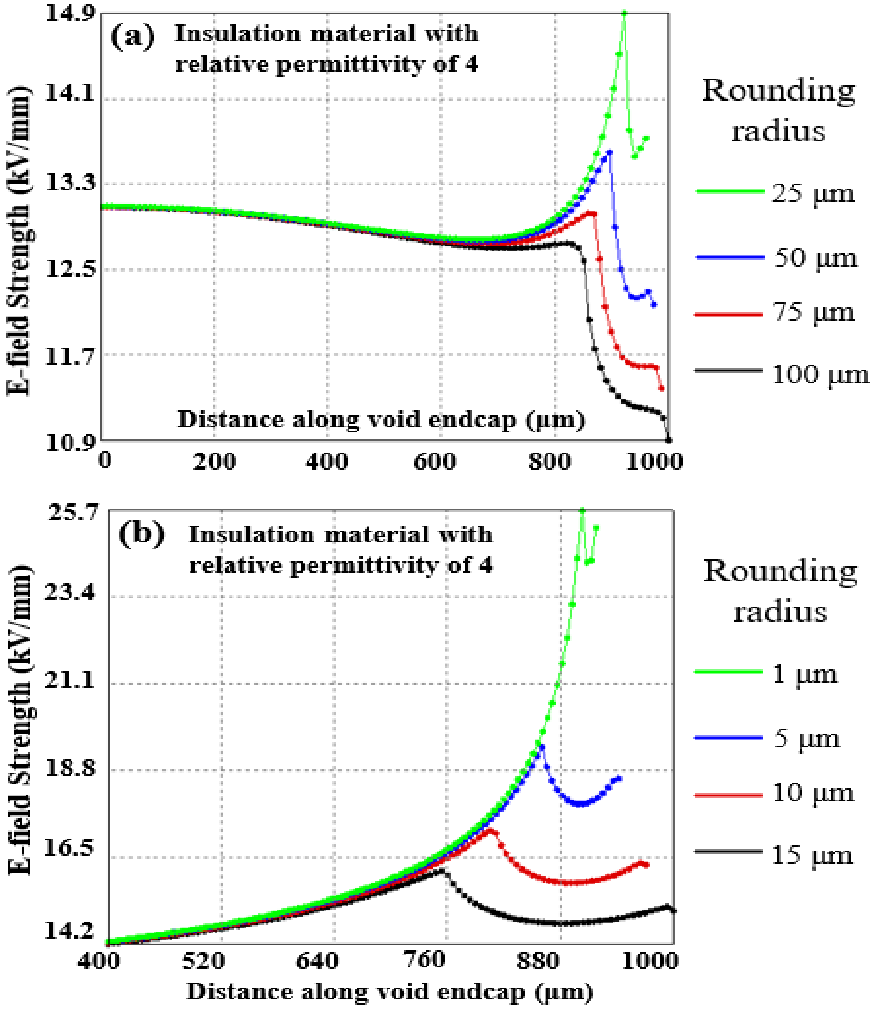

Figure. 4-25. *Case 2 simulations: if a polymer material with relative permittivity of 4 is applied instead of the PFA, the electric field distribution along the void ceiling of 2000 µm diameter with various corner rounding radii follows (a) 100 µm, 75 µm, 50 µm, and 25µm (b) 15 µm, 10 µm, 5 µm, and 1 µm*

By varying the corner rounding radius, the same trend can be observed for small voids with a diameter less than 1 mm. For voids with diameters like 800 µm, 600 µm, 400 µm, 200 µm and 100 µm, the electric field at the corner along the void periphery becomes dominant as the rounding radius is reduced. As a general conclusion for voids with a diameter less than 1 mm, if the corner radius is less than 5% of the void diameter, the electric field along the corner for the void is larger than that near the center of the void.

To match the experiments in the later sections, more simulation cases are studied with void diameters in the range between 10 µm and 500 µm. Since the E-field distribution is similar, only the results under void diameter of 100 µm will be presented in Case 3 and Case 4.

Case 3 investigates the effect of the PFA layer thickness for all layers with the same thickness. The electric field intensity along the PFA layer thickness direction is fixed at 5 kV/mm in all simulations. With each PFA layer thickness of 200 µm, 400 µm, 600 µm and 800 µm, the simulation results are summarized in Fig. 4-26. This analysis shows that for layer thicknesses are large compared to the void size, enhancement of the electric field at the void corner always occurs as predicted in Case 1.

Case 4 analyzes the situation for which the central layer is fixed at the thickness of 800 µm and the thickness of the top and bottom PFA layers are changed. Other simulation conditions are the same as those in Case 1. A typical electric field distribution is represented in Fig. 4-27 with a 100 µm diameter void. The enhancement of the electric field at the void corner can be found in all simulations as shown in Fig. 4-27.

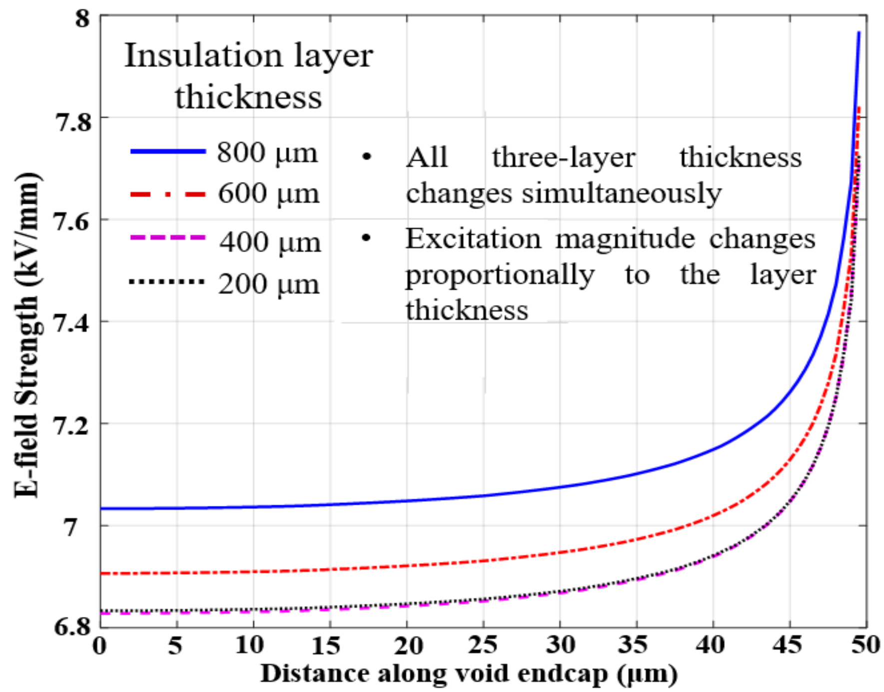

Figure. 4-26. *Case 3 simulations: Electric field distribution along the void ceiling with 100 µm void diameter, under various PFA thickness 800 µm, 600µm, 400 µm, and 200 µm*

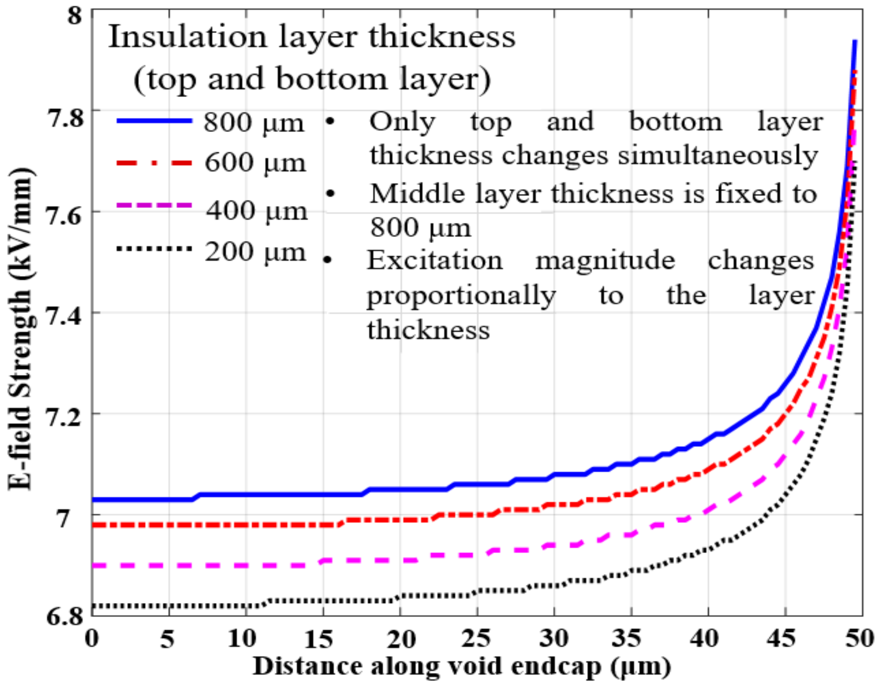

Figure. 4-27. *Case 4 simulations: Electric field distribution along the void ceiling with 100 µm void diameter, under various top and bottom PFA layer thickness 800 µm, 600 µm, 400 µm, and 200 µm, while the middle PFA layer thickness is fixed to 800 µm*

4.3.4. Agreement Between Experiment and Analysis

Initial testing focused on a middle layer with eleven holes of different diameters. The pattern used has one hole of each 500 µm, 300 µm, 150 µm, 100 µm and 70 µm diameter, three holes with 30 µm diameter, and three holes with 10 µm diameter, as shown in Fig. 4-28. The distance between adjacent holes is greater than 5 mm, while the shortest distance from a hole to the high voltage electrode edges is about 6 mm. All holes are within the parallel plate electrode shadow area. Thus, the E-field distortion inside the voids introduced by the electrode edge effect is avoided by allowing sufficient distance to these edges. In addition, interactions among adjacent holes can be ignored due to their large separations.

The laser-drilled polymer sheets are prepared by cleaning with alcohol and deionized water, followed by baking at 105℃ for 4 hours to remove any moisture. After cleaning, the quality of the holes and their nearby regions can be observed, Typical data is shown in Fig. 4-29. The hole size is about 30 to 50 µm larger than specified, and the hole shape is not perfectly circular, due to the laser cutting process.

Based on the simulation, streamer initiation in laser-drilled small voids will appear at the void circumference. After the streamer occurs, it causes the local electric field to be much different than the geometric electric field, which usually prevents other streamers in the nearby region [99]. As the streamer develops, it erodes the overlapping regions of the top and bottom PFA layers. This matches the observed erosion patterns from the experiments in Fig. 4-30.

In these figures, as the analysis predicts, the erosion is concentrated at the circumference with little or no erosion at the void center. Both analysis and experimentally observed erosion patterns showed that for the smaller voids, the electric field distribution drives the partial discharge activity away from the center of the void and to the periphery. This leads to a different erosion pattern in smaller voids than larger ones, adding heretofore unrecognized complexity to the extraction of cable life estimates from coupon data.

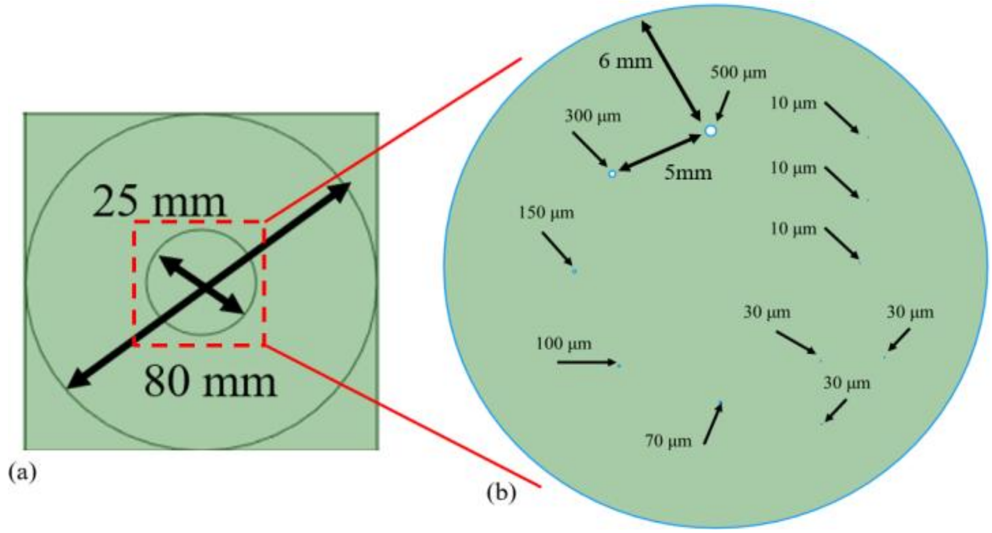

Figure. 4-28. *Laser drilled PFA proof sheet (a) Top view of the 80 mm by 80 mm PFA sheet with all holes drilled in the center circular area of 25 mm diameter (b) The zoom-in view of center area with eleven holes*

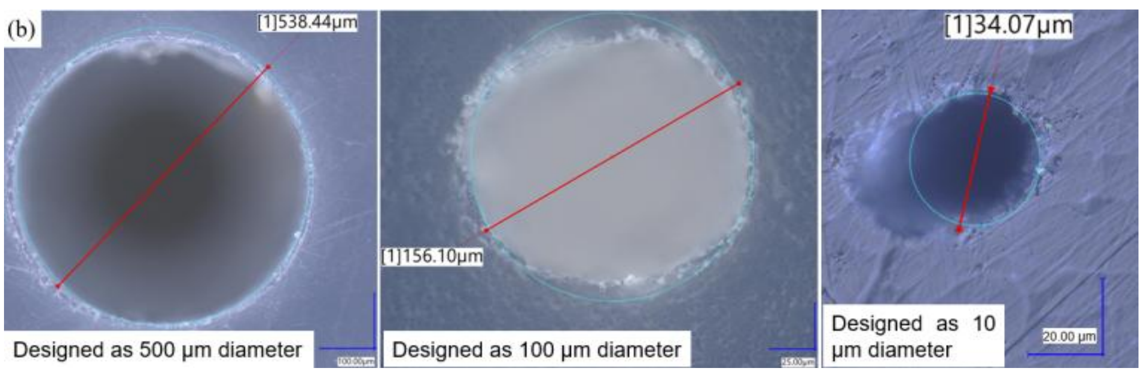

Figure. 4-29. *Received laser drilled PFA sheet under microscope check (the PFA sheets are properly cleaned and dried before checking)*

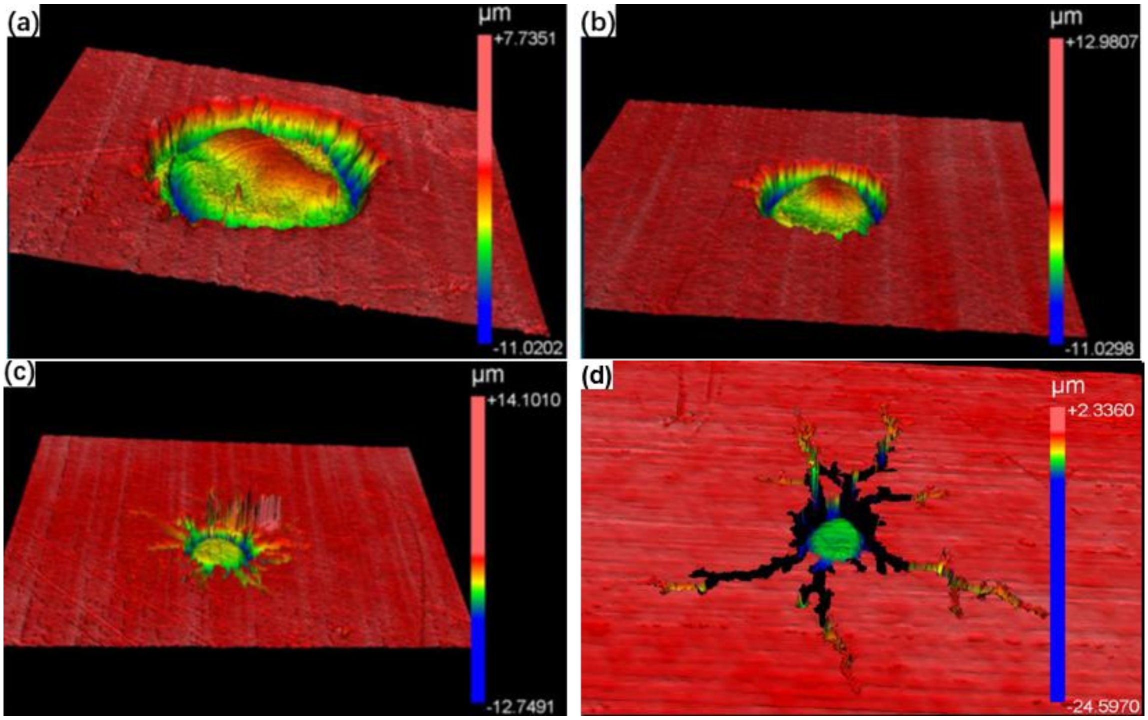

Figure. 4-30. *Erosion pattern from partial discharges in a cylindrical void with nominal diameter (a) 500 μm (b) 300 μm (c) 150 μm (d) 100 μm*

4.3.5. Discussion About Pressure and Temperature Effects in Void

After the streamers occur, the partial discharge energy, which is dissipated in the void, leads to the temperature and pressure rise of the gas inside the void. The different pressure effects occur in smaller volume voids than in larger volume voids.

Since the background electric field strength among all void diameters are similar, the partial discharge energy difference among samples can approximated by the charge level of the partial discharges. Although the void volume has about 400 times difference (100 μm diameter vs. 2 mm diameter), their partial discharge charge rate only has 5 to 20 times difference. It means that the partial discharge energy density deposited in a 100 μm diameter void should be 20 to 80 times higher than that in the 2 mm diameter void. Thus, the expected pressure rise difference between the two cases can be understood by approximating the ideal gas law.

$$PV = nRT = NkT \tag{II-7}$$

where P is the pressure in the void, V is the volume of the void, n is the number of moles and R is the universal gas constant, the number of molecules is N and k is the Boltzmann constant.

Based on the ideal gas law and the charge rate measured experimentally, the pressure increases inside the 100 μm diameter void can be tens of times lower than that in 2 mm diameter void. The elevated temperature and pressure can lead to an aging process that supplements the aging to high energy electrons. Evidence comes from the design and implementation of the test approach. In a naturally occurring void, the resistance to crack initiation has variability due to the micro-morphology of the polymer, but no preferred directionality. The standard three level sample, however, has two interfaces orthogonal to the geometric electric field.

This research managed interface sealing using two approaches. One was mechanical pressure, and the other was thermal bonding. The mechanical pressure approach was to control the pressure on the sample by tightening the electrodes against the polymer sample. After extended partial discharge activity, there was significant erosion along the layer interfaces. Examples of the erosion patterns are shown in Fig. 4-31.

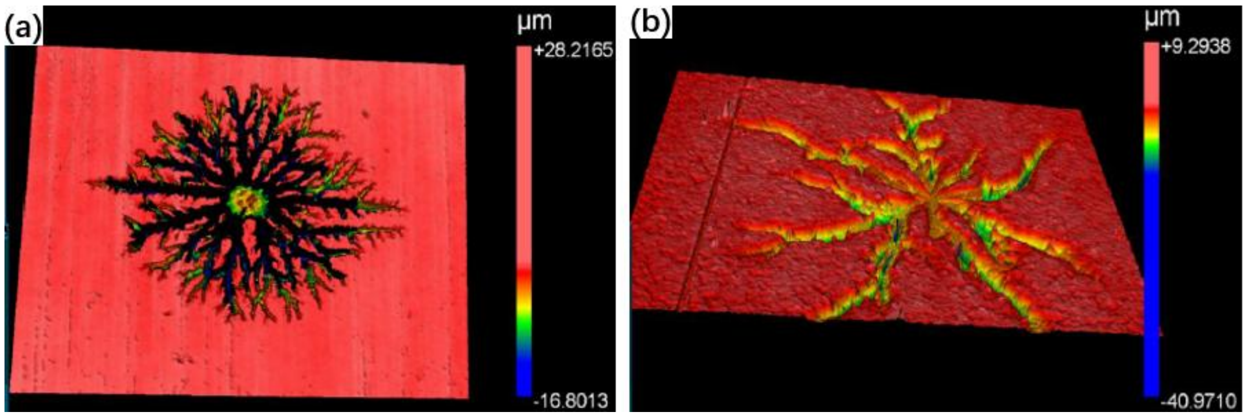

Figure 4-31. *Interfacial erosion, orthogonal to the applied electric field for (a) 70 μm and (b) 10 μm diameter holes in the center layer of polymer*

Since the growth is orthogonal to the applied electric field, the assumption is that this growth is driven completely by the temperature and pressure of the gas in the void. This orthogonal erosion is expected to be an artifact of using the three-layer sandwich geometry for accelerated aging. In service, the cable will experience a much lower rate for partial discharge activity providing more time for thermal conductivity and mass diffusion through the bulk polymer to reduce both temperature and pressure. If, however, the pressure and temperature become sufficiently high in a void produced via a thermal-mechanical process, cracking at the mechanically weakest part of the bulk polymer at the void-bulk interface is expected to occur.

The orthogonal growth demonstrated that improved interfacial sealing is required to support accelerated aging. Consequently, a molding approach was developed to seal the interface. The procedure is shown in Fig. 4-32. There is a metal mold that heats a three-level dielectric sandwich with, as is conventional, a hole in the central sheet. The diameter of the cavity is 5 cm. Upon cooling, a PFA simple with artificial void is fabricated, which should be close to the sealed void in the cable insulation system.

This approach, while promising, was developed at the end of the project. So, there is promising electrical data, but it is insufficient to draw definitive information. To assess the proposed process One prototype was fabricated using this method with the mechanically drilled hole (about 250 μm diameter). This void can be observed after the molding procedure.

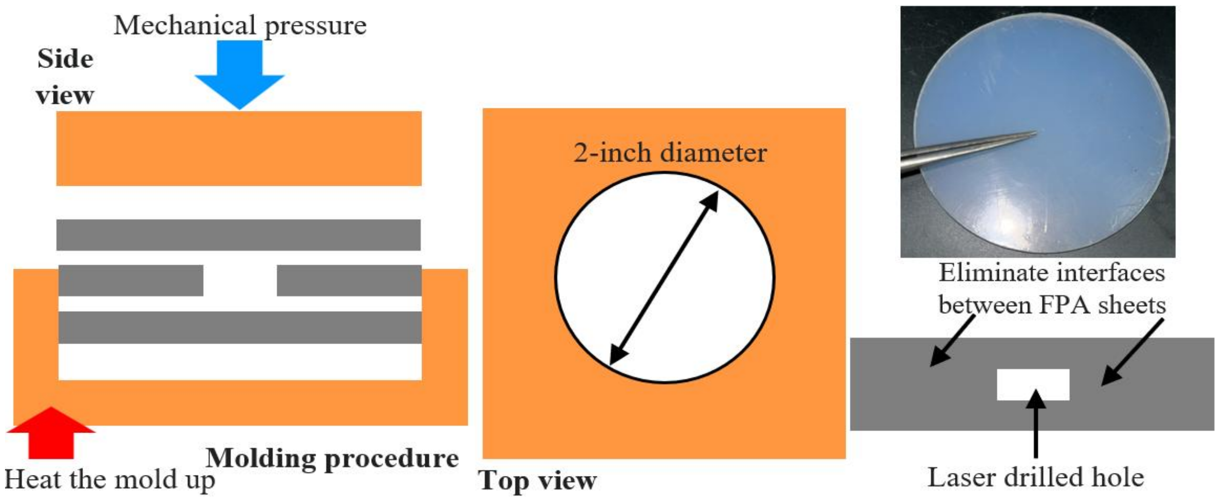

Figure 4-32. *The molding procedure to eliminate the interfaces among the three-layer PFA coupon*

Due to the promise shown by the prototype, two types of molded test coupons were fabricated and tested. As shown in Fig. 4-33, the coupons, consist of 127 µm thick PFA layers with a laser drilled hole, either about 500 µm (Type I) or 100 µm (Type II) diameter near the center of the middle layer. After molding, the hole in the middle layer can be observed under microscope while a more accurate dimension check needs to be applied by using Micro CT, as shown in Table 4-33.

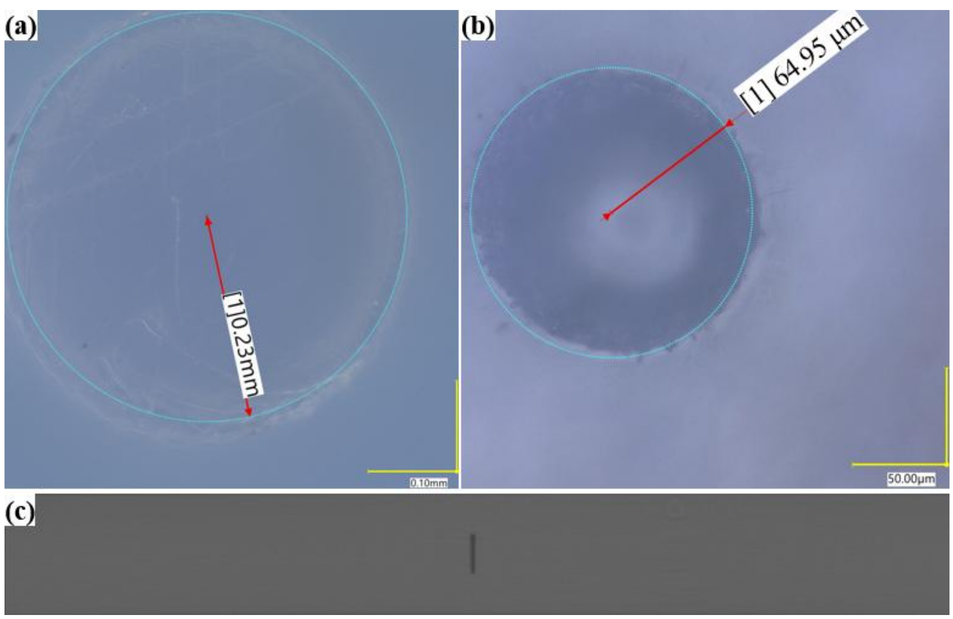

Figure 4-33. *Molded sample (a) the shape and estimated hole size (500 µm target) after molding procedure under microscope check (b) the shape and estimated hole size (100 µm target) after molding procedure under microscope check (c) the side view picture of molded sample under Micro CT check*

Under the Mico CT check, from Fig. 4-31 (c), a good attachment among the layers can be confirmed, since no other defects along the layer interfaces can be identified. Based on Table 4-3, the PFA layer thickness may have about ±20 µm difference than the specific thickness of 127 µm due to the tolerance of the material and the possible thickness change during the molding procedure. Meanwhile, for the hole diameter estimate, about up to ±50 µm error is expected for the nominal500 µm one and about up to ±20 μm error is expected for the nominal 100 μm hole, which is majorly introduced by the inaccuracy of laser drilling step.

Table 4-3. *An example of about hole depth and size measurement under Micro CT check*

Sample	Hole Diameter		Hole Depth	
	Target (μm)	Actual (μm)	Target (μm)	Actual (μm)
Type I	500	457	127	102
Type II	100	100	127	152

Using the stencil mask method, two very thin layers of sintered silver material are applied to the outer surface of the sample, as shown in Fig. 4-34 (a). The smaller metal pad is the high voltage electrode while the larger one is ground. The sample is submerged in oil to eliminate surface discharges. The oil tank and electrode system are shown in Fig. 4-34 (b). The stainless-steel electrodes are polished to achieve parallel surfaces. Moreover, the natural ester oil is dried and degassed according to the standard [100]. After partial discharge aging, if breakdown occurs, black marks in the regions which overlap the void can be identified, while no surface discharge signal or evidence can be found along the coupon surfaces. As a comparison, clear surface discharge marks can be found in the metal electrode surfaces if the previous setup is applied in Fig. 4-34 (c). Other components of the setup and test procedures are the same as in the previous experiments.

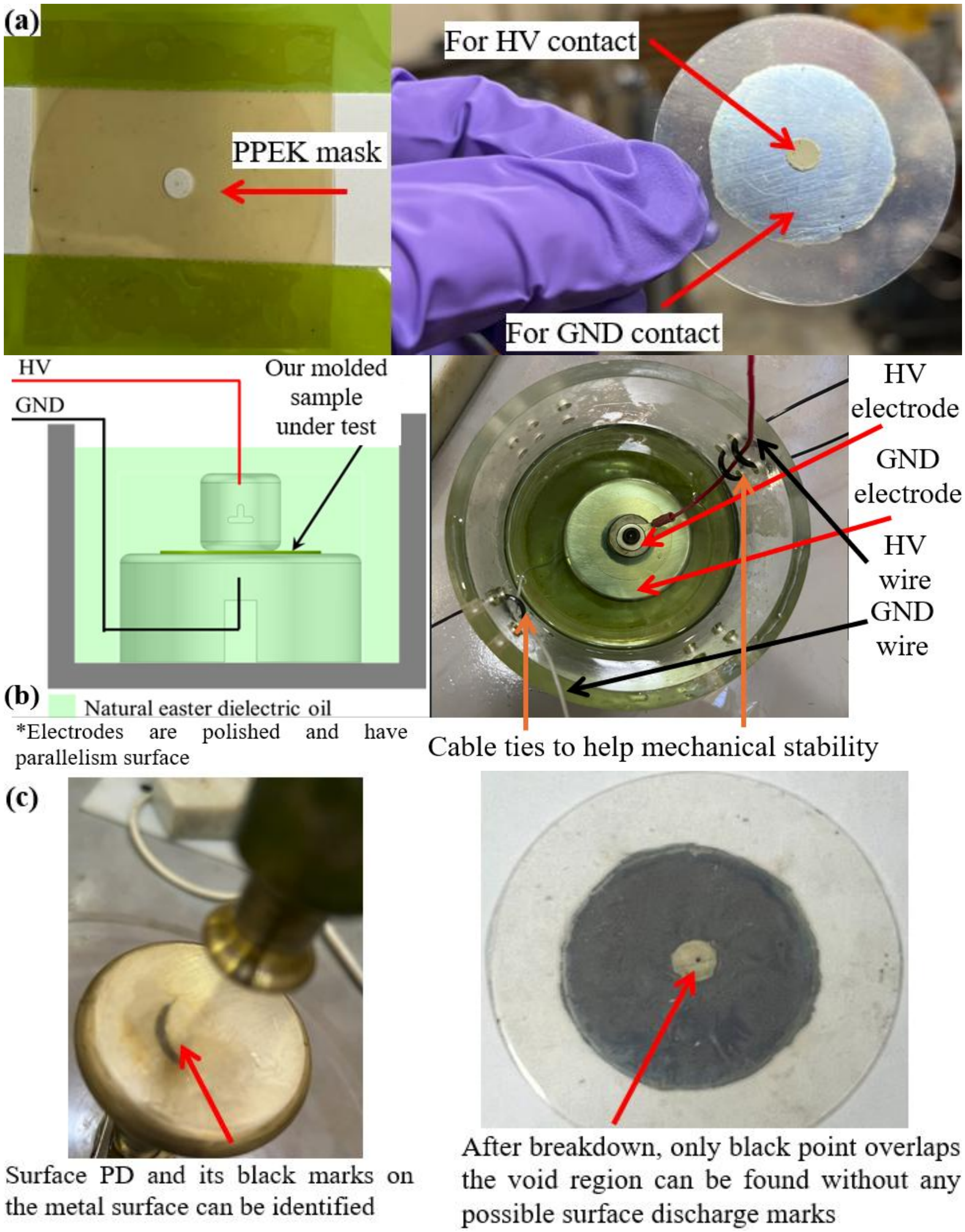

Figure 4-34. *(a) Two very thin layers of silver sinter material applied in each surface of the sample as electrodes (b) Side view drawing of the oil tank and electrodes system in use with a picture of that part setup (c) Black marks introduced by the surface discharges before the improvements and only black marks near breakdown point after the improvements, which support that the surface discharges are eliminated with the setup improvements*

4.3.6. PD Aging Results Comparison Between the Open Interface Samples and the Molded Samples

4.3.6.1. Open Interface Samples PD Aging Results

As shown in Fig. 4-28, With the proof sheet experiments, we found that the void with a nominal diameter of 100 µm becomes critical since breakdown events occur at the lowest voltage for that diameter void. Preliminary measurements indicate that under 60 Hz sinusoidal excitation with 12 kV rms magnitude, breakdown occurred within a few days.

The data, limited by the contract end date, suggested that the partial discharge aging process has three stages. As shown in Fig. 4-35 (a) and (b), in stage 1, the average partial discharge magnitude is around 20~50 pC, while the PD rate is usually about 50~60 events per second in both positive and negative excitation cycles. The aged PFA layer (either the top or bottom) near the void region is demonstrated in Fig. 4-35 (c).

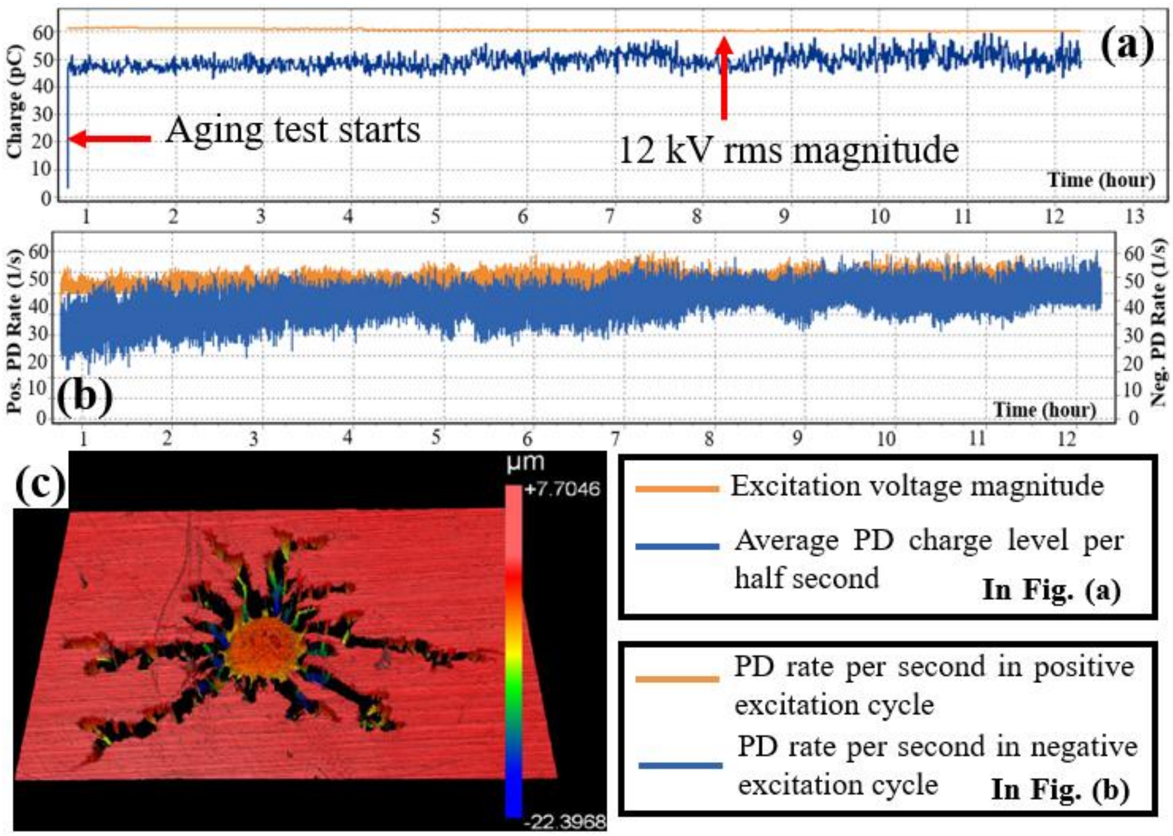

Figure 4-35. *(a) (b): Typical PD behavior for PFA three-layer coupon in accelerated PD aging stage 1 (nominal 100 µm diameter void in middle PFA layer) (c) Aged PFA sheet observed under WLI (in accelerated PD aging stage 1)*

As shown in Fig. 4-35 (c), during the aging stage 1, the material removal along material depth direction is quite shallow, only around 30 ~50 µm, compared to the PFA sheet thickness of 800 µm. Besides, there are also shallow but long valleys, which are initiated around the cylinder void edges and grow along the PFA sheet in-plane direction. This shows that the sealing did not mitigate the interfacial growth to a significant degree beyond what was achieved mechanically.

Partial discharge stage 2 results are shown in Fig. 4-36 (a) and (b). Stage 2 is characterized by an average partial discharge magnitude of 100~200 pC, while the partial discharge rate is usually about 120~180 events per second in both positive and negative excitation cycles. The surface condition under the addition of stage 2 operation is shown in Fig. 4-36 (c).

As shown in Fig. 4-36 (c), comparing the damage observed during the partial discharge aging stage 1, some areas erode more than others. In aging stage 2, erosion proceeds rapidly in these few concentrated sites and seems to remove material along thickness direction much faster. As estimated, the martial removal along the thickness direction should be more than 100 μm and perhaps initiates the so-called electric trees. However, the internal damage structure was not measured.

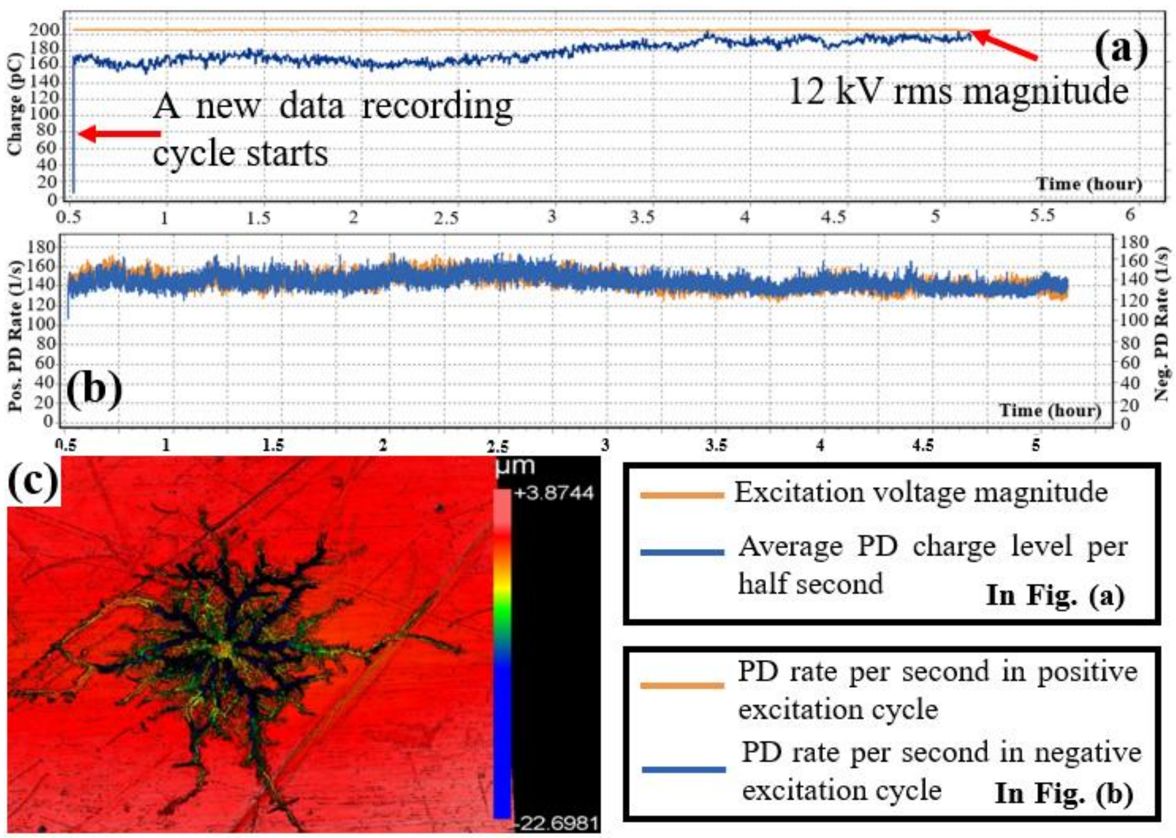

Figure 4-36. *(a) (b): Typical PD behavior for PFA three-layer coupon in accelerated PD aging stage 2 (nominal 100 μm diameter void in middle PFA layer) (c) Aged PFA sheet observed under WLI (in accelerated PD aging stage 2)*

As shown in Fig. 4-37 (a), aging stage 3 has a partial discharge magnitude of around several to tens of several nC. This aging stage lasts for several hours, then the breakdown occurs. By comparison, the duration of aging stage 1 is around 1 to 2 days, while the aging stage 2 lasts for about 1 day.

A typical surface picture is shown in Fig. 4-37 (b). Deep holes in a relatively large area can be observed, which are circled in yellow. Micro CT scanning is applied to resolve the features produced and a typical result is shown in Fig. 4-37 (c). The Micro CT image reveals a channel which spans almost the entire thickness of the bottom PFA layer, but is offset horizontally from the location directly under the void in the middle layer. This is consistent with behavior observed under interfaces sealed only with pressure.

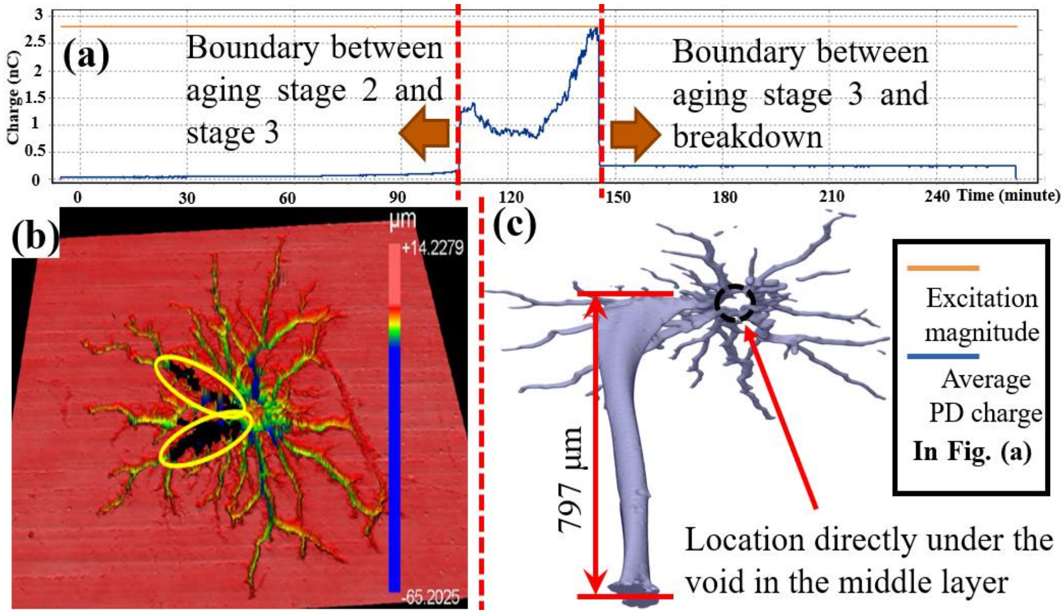

Figure 4-37. *(a) Typical PD behavior for PFA three-layer coupon in accelerated PD aging stage 3 (b) Aged PFA sheet observed under WLI (c) Micro CT image for the aged PFA sheet (all in accelerated PD aging stage 3)*

To mimic the seemingly anomalous breakdown location, a 5 μm interfacial gap is added to the simulation model and the modified E-field distribution with the gap can be found in Fig. 4-38. The E-field intensity at location A and beyond is about 1.5 times of that in the void. Therefore, due to the possible sharper shapes created by interfacial erosion and driven by the background E-field, an electric tree can occur and develop in the region around or beyond point A, which has some distance from the void wall. The simulation results explain the observations from the micro-CT scan.

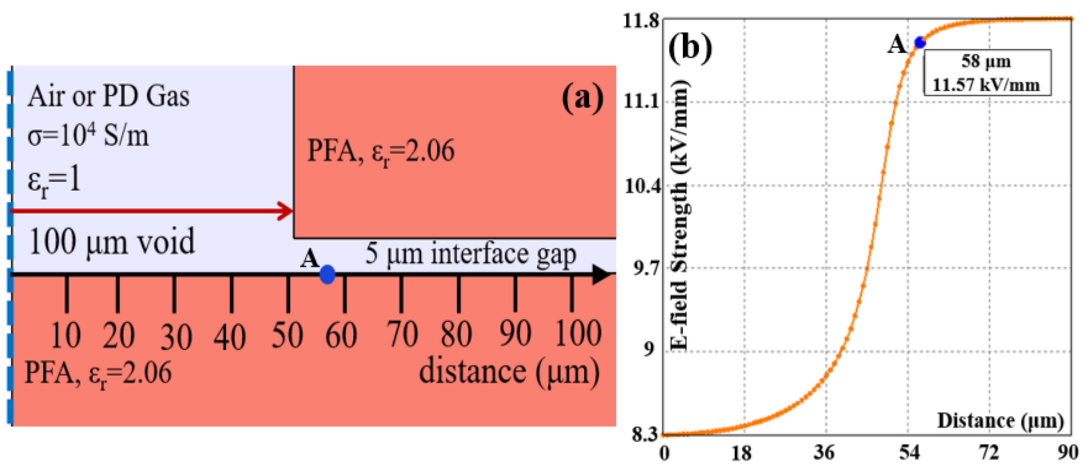

Figure 4-38. *(a) 5 μm gap added in the simulation model to mimic the significant interfacial etching generated by PD (b) E-field distribution along the floor of the interfacial gap in the gas side*

The seven tests are summarized in Table 4-4. For half excitation cycle (either positive or negative), the estimated average PD charge per hour in aging stage 1 and 2 are given in Table 4-4. For those experiments involving stage 3, the total PD charge is only accumulated to the end of stage 2.

Table 4-4. *PD aging stage, time duration and total PD charge of 7 coupons*

Sample Index	Duration (hour)	Results Description	PD Charge (Neg., μC)	PD Charge (Pos., μC)	PD Energy (Pos., mJ)	PD Energy (Pos., mJ)
1	36.65	Aging stage 1	281.69	223.87	2288.6	1810.4
2	41.34	Aging stage 1	315.42	329.05	2408.3	2567.9
3	48.35	Aging stage 2	564.94	608.22	4326.1	4797.2
4	49.48	Aging stage 2	525.33	483.25	4008.7	3606.3
5	61.81	Aging stage 3	660.13	552.77	5039.5	4267.9
6	57.79	Breakdown	725.25	868.54	5843.3	6705.2
7	68.51	Breakdown	793.86	822.41	5927.9	6281.5
For Pos./Neg. cycle, PD charge per hour in aging stage 1 (μC/hour): 7.3						
For Pos./Neg. cycle, PD charge per hour in aging stage 2 (μC/hour): 27.9						

These results are produced in search for an appropriate approach to accelerated aging. These are not processes that would be expected during normal aging in a cable due to the lower void voltage would provide smaller amplitude partial discharges, a reduced discharge frequency, and more diffusion time to relieve the any increase in void pressure.

4.3.6.2. Molded Samples Partial Discharge Aging Results

For a sealed void system, the gas pressure inside the void reflects the dynamic equilibrium between increases with PD activity and pressure relief due to thermal conduction and mass diffusion through the bulk polymer. For Type1 molded sample, the typical test results are shown below.

For Type 1 molded sample, as detailed in Table 4-2, under test, some internal partial discharge pulses can be captured at the excitation of 2.8 kV rms. When the excitation increases to 3 kV rms, consistent partial discharge patterns can be observed. An applied voltage of 3.3 kV rms, which is about 10% higher than the PDIV, was used for a continuous aging test. However, as aging time increases, the detectable PD pulses with their magnitude decrease. After about 8 hours, there are almost no detectable PD pulses under the same testing voltage condition, which can be found in Fig. 4-39.

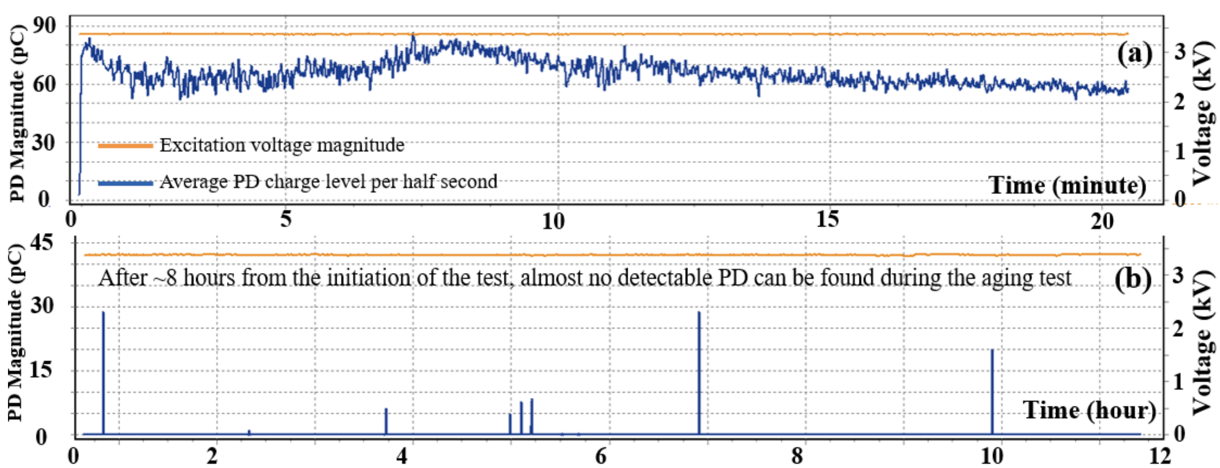

Figure 4-39. *(a) Average PD magnitude behavior decreases with the increase of aging time (b) After 8 hours continuous PD aging, almost no detectable PD pulses under the same test voltage*

Then, the excitation voltage was raised to 4 kV rms, and larger PD events occur after the voltage rises. However, as aging time increases, the partial discharge magnitudes decrease. After about 24 hours, a reduced but consistent PD behavior is measured, which can be found in Fig. 4-40.

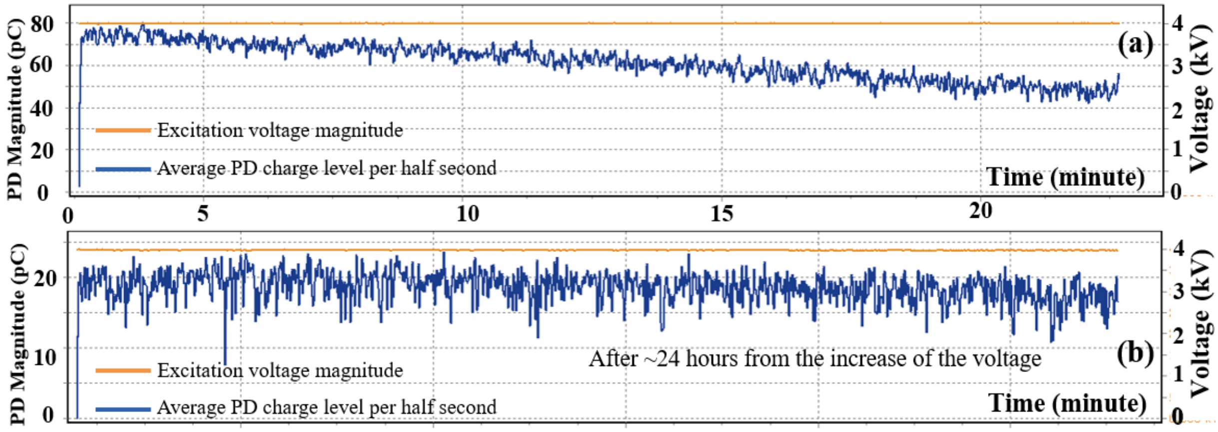

Figure 4-40. *(a) Average PD magnitude behavior decreases with the increase of aging time (b) After 24 hours continuous PD aging, a reduced but consistent PD behavior can be captured*

To confirm this partial discharge behavior, the excitation voltage was raised to 5 kV rms. Similarly, after the voltage rises, larger partial discharges are measured. However, as aging time increases, the detectable PD pulses with their magnitude decrease. Compared to behavior under 4 kV rms, magnitude decrease takes more time, ~36 hours, to reach the new stable status. After about 36 hours, a reduced but consistent PD behavior can be observed, which can be found in Fig. 4-41. The average charge per hour under 5 kV rms is higher than that under 4 kV rms, after both enter the new PD stable status.

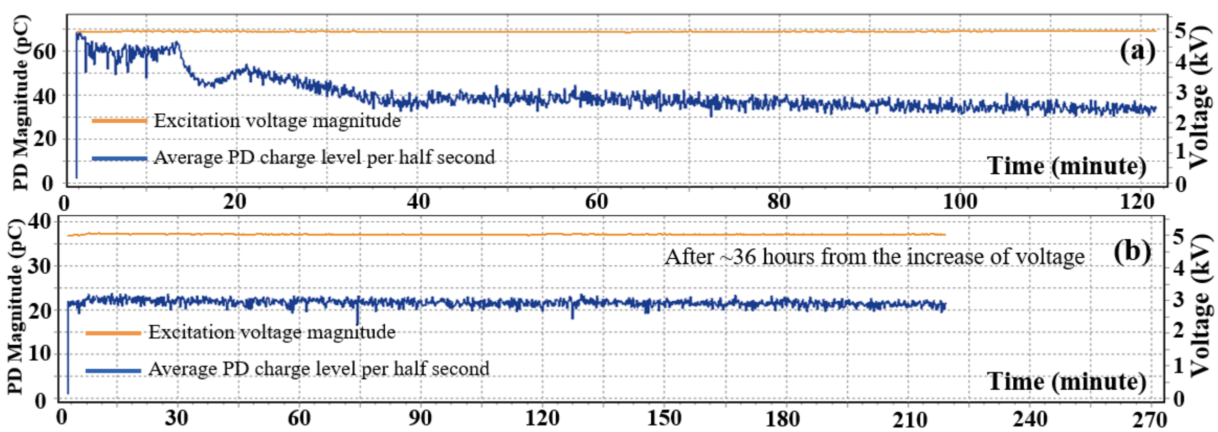

Figure 4-41. *(a) Average PD magnitude behavior decreases with the increase of aging time (b) After 36 hours continuous PD aging, a reduced but consistent PD behavior can be captured*

Finally, the excitation voltage is increased to 6 kV rms. Similarly, after the voltage increase, larger partial discharges are measured. As aging time increases, the magnitude decreases. After about 48 hours, a reduced but consistent behavior is observed, which can be found in Fig. 4-42. The average charge per hour under 6 kV rms is higher than that under 5 kV rms, after both enter the stable status. A pattern in the partial discharge pulse rate is observed under 6 kV rms after the in the steady state. It has a clear rabbit shape which matches the typical characteristic of internal PD.

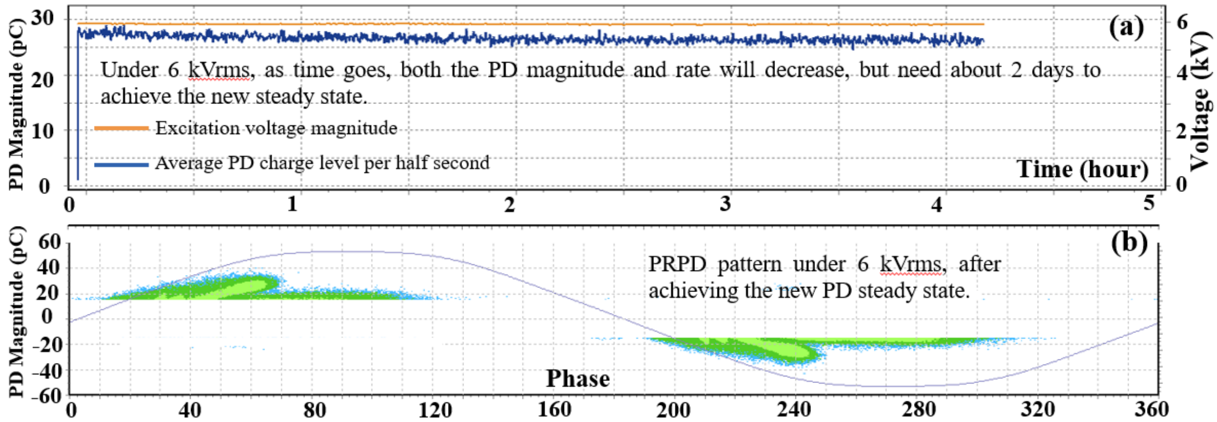

Figure 4-42. *(a) After ~48 hours of continuous PD aging, a reduced but consistent PD behavior can be captured under 6 kV rms (b) A typical PRPD pattern under 6 kV rms after the PD behavior enters the new steady state*

Typical values for all four cases are in Table 4-5. The values shown in Table 4-5 are steady state after waiting sufficient time from the excitation voltage increase. The computation process is shown in Appendix II of this report.

Table 4-5. *Average PD charge and energy per hour for the Type 1 molded sample under different excitation voltage magnitudes after the internal PD behavior reaches the steady state in each level*

Test Condition	State	PD Charge (Neg., μC/hour)	PD Charge (Pos., μC/hour)	PD Energy (Neg., mJ/hour)	PD Energy (Pos., mJ/hour)
3.3 kV rms	All cases under the new PD steady state	0	0	0	0
4 kV rms		0.41	0.28	0.97	0.69
5 kV rms		1.14	0.97	3.87	3.21
6 kV rms		3.31	2.65	12.15	9.49

Finally, the test voltage is held at 6 kV rms, for about 7 days of continuous aging. The metallization layer and oil are removed using alcohol wash. As shown in Fig. 4-43, some interfacial erosion, which is orthogonal to the applied E-field, can be observed like the open interface aged samples. However, as expected the erosion length is quite limited, only about 40 to 50 μm and very shallow. Besides that, a clear round shape erosion, which is along the E-field direction, can be identified. As measured by the microscope, the erosion diameter is about 150 μm with about 12 μm deep.

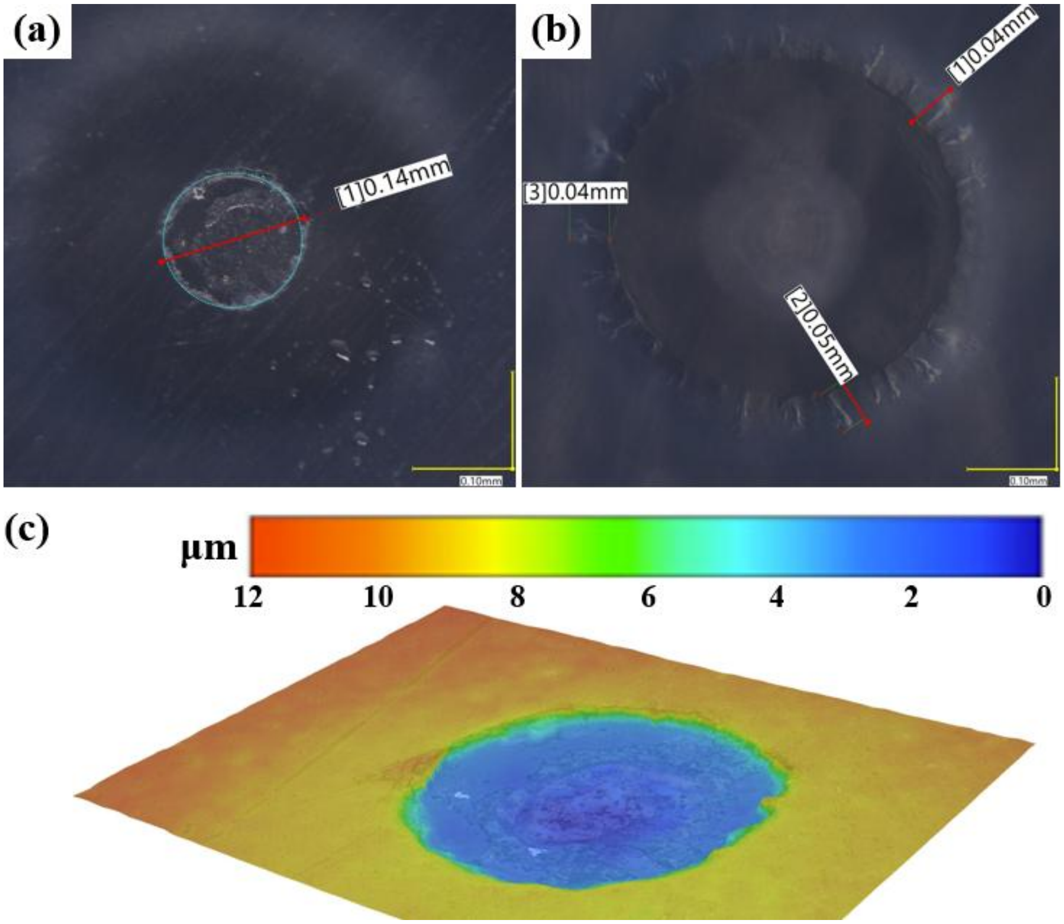

Figure 4-43. *(a) (b) After 1-week continuous PD aging at 6 kV rms, typical erosion patterns observed for the Type 1 molded sample (b) Estimated erosion depth captured by the 3D function of the microscope*

Since two samples from Type 1 molded sample group have been tested under the same conditions for a similar time duration, the total PD charge and energy for the two samples can be found in Table. 4-6. Because they have similar erosion patterns, only one result is shown in Fig. 4-43.

Table 4-6. *PD aging stage, time duration and total PD charge of two coupons in Type 1 molded sample group*

Sample Index	Duration (hour)	PD Charge (Neg., µC)	PD Charge (Pos., µC)	PD Energy (Neg., mJ)	PD Energy (Pos., mJ)
1	135	447	351	1640	1278
2	37	112	128	445	427

For Type 2 molded sample, as detailed in Table 4-3, the partial discharge behavior is very similar to Type 1 molded coupon, thus the figures are not repeated here. However, due to the smaller hole size, ~100 µm diameter, the partial discharge magnitude is quite small. This smaller magnitude is expected for two reasons. First, a smaller ionization volume introduced by a smaller void will lead to smaller partial discharge magnitude. Second, as discussed in the open interface sample section, the partial discharge energy density for smaller void can be much higher than that in a larger void, which means that the gas pressure in small void is at a higher level. On one hand, it could mitigate the PD behavior due to higher gas pressure. On the other hand, a higher gas pressure together with a higher PD energy density can damage the insulation sample more severely, which leads to a shorter time duration to breakdown for small void.

A typical example of partial discharge signal, when Type 2 molded sample is under 10 kV rms electric stress, can be found in Fig. 4-44. Under such conditions, even though the E-field stress in the void is very high (ideally around 55.8 kV/mm), the partial discharge pulse magnitude after the test starts is only up to around 30 pC. As time goes on, the partial discharge magnitude and rate decrease, which is very similar to the phenomena observed in the Type 1 molded sample tests.

About 0.5 to 1 hour after the test starts, the partial discharges evolve to a new steady state condition and many pulses around 10 pC can be observed. This is already very close to the experimental resolution so partial discharge pulses smaller than 8 pC could exist under this test condition. Therefore, the reported estimate of total partial discharge charge and energy shown in this report under this test condition is underestimated.

Due to the small void diameter, experimental sensitivity limits partial discharge signals to be measured for Type 2 molded samples for excitation around ~ 6 kV rms. The only comparison possible with the results from Type 1 sample is the time duration to breakdown under 10 kV rms and 6 kV rms respectively, as shown in Fig. 4-45. It only takes about 12 hours to breakdown for Type 2 molded samples under 10 kV rms PD aging and the time to breakdown will increase to around 27 hours when excitation voltage reduces to 6 kV rms aging. The morphology near the breakdown region (or the hole nearby region) can be found in Fig. 4-46.

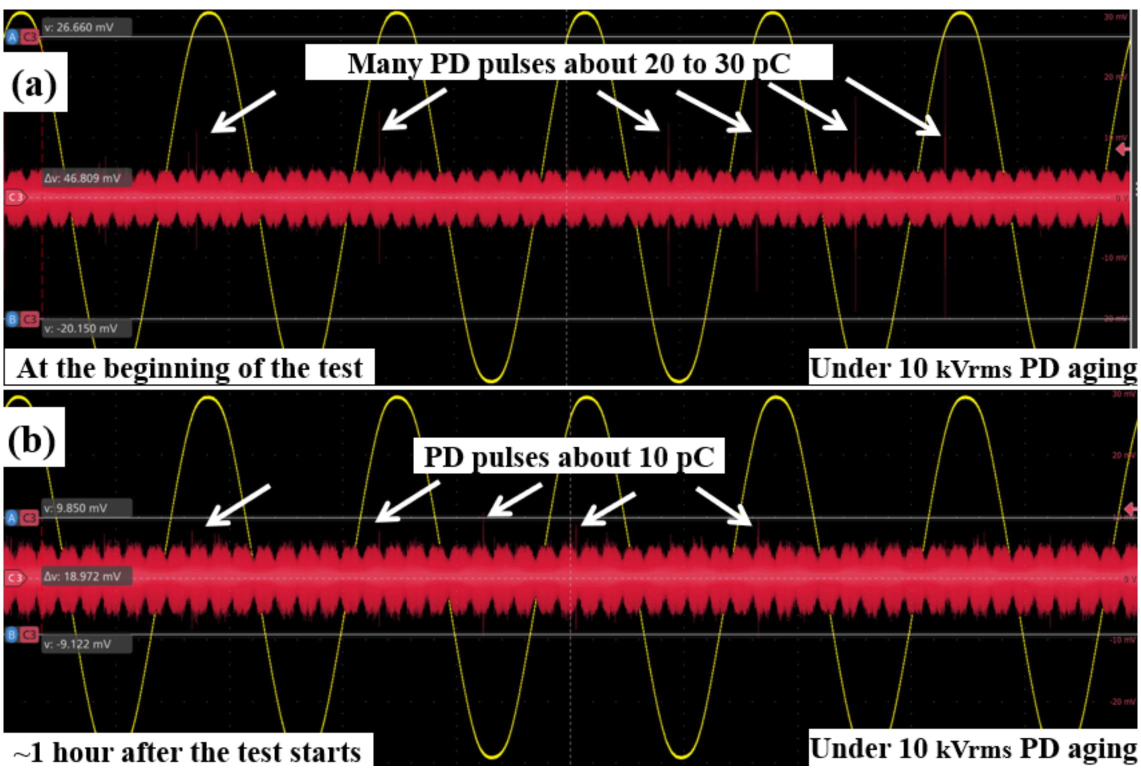

Figure 4-44. *(a) Typical PD pulses captured by the scope for Type 2 molded sample under 10 kV rms excitation after the PD aging test just begins (b) Typical PD pulses captured by the scope for Type 2 molded sample under 10 kV rms excitation after 1 hour from the time when the PD aging test begins*

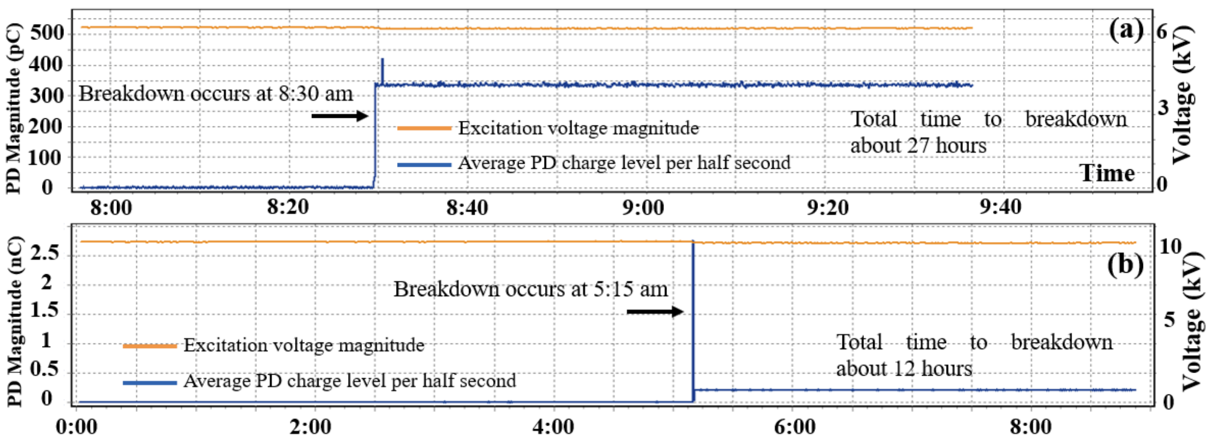

Figure 4-45. *(a) Type 2 molded sample under PD aging test of 6 kV rms excitation and breakdown signal is observed after about 27 hours continuous aging (b) Type 2 molded sample under PD aging test of 10 kV rms excitation and breakdown signal is observed after about 12 hours continuous aging*

Although the breakdown current is limited, the high energy introduced during the breakdown still damages and melts the void nearby region, which provides a hole which is about 2 to 3 times larger than the original void diameter as shown in Fig. 4-46. However, comparing with the open interface sample results, no interfacial erosion orthogonal to the applied E-field can be observed. Moreover, there was no significant increase of partial discharge magnitudes or rates as the aging time increases for the molded samples. These observations indicate that most PD energy contributes to the erosion parallel to the applied E-field direction for the molded samples. The estimate of the total partial discharge charge, energy, and erosion rate etc., for both Type 1 and Type 2 molded samples are given in Table 4-7.

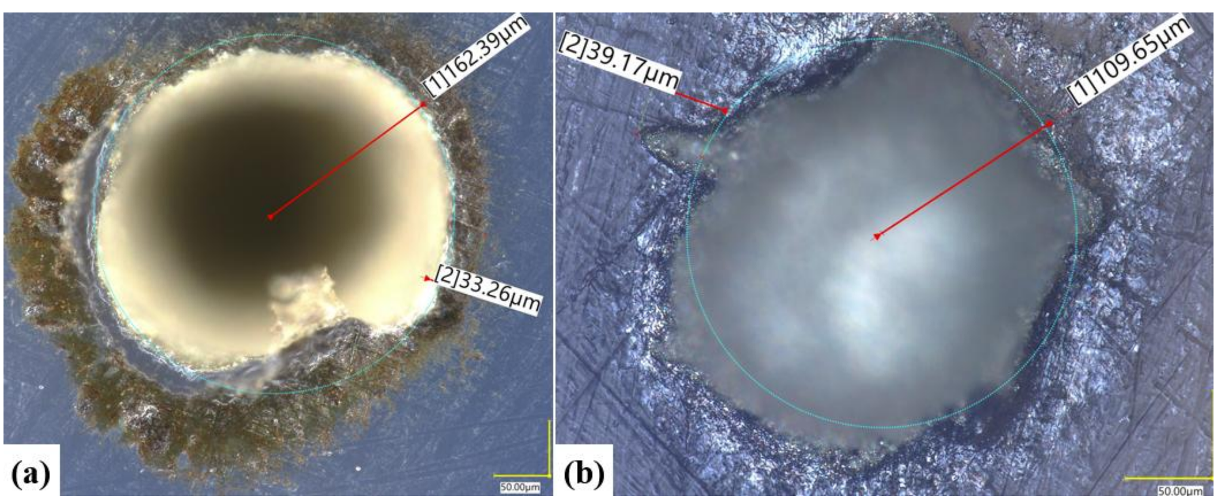

Figure 4-46. *(a) The morphology near the breakdown region (or the hole nearby region) of Type 2 molded sample after breakdown under 10 kV rms (b) The morphology near the breakdown region (or the hole nearby region) of Type 2 molded sample after breakdown under 6 kV rms*

Table 4-7. *PD aging stage, time duration, total PD charge, PD energy, estimated erosion rate etc. comparison between Type 1 and Type 2 molded samples*

Sample Index	Duration (hour)	Condition	PD Charge (Neg., µC)	PD Charge (Pos., µC)	PD Energy (Neg., mJ)	PD Energy (Pos., mJ)	Erosion rate (mJ/µm)
Type 1	135	6 kV rms, not breakdown	447	351	1640	1278	136.7
Type 2	12	10 kV rms, breakdown	28.52	38.88	155.5	210.6	1.8

4.3.7. Comparison with Conventional Large-Diameter Surrogate Voids

Prior research by other investigators focused on much larger diameter void coupons provided the perception that such a three-layer approach can be a valuable surrogate for cable voids. While that can be true in some cases, these earlier observations yielded some major differences from this investigation. To identify the key the differences, a set of aging experiments was conducted for large diameter hole (~2000 µm) samples in N_2 and tested around 21 continuous days. This provides similar conditions that was used in the earlier investigations.

If a nominal 2 mm diameter hole is applied in the middle layer, its typical partial discharge behavior is shown in Fig. 4-47. The results are almost symmetrical between positive and negative excitation cycles, consistent with internal partial discharge. Besides, the partial discharge stays approximately constant, indicating that damage or material change may be happening slowly.

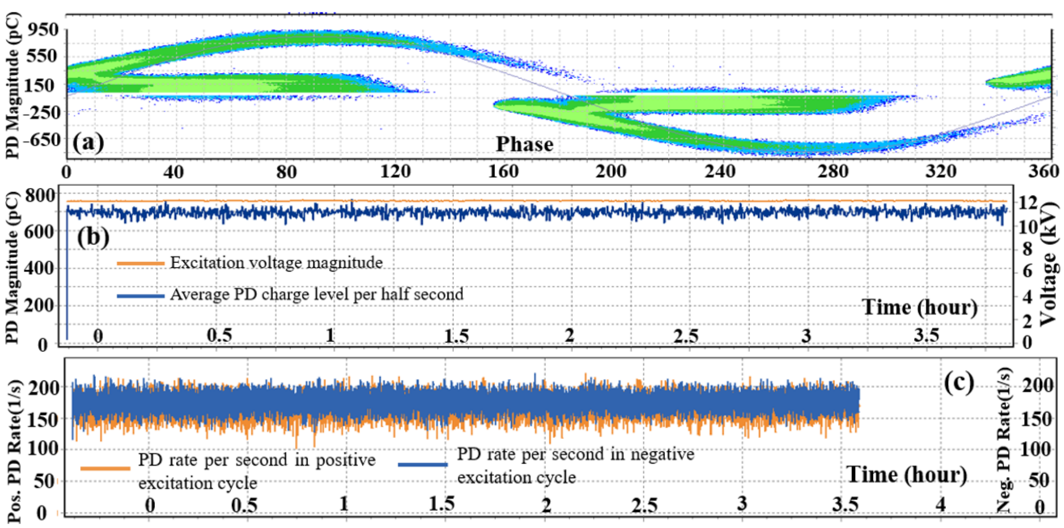

Figure. 4-47. *(a)(b)(c): Typical PRPD pattern, average PD charge level and PD rate results for three-layer coupon in accelerated PD aging test (~2000 µm diameter cylinder void in middle layer)*

The PD charge rate for this test structure ranges from 137 µC/hour to 153 µC/hour. Using the white light interferometry, only some damage along the hole edges can be detected in either the top or bottom layers. In the center of the aged region, no significant material removal can be measured, except some surface roughness changes. This is like the results published by other researchers, but quite different from the aging result with laser drilled small voids.

5. CONCLUSION

These data indicate that, as anticipated, partial discharges provide insight into the change of aging rate with time. This phenomenon, when demonstrated conclusively, can provide an indication of the status of the life of a cable in service. The data are, however, indicative rather than definitive due to the confounding factor of interfacial erosion that is produced when attempting to accelerate the aging process.

This document does not contain any export regulated technical data.

6. References

[1] Sachan S, Zhou C, Bevan G, Alkali B. Prediction of power cable failure rate based on failure history and operational conditions. In9th International Conference on Insulated Power Cables 2015 Jun 25.

[2] A. Kelen, "Studies on Partial Discharges on Solid Dielectrics - a Contribution to the Discharge Resistance Testing of Insulating Materials", Acta Polytechn. Scandin., Electr. Engin. Series No. 16, 1967.

[3] Niemeyer, Lutz. "A generalized approach to partial discharge modeling." IEEE transactions on Dielectrics and Electrical insulation 2.4 (1995): 510-528.

[4] Montanari G C, Cavallini A. Partial discharge diagnostics: from apparatus monitoring to smart grid assessment. IEEE Electrical Insulation Magazine, 2013,29(3): 8-17.

[5] Wenrong S, Junhao L, Peng Y, et al. Digital detection, grouping and classification of partial discharge signals at DC voltage. IEEE Transactions on Dielectrics and Electrical Insulation, 2008, 15(6): 1663-1674.

[6] Morshuis P H F, Smit J J. Partial discharges at DC voltage: their mechanism, detection and analysis. IEEE Transactions on Dielectrics and Electrical Insulation, 2005, 12(2): 328-340.
J. S. Townsend, Electricity in Gases. Clarendon Press, 1915.

[7] Takahashi E, Tsutsumi Y, Okuyama K, et al. Partial discharge characteristics of oil-immersed insulation systems under DC, combined AC-DC and DC-reversed polarity voltage. IEEE Transactions on Power Apparatus and Systems, 1976, 95(1): 411-420.

[8] CIGRE Working Group D1.29 "Partial discharges in transformers" (CIGRE Technical Brochure 676, 2017) Interim Report of WG D1.63: Progress on Partial discharge detection under DC voltage stress, 2020.

[9] Cheng Pan, George Chen, Ju Tang and Kai Wu. Numerical Modeling of Partial Discharges in a Solid Dielectric-bounded Cavity: a Review. IEEE Transactions on Dielectrics and Electrical Insulation, 2019, 26(3): 981-1000.

[10] Nakamura K, Kamijo Y. Fluctuation Mechanism of DC Partial Discharge in Polyethylene and Impulse Noise in Submarine Cable. Japanese Journal of Applied Physics, 1976, 15(5): 865. IEC/IEEE 65700-19-03: "Bushings for DC application" (International Standard, IEC/IEEE 2014).

[11] A. Cavallini, L. Boyer, M.-H. Luton, P. Mirebeau, and G.C. Montanari. "Partial Discharge testing of XLPE cables for HVDC: Challenges and opportunities". In Proc. of Jicable. Versailles, France, June 2015, pp. 1–6.

[12] C. L. da Silva and V. P. Pasko, "Dynamics of streamer-to-leader transition at reduced air densities and its implications for propagation of lightning leaders and gigantic jets", Journal of Geophysical Research: Atmospheres, vol. 118, no. 24, pp. 13, 561–13, 590, 2013.

[13] International Electrotechnical Commission, "High-voltage test techniques- partial discharge measurements", IEC 60270:2000.

[14] L. B. Loeb, Electrical coronas, their basic physical mechanisms. Berkeley: Univ. of California Press, 1965.

[15] G. W. Trichel, "The mechanism of the negative point to plane corona near onset", Phys. Rev., vol. 54, no. 12, pp. 1078–1084, 1938.

[16] Feng X, Xiong Q, Gattozzi AL, Hebner RE. Partial discharge experimental study for medium voltage DC cables. IEEE Transactions on Power Delivery. 2020 Jun 15;36(2):1128-36.

[17] H.-E. Wagner, R. Brandenburg, K. V. Kozlov, A. Sonnenfeld, P. Michel, and J. F. Behnke, “The barrier discharge: Basic properties and applications to surface treatment”, Vacuum, vol. 71, no. 3, pp. 417–436, 2003.

[18] T. N. Tran, “Surface discharge dynamics: Theory, Experiment and Simulation”, Ph.D. Thesis, University of Southampton, Sep. 2010.

[19] Ieda N., “Dielectric breakdown process of polymers”, IEEE Transactions on Electrical Insulation, Vol. 15, pp.206-224, 1980.

[20] Xiangrong Chen, Yang Xu , Xiaolong Cao and S. M. Gubanski, “Electrical Treeing Behavior at High Temperature in XLPE Cable Insulation Samples”, IEEE Transactions on Dielectrics and Electrical Insulation Vol. 22, No. 5, pp.2841-2851, 2015.

[21] Xiangrong Chen, Yang Xu , Xiaolong Cao and S. M. Gubanski, “Electrical Treeing Behavior at High Temperature in XLPE Cable Insulation Samples”, IEEE Transactions on Dielectrics and Electrical Insulation Vol. 22, No. 5, pp.2841-2851, 2015.

[22] Kim M, Hebner RE, Hallock GA. Modeling the growth of streamers during liquid breakdown. IEEE Transactions on Dielectrics and Electrical Insulation. 2008 Apr 3;15(2):547-53.

[23] Van Brunt RJ. Physics and chemistry of partial discharge and corona. Recent advances and future challenges. IEEE Transactions on dielectrics and Electrical Insulation. 1994 Oct;1(5):761-84.

[24] Y. Nyanteh, L. Graber, C. Edrington, S. Srivastava, D. Cartes, Overview of simulation models for partial discharge and electrical treeing to determine feasibility for estimation of remaining life of machine insulation systems, in Electrical Insulation Conference (EIC), 2011, IEEE, 2011, pp. 327–332.

[25] M.H. Ahmad, N. Bashir, H. Ahmad, A.A. Abd Jamil, A.A. Suleiman, An overview of electrical tree growth in solid insulating material with emphasis of influencing factors, mathematical models and tree suppression, TELKOMNIKA Indonesia. Electr. Eng. (2014) 12.

[26] W. Hauschild, W. Mosch, Statistical Techniques for High-Voltage Engineering, IET, 1992.

[27] S. Bahadoorsingh, S. Sambeharry, R. Balliram, C. Sharma, Electrical treeing diagnostics-an approach combining optical measurements and partial discharge statistics, W. Ind. J. Eng. 34 (2012) 98–109.

[28] N. Kottegoda, Fitting Johnson Sb curve by the method of maximum likelihood to annual maximum daily rainfalls, Water Resour. Res. 23 (1987) 728–732.

[29] W. Weibull, A statistical distribution function of wide applicability, J. Appl. Mech-Trans. ASME 18 (1951) 293–297.

[30] L. Niemeyer, L. Pietronero, H.J. Wiesmann, Fractal dimension of dielectric breakdown, Phys. Rev. Lett. 52 (1984) 1033–1036.

[31] Dissado, P. Sweeney, J. Fothergill, The field dependence of electrical tree growth, in: Dielectric Materials, Measurements and Applications, 1992, Sixth International Conference on, IET, 1992, pp. 13–16.

[32] LJ. Champion, S. Dodd, G. Stevens, Analysis and modelling of electrical tree growth in synthetic resins over a wide range of stressing voltage, J. Phys. D: Appl. Phys. 27 (1994) 1020.

[33] L.A. Dissado, J.C. Fothergill, Electrical Degradation and Breakdown in Polymers, IET, 1992.

[34] R. Spatschek, E. Brener, A. Karma, Phase field modeling of crack propagation, Phil. Mag. 91 (2011) 75–95.

[35] Karma, Alain, David A. Kessler, and Herbert Levine. "Phase-field model of mode III dynamic fracture." Physical Review Letters 87.4 (2001): 045501.

[36] Karma, Alain, and Alexander E. Lobkovsky. "Unsteady crack motion and branching in a phase-field model of brittle fracture." Physical review letters 92.24 (2004): 245510.

[37] Karma, Alain. "Phase-field formulation for quantitative modeling of alloy solidification." Physical review letters 87.11 (2001): 115701.

[38] N. Kottegoda, Fitting Johnson Sb curve by the method of maximum likelihood to annual maximum daily rainfalls, Water Resour. Res. 23 (1987) 728–732.

[39] Corson, F., et al. "Thermal fracture as a framework for quasi-static crack propagation." International journal of fracture 158.1 (2009): 1-14.

[40] Govaert, Leon, Brian Brown, and Paul Smith. "Temperature dependence of the Young's modulus of oriented polyethylene." Macromolecules 25.13 (1992): 3480-3483.

[41] Xiangrong Chen, Yang Xu , Xiaolong Cao and S. M. Gubanski, "Electrical Treeing Behavior at High Temperature in XLPE Cable Insulation Samples, IEEE Transactions on Dielectrics and Electrical Insulation Vol. 22, No. 5, pp.2841-2851, 2015.

[42] Karma, Alain, and Wouter-Jan Rappel. "Quantitative phase-field modeling of dendritic growth in two and three dimensions." Physical review E 57.4 (1998): 4323.

[43] Brackbill, Jeremiah U., Douglas B. Kothe, and Charles Zemach. "A continuum method for modeling surface tension." Journal of computational physics 100.2 (1992): 335-354.

[44] B. Yoda and N. Sakabe, "Treeing degradation of high voltage polyethylene insulated cable", Hitachi Review, Vol.51, pp.72-76, 1969.

[45] Y. Yamada, "Treeing phenomena in polyethylene", Sumitomo Electric Review, Vol.101, pp.24-36, 1969.

[46] H.R. Zeller, ‘‘Breakdown and pre-breakdown phenomena in solid dielectrics’’, IEEE Trans. EI., Vol.22, pp.115-122, 1987

[47] H.R. Zeller and W.R. Schneider, "Electro fracture Mechanism of Dielectric Aging", J Appl. Phys., Vol.56, pp. 455-459, 1984.

[48] Tzimas, Antonios. Identification of ac electro-thermal ageing markers from Artemis cable peelings. University of Leicester (United Kingdom), 2008.

[49] Feng, Xianyong, et al. "Partial discharge experimental study for medium voltage DC cables." IEEE Transactions on Power Delivery 36.2 (2020): 1128-1136.

[50] L. E. Kline and J. G. Siambis, "Computer simulation of electrical breakdown in gases: avalanche and streamer formation", Phys. Rev. A., vol. 5, no. 2, Feb. 1972.

[51] Shekhar A, Feng X, Gattozzi A, Hebner R, Wardell D, Strank S, Rodrigo-Mor A, Ramírez-Elizondo L, Bauer P. Impact of DC voltage enhancement on partial discharges in medium voltage cables—An empirical study with defects at semicon-dielectric interface. Energies. 2017 Nov 26;10(12):1968.

[52] Gutfleisch F and Niemeyer L 1995 Measurement and simulation of PARTIAL DISCHARGE in epoxy voids IEEE Trans. Dielectr. Electr. Insul. 2 729–43

[53] Niemeyer, Lutz. "A generalized approach to partial discharge modeling." IEEE transactions on Dielectrics and Electrical insulation 2.4 (1995): 510-528.

[54] Pan, Cheng, et al. "Numerical modeling of partial discharges in a solid dielectric-bounded cavity: A review." IEEE Transactions on Dielectrics and Electrical Insulation 26.3 (2019): 981-1000.

[55] Villa, Andrea, et al. "A PARTIAL DISCHARGEE-based partial discharge simulator." Journal of Computational Physics 345 (2017): 687-705.

[56] Callender, George, et al. "Critical analysis of partial discharge dynamics in air filled spherical voids." Journal of Physics D: Applied Physics 51.12 (2018): 125601

[57] Dordizadeh, Peyman, Kazimierz Adamiak, and GS Peter Castle. "Study of the impact of photoionization on negative and positive needle-plane corona discharge in atmospheric air." Plasma Sources Science and Technology 25.6 (2016): 065009

[58] Tran, T. N., et al. "Numerical modelling of negative discharges in air with experimental validation." Journal of Physics D: Applied Physics 44.1 (2010): 015203.

[59] Babaeva, Natalia Yu, Ananth N. Bhoj, and Mark J. Kushner. "Streamer dynamics in gases containing dust particles." Plasma Sources Science and Technology 15.4 (2006): 591.

[60] Kushner, Mark J. "Modelling of micro discharge devices: plasma and gas dynamics." Journal of Physics D: Applied Physics 38.11 (2005): 1633.

[61] Ségur, Pierre, et al. "The use of an improved Eddington approximation to facilitate the calculation of photoionization in streamer discharges." Plasma Sources Science and Technology 15.4 (2006): 648.

[62] Bourdon A, Pasko VP, Liu NY, Célestin S, Ségur P, Marode E. Efficient models for photoionization produced by non-thermal gas discharges in air based on radiative transfer and the Helmholtz equations. Plasma Sources Science and Technology. 2007 Aug 3;16(3):656.

[63] Kang WS, Park JM, Kim Y, Hong SH. Numerical study on influences of barrier arrangements on dielectric barrier discharge characteristics. IEEE Transactions on Plasma Science. 2003 Aug 18;31(4):504-10.

[64] Dordizadeh, Peyman, Kazimierz Adamiak, and GS Peter Castle. "Study of the impact of photoionization on negative and positive needle-plane corona discharge in atmospheric air." Plasma Sources Science and Technology 25.6 (2016): 065009.

[65] Tran, T. N., et al. "Numerical modelling of negative discharges in air with experimental validation." Journal of Physics D: Applied Physics 44.1 (2010): 015203.

[66] Callender, George, et al. "Critical analysis of partial discharge dynamics in air filled spherical voids." Journal of Physics D: Applied Physics 51.12 (2018): 125601.

[67] Pan C, Meng Y, Wu K, Han Z, Qin K and Cheng Y 2011 Simulation of partial discharge sequences using fluid equations J. Phys. D: Appl. Phys. 44 255201

[68] Morshuis P 1993 Partial discharge mechanisms PhD Thesis Delft University of Technology

[69] Stevens, R. N., and F. Guiu. "Energy balance concepts in the physics of fracture." Proceedings of the Royal Society of London. Series A: Mathematical and Physical Sciences 435.1893 (1991): 169-184.

[70] Morshuis PH, Kreuger FH. Transition from streamer to Townsend mechanisms in dielectric voids. Journal of Physics D: Applied Physics. 1990 Dec 14;23(12):1562.

[71] Niemeyer L. A generalized approach to partial discharge modeling. IEEE transactions on Dielectrics and Electrical insulation. 1995 Aug;2(4):510-28.

[72] Yousfi B, Lefkaier IK. Simulation of partial discharges initiation in voids in medium voltage cables insulators. IEEE Transactions on Dielectrics and Electrical Insulation. 2018 Jun;25(3):892-9.

[73] Seri P, Montanari GC, Hebner R. Partial discharge phase and amplitude distribution and life of insulation systems fed with multilevel inverters. In2019 IEEE Transportation Electrification Conference and Expo (ITEC) 2019 Jun 19 (pp. 1-6). IEEE.

[74] Charge Accumulation in Polymeric High Voltage DC Cable Systems, Ph.D. Dissertation, Delft University of Technology, 2006.

[75] J. Kindersberger and C. Lederle, “Surface charge decay on insulators in air and sulfurhexafluorid - Part II: measurements,” IEEE Trans. Dielectric and Electrical Insulation, vol. 15, no. 4, pp. 949-957, Aug. 2008.

[76] P. H. F. Morshuis and J. J. Smit, “Partial discharges at dc voltage: their mechanism, detection and analysis,” IEEE Trans. Dielectric and Electrical Insulation, vol. 12, no. 2, pp. 328-340, April 2005.

[77] F. H. Kreuger and U. Fromm, “Partial discharges in gaseous voids for dc voltage,” Jpn. J. Appl. Phys., vol. 33, pp. 1079-1084, Feb. 1994.

[78] P. H. F. Morshuis and J. J. Smit, “Partial discharges at dc voltage: their mechanism, detection and analysis,” IEEE Trans. Dielectric and Electrical Insulation, vol. 12, no. 2, pp. 328-340, April 2005.

[79] Hikita M, Yamada K, Nakamura A, Mizutani T, Oohasi A, Ieda M. Measurements of partial discharges by computer and analysis of partial discharge distribution by the Monte Carlo method. IEEE Transactions on Electrical Insulation. 1990 Jun;25(3):453-68.

[80] Morshuis PH, Kreuger FH. Transition from streamer to Townsend mechanisms in dielectric voids. Journal of Physics D: Applied Physics. 1990 Dec 14;23(12):1562.

[81] P. Morshuis, "Assessment of dielectric degradation by ultrawide-band PD detection", *IEEE Trans.* Dielectr. Electr. InsuI., vol. 2, pp. 744-760, 1995.

[82] Brown A, Vickerman JC. A comparison of positive and negative ion static SIMS spectra of polymer surfaces. Surface and interface analysis. 1986 Apr;8(2):75-81.

[83] Niemeyer, Lutz. "A generalized approach to partial discharge modeling." IEEE transactions on Dielectrics and Electrical insulation 2.4 (1995): 510-528.

[84] Illias HA, Tunio MA, Mokhlis H, Chen G, Bakar AH. Experiment and modeling of void discharges within dielectric insulation material under impulse voltage. IEEE Transactions on Dielectrics and Electrical Insulation. 2015 Aug 11;22(4):2252-60.

[85] Khachen W, Laghari JR. Estimating lifetime of PP, PI and PVDF under artificial void conditions using step-stress tests. IEEE transactions on electrical insulation. 1992 Oct;27(5):1022-5.

[86] Zoughi R, Bakhtiari S. Microwave nondestructive detection and evaluation of voids in layered dielectric slabs. Research in Nondestructive Evaluation. 1990 Dec;2(4):195-205.

[87] Illias HA, Tunio MA, Abu Bakar AH, Mokhlis H, Chen G. Partial discharge behaviours within a void-dielectric system under square waveform applied voltage stress. IET Science, Measurement & Technology. 2014 Mar;8(2).

[88] Morshuis PH, Kreuger FH. Transition from streamer to Townsend mechanisms in dielectric voids. Journal of Physics D: Applied Physics. 1990 Dec 14;23(12):1562.

[89] Zhao XF, Yao X, Guo ZF, Wang YY, Li JH, Li YM. Partial discharge characteristics and mechanism in voids at impulse voltages. Measurement Science and Technology. 2011 Feb 1;22(3):035704

[90] Aakre TG, Ildstad E, Hvidsten S. Partial discharge inception voltage of voids enclosed in epoxy/mica versus voltage frequency and temperature. IEEE transactions on dielectrics and electrical insulation. 2020 Feb 6;27(1).

[91] Chang DD, Sudarshan TS, Thompson JE. Analysis of electric stress distribution in cavities embedded within dielectric structures. IEEE transactions on electrical insulation. 1986 Apr(2):213-9.

[92] Illias HA, Tunio MA, Bakar AH, Mokhlis H, Chen G. Partial discharge phenomena within an artificial void in cable insulation geometry: experimental validation and simulation. IEEE Transactions on Dielectrics and Electrical Insulation. 2016 Mar 7;23(1):451-9.

[93] Wu K, Suzuoki Y, Dissado LA. The contribution of discharge area variation to partial discharge patterns in disc-voids. Journal of Physics D: Applied Physics. 2004 Jun 16;37(13):1815.

[94] Morshuis PH. Partial discharge mechanisms in voids related to dielectric degradation. IEE Proceedings-Science, Measurement and Technology. 1995 Jan 1;142(1):62-8.

[95] Mazzanti G. Life and reliability models for high voltage DC extruded cables. IEEE Electrical Insulation Magazine. 2017 Aug 22;33(4):42-52.

[96] Montanari GC, Seri P, Bononi SF, Albertini M. Partial discharge behavior and accelerated aging upon repetitive DC cable energization and voltage supply polarity inversion. IEEE Transactions on Power Delivery. 2020 Apr 3;36(2):578-86.

[97] Seri P, Cirioni L, Naderiallaf H, Montanari GC, Hebner R, Gattozzi A, Feng X. Partial Discharge Inception Voltage in DC insulation systems: a comparison with AC voltage supply. In2019 IEEE Electrical Insulation Conference (EIC) 2019 Jun 16 (pp. 176-179). IEEE.

[98] Feng X, Xiong Q, Gattozzi A, Montanari GC, Seri P, Hebner R. Cable commissioning and diagnostic tests: The effect of voltage supply frequency on partial discharge behavior. In2018 12th International Conference on the Properties and Applications of Dielectric Materials (ICPADM) 2018 May 20 (pp. 373-376). IEEE.

[99] Murphy BT, Hebner RE, Kelley EF. Simulating mode transitions during breakdown in liquids. IEEE Transactions on Dielectrics and Electrical Insulation. 2011 Jun 30;18(3):682-91.

[100] ASTM D2413-16: Standard Practice for Preparation of Insulating Paper and Board Impregnated with a Liquid Dielectric

[101] R. F. Harrington, et.al., “Computation of Laplacian Potentials by an equivalent source method,” Proc. IEE, vol 166, no. 10, Oct. 1969, pp. 1715-1720.

[102] J. A. Stratton, Electromagnetic Theory, New York, McGraw Hill Book Co., 1941, pp. 163-167.

[103] Y. Bulent Yildir, K. M. Prasad, and D. Zheng, “Computer aided design in electromagnetic systems: Boundary element method and applications,” Control and Dynamic Systems, vol. 59. New York: Academic, 1993, pp. 167–223.

[104] Yu.G. Smirnov and A.A. Tsupak, “Galerkin method for solving of singular integral equation of diffraction problem”, International Conference on Mathematical Methods in ElectromagneticTheory, 2002, vol 2.

[105] K.R. Davey and D. Zheng, “Error tracking in boundary element formulations,” IEEE Transactions on Magnetics, Vol. 32, No. 1, pp. 259-264, January 1996.

APPENDIX I

Boundary Element Analysis Method

The objective of the boundary element formulation used by this team is encapsulated in Fig. A-1. Each dielectric object is replaced with a layer of surface charge on the interfacial skin. The fictitious layer of surface charge σ_1 on the interfacial layer of the body will serve to represent the body's induced field signature interior and exterior to the body. Since this method does not involve discretizing the surrounding volume, the accuracy of the method can be increased simply by increasing the number of unknowns on the interface [101]. The best analysis techniques involve assigning a high element weighting to the interface regions where the accuracy is most desired. In this work the regions involving corners are weighted 40 times heavier than those near open regions.

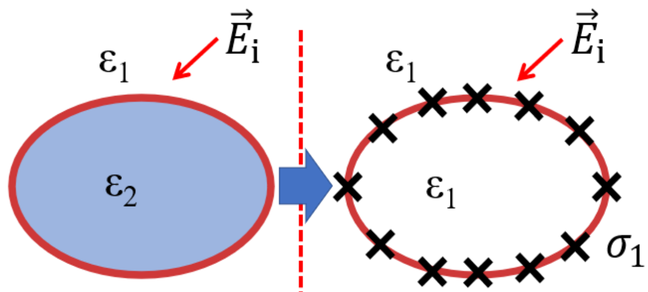

Figure A-1. *Objective of the boundary element method (BEM) used here is to replace the interface between two dielectric materials with a single surface layer charge* σ_1

The layer of surface charge resides on the interface between the two dielectric materials. The surface charges are chosen to guarantee that the jump in tangential E-field is continuous and the normal jump in the displacement field equals the enclosed surface charge, which can be found in equations (II-A-1) and (II-A-2) respectively. At this stage, we assume there is no free volume charge, σf, only free surface charge, σf.

$$\hat{n} \times \|\vec{E}\| = 0 \quad \text{(II-A-1)}$$

$$\hat{n} \cdot \|\vec{D}\| = \sigma_f \quad \text{(II-A-2)}$$

Where σ_f is the surface charge. $\vec{E}$ is the E-field vector and $\vec{D}$ is the displacement field vector.

The E-field is represented as the gradient of a scalar field Φ. Within the interior or exterior region, it follows that:

$$\nabla \cdot \varepsilon\vec{E} = \rho_f \quad \text{(II-A-3)}$$

Since the dielectric constant ε is piecewise continuous, it follows that:

$$\nabla^2\Phi = \frac{\rho_f}{\varepsilon} = 0` \quad \text{(II-A-4)}$$

This equation is commonly represented in terms of the finite element or finite difference forms, but it can also be represented by an integral formulation via using Green's functions [102]. Green's theorem allows this to be written as:

$$\iiint_V \{\Phi \nabla^2 G(r,r') - G(r,r')\nabla^2 \Phi\} dV = \iint_S \left\{\Phi \frac{\partial G(r,r\prime)}{\partial n} - G(r,r')\frac{\partial \Phi}{\partial n}\right\} dS \qquad \text{(II-A-5)}$$

The free space Green's function in two dimensions is shown in (II-A-6),

$$G(r,r')\frac{1}{2\pi|r-r'|}, \text{ Satisfying } -\nabla^2 G(r,r') = 2\pi\delta(r-r') \qquad \text{(II-A-6)}$$

Whereδ is the Dirac delta function defined for the surface integral.

$$\iint_S \left\{\Phi \frac{\partial G(r,r\prime)}{\partial n} - G(r,r')\frac{\partial \Phi}{\partial n}\right\} dS' = \begin{cases} -2\pi\Phi(r) & r \in S \\ 0 & r \in V \end{cases} \qquad \text{(II-A-7)}$$

The free surface charge σ_f at an interface can be written in terms of the electric field potential:

$$\frac{\sigma}{\varepsilon} = \frac{\partial \Phi}{\partial n} \qquad \text{(II-A-8)}$$

The simple layer formulation of Laplace's equation follows:

$$\iint_S G(r,r')\sigma(r')dS' = \varepsilon\Phi(r) \qquad \text{(II-A-9)}$$

Application of the Neumann condition at the boundary for the surface charge in (II-A-2), a final equation for the surface charge can be achieved. By using $\Phi'(r)$ and $G'(r,r')$ to represent the normal derivatives of potential and Green's function with respect to the unprimed variable, the final condition for the surface charge results:

$$(\varepsilon_1 - \varepsilon_2) \cdot \iint_S G'(r,r')\sigma(r')dS' + (\varepsilon_1 + \varepsilon_2)\sigma(r) = 0 \qquad \text{(II-A-10)}$$

In the presence of an incident electric field, (II-A-10) becomes:

$$(\varepsilon_1 - \varepsilon_2) \cdot \iint_S G'^{(r,r\prime)}\sigma(r')dS' + (\varepsilon_1 + \varepsilon_2)\sigma(r) = (\varepsilon_1 - \varepsilon_2)\hat{n} \cdot \vec{E}_{inc} \qquad \text{(II-A-11)}$$

Once this charge is found, the E-field at any point is the impressed E-field added to the Biot-Savart contribution from the charges of the dielectric interface. This field pattern is best computed by the integration of (II-A-9). A good seminal work outlining this type of integral analysis can be found in reference [103]. The solution of (II-A-11) is found by assuming a charge distribution along the interface. It can be piecewise constant, linear, or quadratic. In this work, Galerkin methods are used to solve these unknowns [104][105].

APPENDIX II

Partial Discharg Total Charge and Energy Estimation Method

To get an accurate PD quantitative measurement, both PD checker and scope are applied as shown in Fig. A-2. To enable both measurement methods simultaneously, two HFCT are applied. One HFCT from Doble can allow the PD checker to achieve its best performance, since the same vendor makes them. Another HFCT from Techimp is applied to the scope, which can reach a gain of 1 pC/mV after PD calibration. Please note that, due to the difference of HFCTs, the gain will be different for the two methods, but both can achieve at least 10 pC sensitivity.

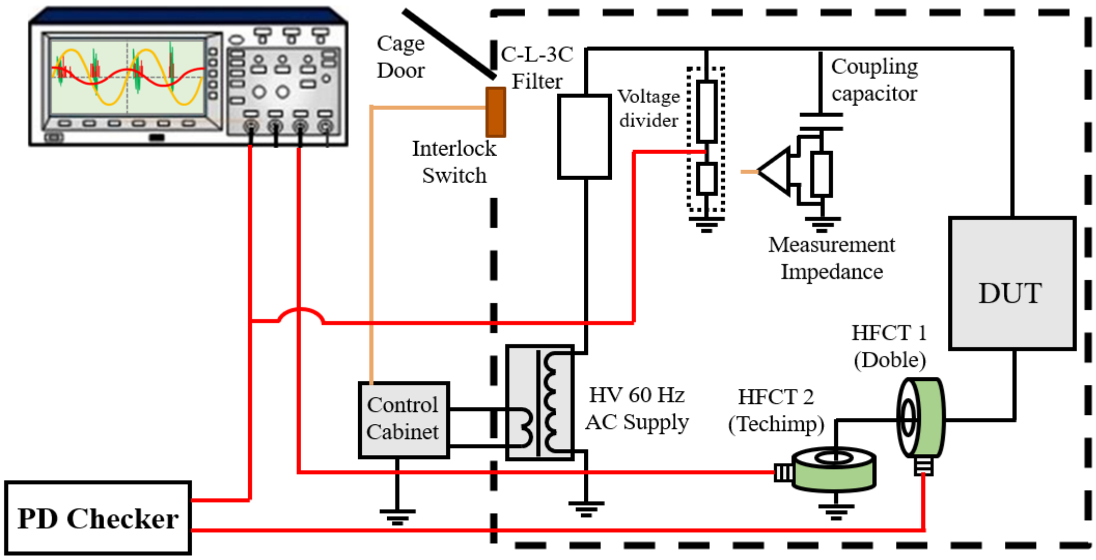

Figure A-2. *Schematic drawing of the PD measurement setup when both PD checker and scope are applied*

PD checker is designed to record PD behavior for a longer period, like a day. Thus, to save hardware cost, it has limited sampling rate, which means a lot of high frequency features of PD signals will be ignored. Meanwhile, it will average the PD characteristics and record one data point per half second, instead of recording each individual PD event. Although it will lose some accuracy due to the limited sampling rate and averaging function, it still can provide good numerical feelings about how PD behavior changes in a day or a week. By comparison, scope is more flexible, and it can provide more details about the PD signal. By selecting a sampling rate of 250 MS/s (1 million sample points per second), each single PD event can be captured with a lot of high frequency features. Thus, by using the data from scope, more accurate numerical information like PD charges and energy for a short period of time can be obtained. However, since due to the high sampling rate and long record length, it is not possible to use the scope continuously to monitor the PD data for several hours or a day.

To enjoy the benefits from both the PD checker and the scope methods, we will majorly use the data from the PD checker to estimate information such as PD charge, energy, etc., for a long time, for example, a day. Besides, at least in every stable PD stage for all the tests, we will pick up several time windows and use scope to record about 100 PD events simultaneously. Thus, we can also get information such as PD magnitude, charge, energy, rates, etc. from the data captured by the scope. In most cases, the information from both methods should match. In some cases, if the information is similar but has some mismatches, we will use the information from the scope and adjust the values from the PD checker a little bit, to provide our best estimation. In some rare cases, part of data from the PD checker may be contaminated due to an automatic gain modification of that equipment, then the data from the scope will be majorly applied to provide the best estimation of PD behaviors for that period.

For total PD charge estimation, we can use the so-called HNQ plot in the PD checker to perform the estimation. A typical HNQ plot for a normal PD recording cycle is shown in Fig. A-3. There are 120 intervals for both the positive and negative PD, which cover from 0 pC to +/- 240 pC. The vertical axis shows the rate of PD events within a certain PD magnitude in this recording cycle. The following equations can be applied to estimate the total PD charges for this recording cycle:

$$Q_{pos} = \int_0^T \sum_{k=1}^{k=120} PDrate_{pos}(k) * PDcharge_{pos}(k)dt \qquad \text{(A-II-12)}$$

$$Q_{neg} = \int_0^T \sum_{k=1}^{k=120} PDrate_{neg}(k) * PDcharge_{neg}(k)dt \qquad \text{(A-II-13)}$$

Where $PDrate_{pos}(k)$ is the PD rate at kth positive interval. $PDcharge_{pos}(k)$ is the PD magnitude at kth positive interval. T is the time duration of this recording cycle. The definition of equation for negative charge calculation is like the positive one.

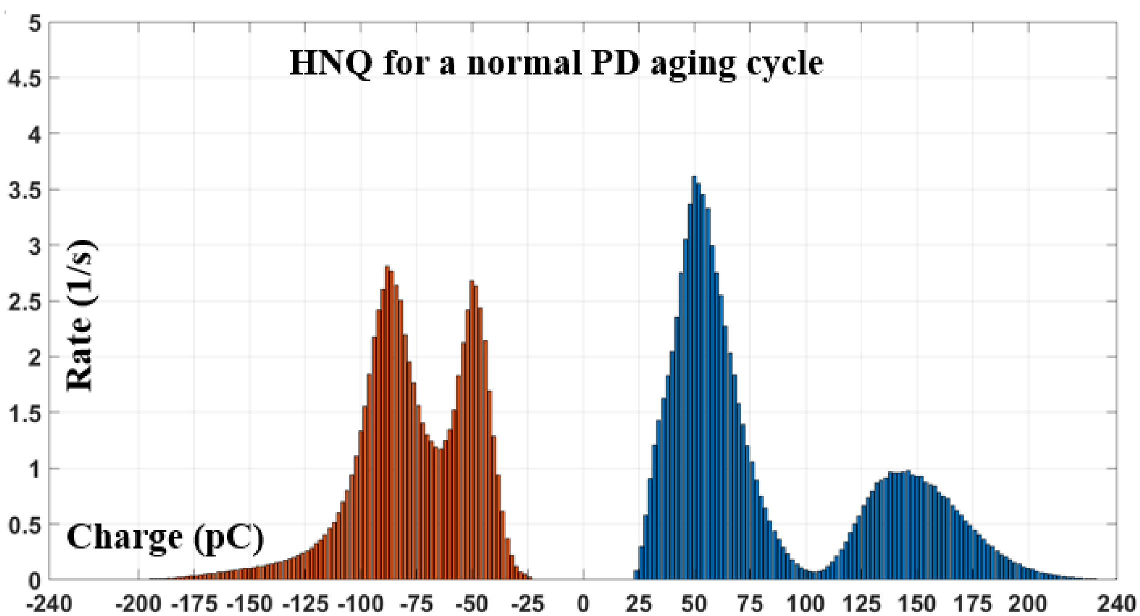

Figure A-3. *Typical HNQ plot for a normal PD recording cycle*

Besides the HNQ plot, the PD checker also provides some time domain data which can be used for numeric estimation. This method is usually applied when HNQ plot is contaminated majorly due to breakdown events. Breakdown event will lead to a lower gain of the PD checker for protection reasons and thus introduce a lot of noise to the HNQ plot after the occurrence of breakdown.

One example is given below. The typical positive PD rate and PD charge time domain waveforms are shown in Fig. A-4 and A-5 individually. The equation which can be applied to estimate the total positive PD charges in this period is below.

$$Q_{pos} = \sum_{k=0}^{k=T} PDrate_{pos}(k) * Q(k) \qquad \text{(A-II-14)}$$

Where $PDrate_{pos}(k)$ is the positive PD rate for the kth time interval. $Q(k)$ is the average PD charge for the kth time interval. T is the time duration. The duration for each time interval is 0.5 second.

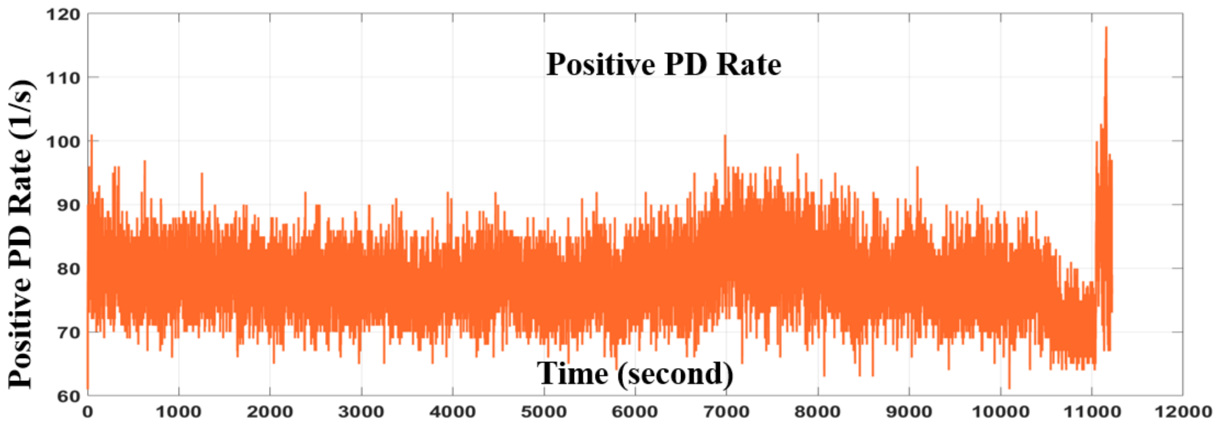

Figure A-4. *Typical positive PD rate time domain waveform*

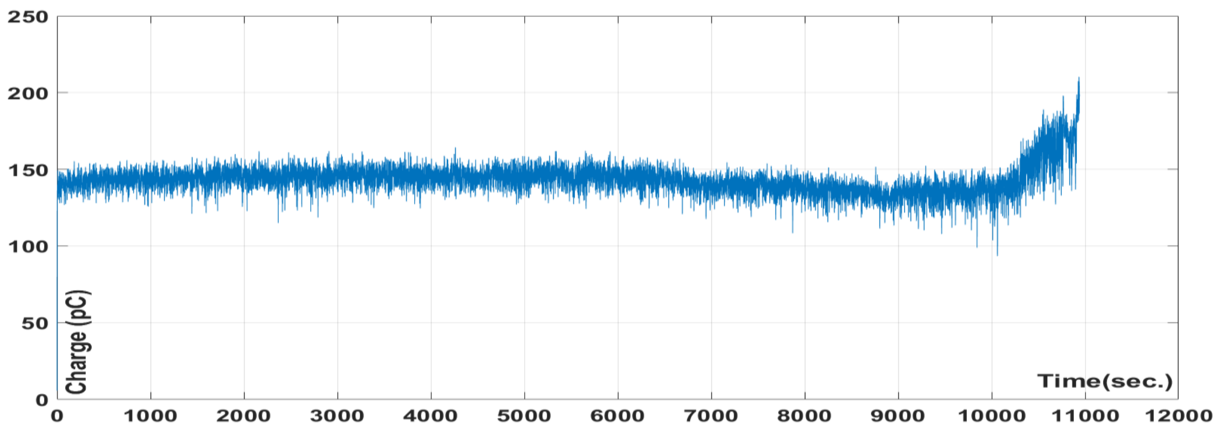

Figure A-5. *Typical positive PD charge time domain waveform*

The PD checker also provides the estimation of PD energy. Based on the PRPD recorded, PD energy can be calculated by the multiplication of PD charge and firing voltage. The definition of PD firing voltage is the magnitude of excitation voltage at the same time point when the PD event is recorded. An example of PRPD pattern with a PD energy plot accordingly can be found in Fig. A-6. In Fig. A-6 (b), PD energy is in log scale to make the PD energy pattern clear.

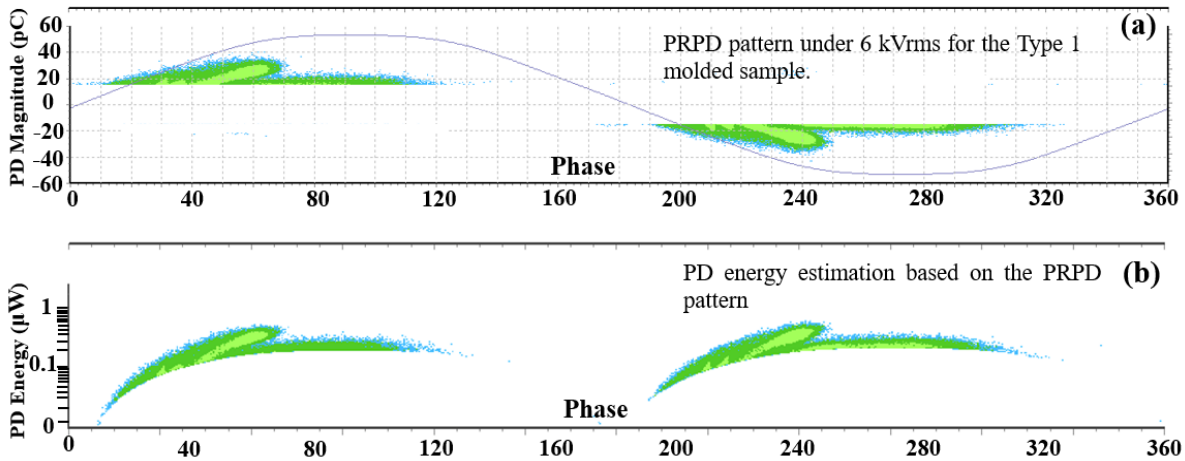

Figure A-6. *(a) A typical PRPD pattern for Type 1 molded sample under PD aging at 6 kV rms for a time (b) PD energy estimation based on the same information from the PRPD pattern*

Similarly, the partial discharge energy for a certain time can be estimated by using the information captured by the scope if the total partial discharge charge information is provided by the PD checker. As an example, shown in Fig. A-7, both the PD events magnitude and their firing voltage can be obtained after analyzing the data from the scope. Thus, the total PD energy for this snapshot and the average PD energy per pC can be calculated. Then, if around thirty-five of such snapshots are processed in a similar way, which means about 100 excitation voltage cycles, the average PD energy per pC for this time window can be estimated. In each steady PD status, about 3 to 5 of such time windows will be selected and the average PD energy per pC value will be calculated by using the scope data. Therefore, if the total PD charge is known from the PD checker, total PD energy for this period can be estimated by using the total PD charge multiplied by the average PD energy per pC. Also, from the scope, the information about total PD charge per one hundred excitation cycles can be obtained, which can provide a way to estimate the total PD charge for a certain period. As a summary, this method not only provides a way to check the value from the PD checker, but also may give an access to a more flexible and accurate PD behavior estimation especially under some conditions when PD signals are very close to the background noise.

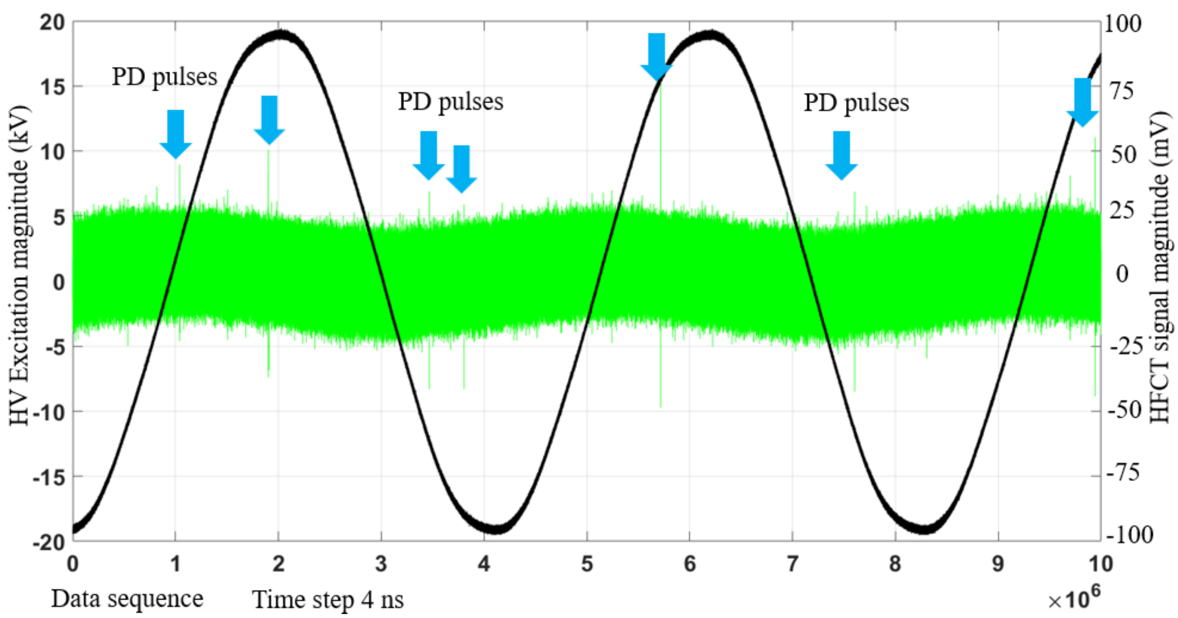

Figure A-7. *An example of scope captured data. Both PD magnitude and firing voltage can be captured simultaneously with two scope channels*